RESEARCH ARTICLE

Advances in Modeling of Noisy Quantum Computers: Spin Qubits in Semiconductor Quantum Dots

DAVIDE COSTA[1],*, MARIO SIMONI[2],*, (Member, IEEE), GIANLUCA PICCININI[2], AND MARIAGRAZIA GRAZIANO[3]

[1]QuTech and Kavli Institute of Nanoscience, Delft University of Technology, 2628 CJ Delft, The Netherlands
[2]Department of Electronics and Telecommunications, Politecnico di Torino, 10129 Torino, Italy
[3]Department of Applied Science and Technology, Politecnico di Torino, 10129 Torino, Italy

Corresponding authors: Mario Simoni (mario.simoni@polito.it) and Davide Costa (d.costa@tudelft.nl)

*Davide Costa and Mario Simoni contributed equally to this work.

ABSTRACT The new quantum era is expected to have an unprecedented social impact, enabling the research of tomorrow in several pivotal fields. These perspectives require a physical system able to encode, process and store for a sufficiently long amount of time the quantum information. However, the optimal engineering of currently available quantum computers, which are small and flawed by several non-ideal phenomena, requires an efficacious methodology for exploring the design space. Hence, there is an unmet need for the development of reliable hardware-aware simulation infrastructures able to efficiently emulate the behaviour of quantum hardware that commits to looking for innovative systematic ways, with a bottom-up approach starting from the physical level, moving to the device level and up to the system level. This article discusses the development of a classical simulation infrastructure for semiconductor quantum-dot quantum computation based on compact models, where each device is described in terms of the main physical parameters affecting its performance in a sufficiently easy way from a computational point of view for providing accurate results without involving sophisticated physical simulators, thus reducing the requirements on CPU and memory. The effectiveness of the involved approximations is tested on a benchmark of quantum circuits — in the expected operating ranges of quantum hardware — by comparing the corresponding outcomes with those obtained via numeric integration of the Schrödinger equation. The achieved results give evidence that this work is a step forward towards the definition of a classical simulator of quantum computers.
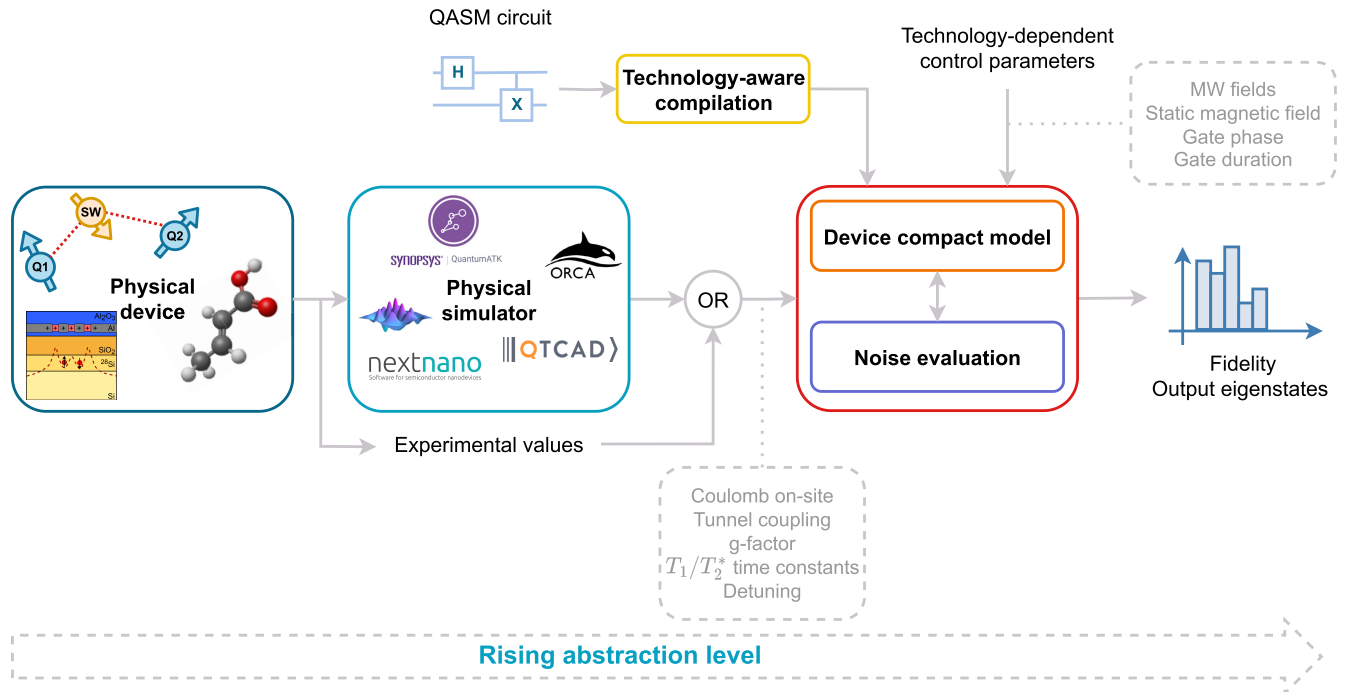
I. INTRODUCTION

Although classical electronics and computer science, based on classical physics, have met the requirements of an ever-inflating number of pervasive applications for several decades thanks to astonishing technological development, some hard problems still remain beyond the reach of classical computers. Quantum computing is expected to be a viable answer to overcome the shortcomings of classical computing in several scenarios. Among these, optimisation [2], image

The associate editor coordinating the review of this manuscript and approving it for publication was Wei Huang.

processing [3], machine learning [4] and chemical simulations [5] can be mentioned. This application-driven exigency urges towards the design of reliable quantum hardware able to encode, process and store for a sufficiently long amount of time the quantum information. Several technologies have been proposed for building a quantum computer based on superconducting devices [6], trapped ions [7], quantum dots [8], molecules [9] and nuclei in diamagnetic molecules (NMR) [10]. Moreover, some devices fabricated by either private companies — e.g., superconducting qubits by IBM [11] and trapped ions by Quantinuum [12] — or Academia — e.g., silicon qubits by QuTech [13] at TU Delft — are already

(a) SiGe-^{28}Si-SiGe heterostructure.

(b) Si-^{28}Si-SiO$_2$ heterostructure.

FIGURE 1. Pictorial representation of the target semiconductor heterostructure devices. In blue are the Y gates, in red the plunger gates, in pale light blue the barrier gates and in yellow the Al$_2$O$_3$ oxide.

accessible *via* cloud. Nevertheless, all currently available devices belong to the so-called Noisy Intermediate Scale Quantum (NISQ) computers era, meaning that they are small and affected by several non-ideal phenomena [14]. Accordingly, the optimal exploration of the design space demands classical trustworthy simulators that must, on the one hand, be able to take into account the main non-ideal phenomena affecting real hardware devices and, on the other, be CPU-and-memory friendly. However, presently accessible classical simulators of quantum computers mainly belong to two well-established families: physically accurate but CPU-intensive simulators based on the direct solution of Schrödinger and Lindblad equations [15], [16], [17] and fast high-level ideal simulators [18] developed for handling many qubit systems. Therefore, there is still an unsatisfied need for an *intermediate-level* simulation infrastructure able to emulate the actual behaviour of real-world quantum hardware and determine, for every technology, the performance dependence on both physical and control degrees of freedom, thus enabling their optimisation according to some fiducial parameters. A possible response to this requirement is the development of a *compact-model* based simulation toolchain, where each device is described in terms of the main physical parameters affecting its performance in a way sufficiently light from a computational point of view for providing accurate results without involving sophisticated physical simulators. This methodology has already been discussed in [19] and [20], with a specific focus on NMR technology, which, on the one hand, represents an iconic example of a system affected by several non-ideal phenomena — such as relaxation, decoherence, off-resonance and residual unwanted coupling – and, on the other, can be regarded as

the archetype of spin-based quantum technologies. At the time of [20], the other technology supported by the proposed simulation infrastructure was represented by molecular nanomagnets.

In this work, a new technology, namely semiconductor quantum dots, is discussed. It shall be noted that semiconductor quantum computation has been a rapidly growing field in the past years thanks to a global investigation on realising fault-tolerant implementations. Experiments on physical devices are indeed yielding noteworthy results in terms of charge control, gate fidelities and coherence times, in both 1D [21], [22] and 2D arrays [23], [24]. In [25], the authors review recent advances in this field, at the fabrication and experimental levels, in both Academia and industry. Quantum dots are one of the most explored possibilities for semiconductor quantum implementation, thanks to their flexibility and technological readiness for such applications. Yet, this is not the only option available for semiconductors: different technologies, namely dopants [26], [27], [28] and optically addressable quantum defects [29], are accessible. Relevant benefits are the small qubit footprint (tens of nanometres) and the fast gate-controlled manipulation and read-out procedure [30], but the most notable advantage is the compatibility with the established CMOS integration techniques [25], [31]. This makes quantum dots a strong candidate for large-scale quantum computing integration and paves the way to the integration of quantum and classical electronics [32], [33]. Moreover, semiconductor quantum devices can be controlled through electric (metal gates) and magnetic (integrated micromagnets) fields, a crucial feature when envisioning possible control schemes of a dense array of several qubits together [34]. Physical semiconductor qubits

FIGURE 2. Proposed quantum simulation toolchain. Currently supported technologies are NMR, quantum dots (presented in this article) and molecular nanomagnets (the latter technology is discussed in [1]). The input physical parameters can be retrieved from experiments or physical simulations exploiting currently available software tools. They are provided, together with technology-dependent control parameters, to the compact-model-based simulation infrastructure. The QASM description of the quantum circuit is compiled by a technology-aware in-house compilation toolchain. The infrastructure outputs the fidelity and the probability distribution of the eigenstates. The input physical and control parameters for the specific case of semiconductor quantum dots — discussed in this article — are reported in the dashed grey rectangles.

have also shown long coherence times, and therefore are promising candidates for building fault-tolerant quantum processors [22], [23], [35], [36]. As far as the encoding of the quantum information is concerned, electrons confined in quantum dots offer different possibilities: **Loss-DiVincenzo qubit** [37] — when the quantum information is encoded on the two Zeeman hyperfine spin levels of the dot ground state such that $|0\rangle = |\downarrow\rangle$ and $|1\rangle = |\uparrow\rangle$ —, the **charge qubit** [38] — when the qubit on the presence of a single electron in a dot or in another — and the **Singlet-Triplet (ST) qubit** [39] — when the qubit is encoded on the singlet-triplet many-body eigenstates of a two-electron-in-two-dot system. This work takes into account Loss-DiVincenzo qubits encoded in quantum dots built into intrinsic silicon, focusing on the two most common heterostructures: SiMOS [40] and SiGe/Si/SiGe heterostructures [41] (cf. Figure 1).

This article is intended to fulfil two objectives:

- First, leveraging the methodology proposed in [20] for spin-based technology, it presents the detailed derivation of a novel compact model for two-qubit semiconductor quantum dot systems, which is then inserted within the MATLAB-based simulation infrastructure of quantum computing technologies under development. Since several different methodologies to initialise the systems and perform the read-out are routinely exploited [42], [43], at the time of writing, the proposed compact model assumes ideal initial states and simple

projective measurements to decouple the simulation from the specific experimental details and facilitate the integration in the multi-technology infrastructure. The approximations employed in the compact model — most of them involving time dependencies simplifications — are then thoroughly verified using the Quantum Toolbox in Python (QuTiP) [15], a Python-based environment able to solve the Lindblad master equation. The error between QuTiP exact simulation and the MATLAB model is plotted with respect to some relevant system input parameters, in order to prove the validity of the model approximations. The model is finally validated in terms of state probability distribution and gate fidelity by extensively verifying its results when simulating different quantum algorithms.

- Second, it envisions the development of a comprehensive classical simulation toolchain that, starting from currently available *low-level* simulators — such as NextNano [17], QTCAD [16], ORCA [44], [45] and QuantumATK [46] — or experimental values and an arbitrary quantum circuit described in OpenQASM 2.0 [47], can determine the expected outcomes in terms of the eigenstate probability distribution, the fidelity and the execution time.

The remaining of this work is organised as follows: Section II discusses the classical simulation toolchain for quantum computers, Section III describes the detailed

derivation of the compact model, Section IV presents some FEM simulations aiming to extract the compact model's input parameters, Section V collects the results obtained with the proposed models and eventually Section VI draws the conclusions.

II. CLASSICAL MODELLING OF NOISY QUANTUM HARDWARE

Hardware devices and systems for quantum information processing are complex, and the process of definition of an optimal workflow to design and optimise a quantum processor is still in part a matter of trial and error in development. Accordingly, a comprehensive classical simulation of their behaviour — an essential step to empower the understanding of the parameters that impact the performance that is still an open problem [48] in both industry and academy — must include different levels of abstraction, starting from the physical level, moving to the device level and up to the system level. On the one hand, it should include low-level multiphysics simulators [16], [17], [44], [45], [46], [49] for the accurate characterization of the devices, on the other, it must be able to handle involved quantum algorithms, reducing the required resources in terms of RAM and CPU time, as discussed in [20]. The quantum simulation toolchain envisioned in this article is hoped to be a first step towards the development of a design infrastructure that, leveraging existing physical simulators and novel compact models, could mimic the well-established multi-level design procedure routinely employed in classical electronics by bridging the gap between technology and applications, thus paving the way for the practical engineering of quantum systems. As pictorially reported in Figure 2, the relevant physical parameters — such as Zeeman splittings, T_1 and T_2^* time constants, J-couplings and many-body singlet-triplet splitting, g-factors, chemical shieldings, Coulomb on-site interaction and several others — can be extracted from the experimental characterisation of the quantum devices or by exploiting FEM and ab-initio simulators. The downstream *intermediate-level* simulation infrastructure is provided with the acquired device parameters and with several technology-dependent control parameters — such as the static magnetic field, the microwave or radiofrequency electromagnetic fields and the phase and duration of quantum gates. Moreover, in an application-driven scenario where quantum computing is going to be employed for facing real-world problems, manual quantum algorithm optimisation is unfeasible. Hence, the input quantum circuit, described in OpenQASM 2.0 — standard de facto for quantum algorithms —, is handled by a technology-aware compilation utility that translates the abstract input description into one compliant with the target coupling graph and gate native set, carrying out a technology-inspired logic — proposed in a previous article [50] — and layout synthesis, trying, at the same time, to reduce the number of gates, by introducing some fine-grain technology-dependent optimisations. The

resulting output is a quantum circuit built to work smoothly with the target device, tailored to properly optimise specific performance parameters. Then, the noisy-compact model infrastructure carries out an ideal (state vector) and a noisy (density matrix, cf. Appendix) simulation and delivers in the output the probability distribution of the eigenstates and some performance metrics, such as the fidelity [51] and the expected execution time on the target hardware device.

The research presented in this article examines the implementation of a preliminary multi-level simulation toolchain for semiconductor-based quantum dots.

III. FROM PHYSICAL PRINCIPLES TO COMPACT MODEL
A. THE PHYSICAL, THE COMPUTATIONAL AND THE CANONICALLY ORDERED EIGENBASES

Focusing on gate-defined spin-$\frac{1}{2}$ qubits in quantum dots, the spin angular momentum operator of an electron is $\boldsymbol{S}$, and its component along the $\hat{z}$ direction is $S_z = \frac{\hbar}{2}\sigma_z$ [52], where σ_z is the Pauli z-matrix. Hence, S_z is diagonal over the *ordered* eigenbasis $\{|\uparrow\rangle, |\downarrow\rangle\}$. If a static magnetic field $\boldsymbol{B_0} = B_0\hat{z}$ is applied to the system, then the Hamiltonian describing the interaction between the field and the spin magnetic moment $\boldsymbol{m} = \gamma\boldsymbol{S}$ [53] is $\mathcal{H}_0' = \frac{E_z}{2}\sigma_z$ [53], where $E_z = -\hbar\gamma B_0$ is the **Zeeman** energy splitting between the spin-up and spin-down states, $\gamma = -g\mu_B/\hbar$, μ_B is the Bohr magneton and g is the electron *spin g-factor* [54]. In a semi-classical picture [52], the effect of the Zeeman Hamiltonian can be interpreted as a spin precession about the axis along which the static field is applied, at the vector Larmor angular frequency $\boldsymbol{\omega_0} = -\gamma\boldsymbol{B_0}$, where $|\boldsymbol{\omega_0}| = \omega_0 = |\gamma|B_0$, and the sign depends on the sign of g. Therefore:

- **Positive** $g \longrightarrow$ negative $\gamma \longrightarrow$ positive E_z and positive direction of $\boldsymbol{\omega_0} \longrightarrow$ positive precession about the $\hat{z}$ axis. This is the case for instance of silicon, that has $g \sim +2$ [54]. Therefore, the $|\downarrow\rangle$ state is the spin **ground state**, since its energy is reduced by $|E_z|/2$, whereas the first excited spin state is $|\uparrow\rangle$, whose energy is increased by $|E_z|/2$.
- **Negative** $g \longrightarrow$ positive $\gamma \longrightarrow$ negative E_z and negative direction of $\boldsymbol{\omega_0} \longrightarrow$ negative precession about the $\hat{z}$ axis. This is the case for instance of GaAs, that has $g \sim -0.44$ [54]. Therefore, the $|\uparrow\rangle$ state is the spin **ground state**, since its energy is reduced by $|E_z|/2$, whereas the first excited spin state is $|\downarrow\rangle$, whose energy is increased by $|E_z|/2$.

Since the abstract qubit state $|0\rangle$ is mapped to the lower physical energy state and vice versa for $|1\rangle$, focusing on **positive-g-factor** materials (i.e., silicon and germanium), the ordered physical eigenbasis $\{|\uparrow\rangle, |\downarrow\rangle\}$ corresponds to the ordered computational basis $\{|1\rangle, |0\rangle\}$. However, for historical reasons — the physical spin ground state of one of the first technologies employed, namely the Nuclear Magnetic Resonance (NMR), is $|\uparrow\rangle$ [20] — the ordered *canonical* basis customarily employed in the field of quantum computation is $\{|0\rangle, |1\rangle\}$. Therefore, a change of basis

through a unitary matrix $U_B = \sigma_x$ is needed to make the description compliant with the canonical formalism adopted in the simulation infrastructure discussed in this article and in [20]. The system spin Hamiltonian in the $\{|\downarrow\rangle, |\uparrow\rangle\}$ basis is

$$\mathcal{H}_0 = U_B \mathcal{H}_0' U_B^\dagger = \sigma_x \mathcal{H}_0' \sigma_x^\dagger = -\frac{E_z}{2}\sigma_z \qquad (1)$$

After this change of basis, the spin rotates about $\boldsymbol{B}_0$ in the opposite way with respect to Larmor precession, i.e., the same verse as in NMR. The superimposition of a micro-wave magnetic field applied along $+\hat{x}$ axis with angular frequency ω_w, phase ϕ and amplitude $2B_w$ allows the transitions between the hyperfine Zeeman levels. The corresponding micro-wave Hamiltonian in the physical basis is

$$\mathcal{H}_w' = -\boldsymbol{m} \cdot \boldsymbol{B}_w = -2\gamma B_w \cos(\omega_w t - \phi)\frac{\hbar}{2}\sigma_x . \qquad (2)$$

Moving to the $\{|\downarrow\rangle, |\uparrow\rangle\}$, the total single-qubit Hamiltonian becomes

$$\begin{aligned}
\mathcal{H} &= \sigma_x \left(\mathcal{H}_w' + \mathcal{H}_0'\right)\sigma_x^\dagger \\
&= -\frac{E_z}{2}\sigma_z + \hbar\omega_* \cos(\omega_w t - \phi)\sigma_x ,
\end{aligned} \qquad (3)$$

which is formally equivalent to [20, Section 3.1] with the Rabi frequency $\omega_* = |\gamma|B_w = -\gamma B_w$, considering the negative sign of γ. As discussed in [20, Section 3.3], moving to the interaction picture — i.e., to a frame rotating in the negative verse about $\hat{z}$ axis at angular frequency ω_f via the linear operator $U_R = R_z(\omega_f t)$ where the Hamiltonian is $\widetilde{\mathcal{H}} = U_R \mathcal{H} U_R^\dagger - i\hbar U_R \partial_t U_R^\dagger$ [55] — and applying the rotating-wave approximation (RWA) under the assumption that $\omega_w = \omega_f$ leads to the following time-independent single-qubit Hamiltonian:

$$\widetilde{\mathcal{H}} = \frac{\hbar}{2}\left\{\delta\sigma_z + \omega_*[\cos(\phi)\sigma_x + \sin(\phi)\sigma_y]\right\} , \qquad (4)$$

where $\delta = \omega_w - \omega_0$ (cf. Appendix for a discussion about the different approaches adopted to solve systems with and without Hamiltonians with explicit time dependence).

B. DOUBLE COUPLED QUANTUM DOTS
1) THE FERMI-HUBBARD MODEL

In the setting of quantum field theory, an interacting Fermi Gas subjected to a confining potential is well described by the Fermi-Hubbard model. Since a double-quantum dot system with two electrons is a many-body system of fermions, the Fermi-Hubbard model is an effective choice that can describe the relatively complex physics with simplicity and thus a reasonable starting point for the derivation of a compact model. The simplest — yet widely adopted [56], [57], [58] — Fermi-Hubbard model leads to the following formal laboratory-frame Hamiltonian [57], [59]:

$$\mathcal{H}' = \mathcal{H}_\epsilon + \mathcal{H}_v + \mathcal{H}_u + \mathcal{H}_t + \mathcal{H}_z , \qquad (5)$$

where $\mathcal{H}_\epsilon$ takes into account the on-site energy, $\mathcal{H}_v$ the valley degeneracy, $\mathcal{H}_u$ the on-site Coulomb energy, $\mathcal{H}_t$

the tunneling and $\mathcal{H}_z$ the Zeeman energy. Henceforth, the following notation is exploited: $\sigma = \uparrow, \downarrow$ is the index for spin eigenstates, $v = \pm$ for the z-valleys and k for the dot site. Considering N_R electrons in the right dot and N_L in the left dot, the singlet and triplet states are denoted $S(N_L,N_R)$, $T_+(N_L,N_R)$, $T_0(N_L,N_R)$ and $T_-(N_L,N_R)$, where, S stands for singlet state, and the three T notations are related to the three possible values of the eigenvalue of the spin operator M: +1, 0 and −1, respectively.

For a two-qubit system with two electrons in two quantum dots, the ordered physical basis is $\{|\uparrow\rangle, |\downarrow\rangle\} \otimes \{|\uparrow\rangle, |\downarrow\rangle\}$ $= \{|T_+(1,1)\rangle = |\uparrow\uparrow\rangle, |\uparrow\downarrow\rangle, |\downarrow\uparrow\rangle, |T_-(1,1)\rangle = |\downarrow\downarrow\rangle\}$. The many-body singlet $|S(2,0)\rangle$ and $|S(0,2)\rangle$ states need to be considered too [57], since they strongly couple to the $|S(1,1)\rangle = \frac{1}{\sqrt{2}}(|\uparrow\downarrow\rangle - |\downarrow\uparrow\rangle)$ energy state, whereas the $|T(2,0)\rangle$ and $|T(0,2)\rangle$ states are at significantly higher energies and can be neglected [56]. Hence, the complete ordered physical basis is

$$\begin{aligned}
\{|T_+(1,1)\rangle &= |\uparrow\uparrow\rangle, |\uparrow\downarrow\rangle, |\downarrow\uparrow\rangle, \\
|T_-(1,1)\rangle &= |\downarrow\downarrow\rangle, |S(0,2)\rangle, |S(2,0)\rangle\}.
\end{aligned} \qquad (6)$$

Under this hypothesis and considering that, in silicon, the natural ground state is $|\uparrow\uparrow\rangle$, as shown in Appendix, the six-level Fermi Hubbard Hamiltonian [56], [57], [58] matrix form of Equation (5) is:

$$\mathcal{H}_H' = \begin{bmatrix} \overline{E}_z & 0 & 0 & 0 & 0 & 0 \\ 0 & \frac{\Delta E_z}{2} & 0 & 0 & t_0 & t_0 \\ 0 & 0 & -\frac{\Delta E_z}{2} & 0 & -t_0 & -t_0 \\ 0 & 0 & 0 & -\overline{E}_z & 0 & 0 \\ 0 & t_0 & -t_0 & 0 & U-\epsilon & 0 \\ 0 & t_0 & -t_0 & 0 & 0 & U+\epsilon \end{bmatrix}, \qquad (7)$$

where the Coulomb on-site interaction energy U is assumed to be equal for the two dots, t_0 is the inter-dot tunnel coupling, ϵ is the detuning, $\overline{E}_z = \frac{E_z^0 + E_z^1}{2}$ and $\Delta E_z = E_z^1 - E_z^0$ are the average and the difference of the qubits Zeeman splittings, respectively, with $E_z^1 \neq E_z^0$ to allow for single-qubit addressability in a many-qubit quantum register. The energy diagram — i.e., the plot of the eigenvalues of Equation (7) with respect to the detuning ϵ —, reported in Figure 3 for a reasonable set of physical parameters (cf. Table 7), allows the identification of two regimes of control parameters ϵ and t_0 that enable the execution of single-qubit and two-qubit gates, respectively. The Pauli exclusion principle prevents the transition between the spin-triplet states with one electron in each dot ($|T_+(1,1)\rangle = |\uparrow\uparrow\rangle$ and $|T_-(1,1)\rangle = |\downarrow\downarrow\rangle$) to the singlet states with two electrons in the same dot ($|S(2,0)\rangle$ and $|S(0,2)\rangle$) [60]. Accordingly, $|\uparrow\uparrow\rangle$ and $|\downarrow\downarrow\rangle$ in Figure 3 do not interact with $|S(2,0)\rangle$ and $|S(0,2)\rangle$, and their energies are constant for every value of the detuning. Conversely, the antiparallel spin states shift downward in energy as $|\epsilon|$ approaches the numerical value of U since they contain an $|S(1,1)\rangle$ component, and the $|S(1,1)\rangle$ state has an avoided crossing with the $|S(0,2)\rangle$ and $|S(2,0)\rangle$ states [56], due to the
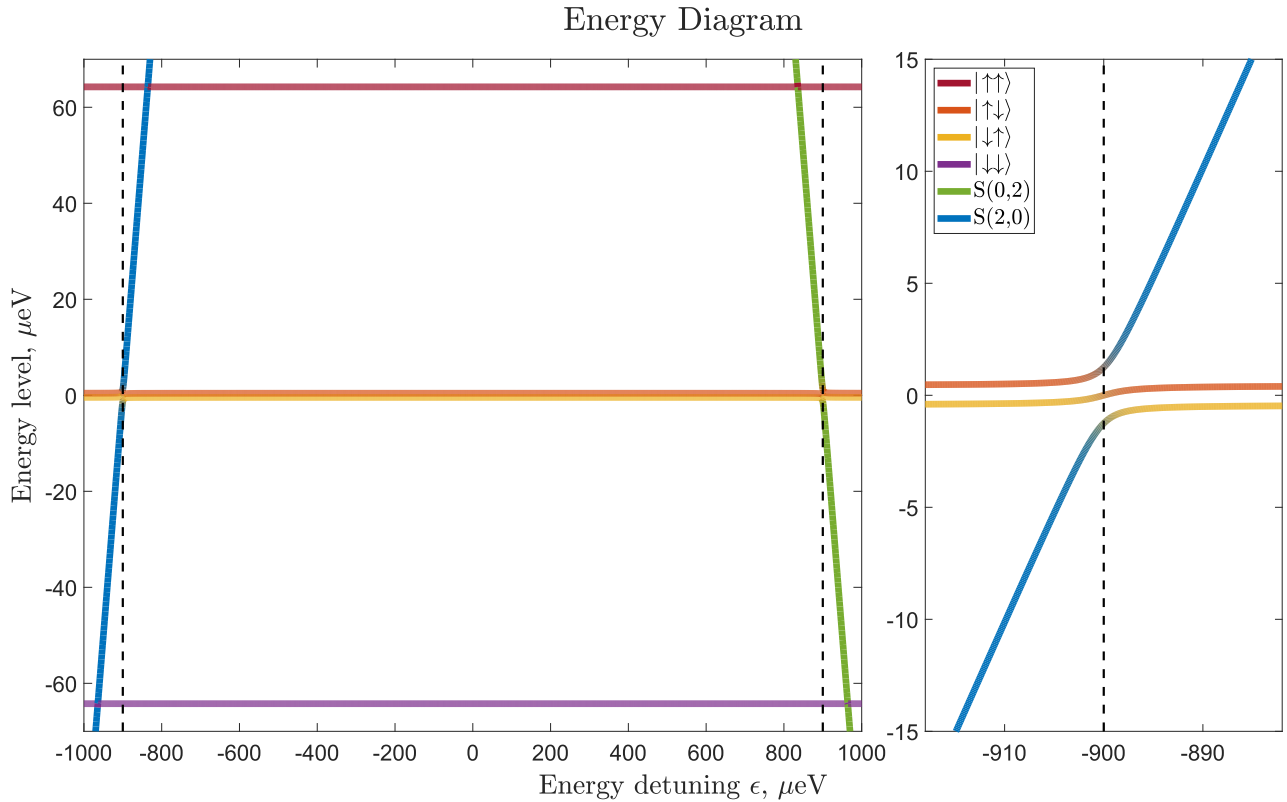
FIGURE 3. Energy diagram of a double quantum dot system with respect to the detuning ϵ. The diagram assumes $U = 0.9$ meV, $t_0 = 1.65$ μeV, $\bar{E}_z = 64.25$ μeV and $\Delta E_z = 868.49$ neV (cf. the CPHASE regime parameters for SiMOS heterostructure of Table 7).

finite interdot tunnelling t_0. Near $|\epsilon| \sim 0$ or for $|\epsilon| \gg U$, the eigenstates of the Hamiltonian correspond to the physical basis states (uncoupled spins), whereas for $|\epsilon| \sim U$ (dashed black lines) they are a linear superposition of the basis states (coupled spins), as pictorially represented by mixed colours in Figure 3.

Near the transition zones, that is for $|\epsilon| \to U$ — i.e., when the difference between the chemical potentials is similar to the on-site electron repulsion —, the resonance frequency of each qubit depends on the state of the *other* qubit, a conditional change that is needed to implement two-qubit gates. Let:

- $f_0^{\downarrow} = \frac{1}{h}\left(E_{|\downarrow\uparrow\rangle} - E_{|\downarrow\downarrow\rangle}\right)$: the resonance frequency of q_0 when q_1 is in $|\downarrow\rangle$;
- $f_0^{\uparrow} = \frac{1}{h}\left(E_{|\uparrow\uparrow\rangle} - E_{|\uparrow\downarrow\rangle}\right)$: the resonance frequency of q_0 when q_1 is in $|\uparrow\rangle$;
- $f_1^{\downarrow} = \frac{1}{h}\left(E_{|\uparrow\downarrow\rangle} - E_{|\downarrow\downarrow\rangle}\right)$: the resonance frequency of q_1 when q_0 is in $|\downarrow\rangle$;
- $f_1^{\uparrow} = \frac{1}{h}\left(E_{|\uparrow\uparrow\rangle} - E_{|\downarrow\uparrow\rangle}\right)$: the resonance frequency of q_1 when q_0 is in $|\uparrow\rangle$.

The behaviour of the resonance frequencies for different values of ϵ is reported in Figure 4. As expected, as $|\epsilon|$ approaches the transition regions, the difference between $f_0^{\downarrow}$ and $f_0^{\uparrow}$ (similarly for $f_1^{\downarrow}$ and $f_1^{\uparrow}$) increases. The Heisenberg exchange interaction parameter J [37] can be computed

as [21]:

$$
\begin{aligned}
J(\epsilon) &= f_0^{\uparrow} - f_0^{\downarrow} = f_1^{\uparrow} - f_1^{\downarrow} \\
&= \frac{1}{h}\left(E_{|\uparrow\uparrow\rangle} - E_{|\uparrow\downarrow\rangle} - E_{|\downarrow\uparrow\rangle} + E_{|\downarrow\downarrow\rangle}\right),
\end{aligned} \tag{8}
$$

and Figure 5 shows the behaviour of $J(\epsilon)$ as a function of the detuning. For low detuning ($\epsilon \sim 0$) the system behaves as two *uncoupled* quantum dots: the eigenstates of the Fermi Hubbard Hamiltonian correspond to the physical computational basis, the resonance frequencies have their nominal values and the J interaction is negligible. Under this regime, **single-qubit** quantum gates can be implemented. On the other hand, for large detuning ($|\epsilon| \to U$), the system consists of two *coupled* quantum dots: the eigenstates of the Fermi Hubbard Hamiltonian are a linear superposition of natural computational basis, the resonance frequencies shifts from their nominal values and the J interaction rises. This regime allows the execution of **two-qubit** quantum gates.

From the above discussion, it follows that the exchange interaction can be *turned on and off* on demand, thus allowing an easy switch from the single-qubit gate to the two-qubit gate regime and vice versa. The value of J can be finely controlled through the application of opportunely engineered voltages on the device plunger gates (that control the **detuning**) or by modifying the **tunnel coupling** t_0 (a larger t_0 leads to an increased bending of the Fermi Hubbard Hamiltonian

Exchange Diagram
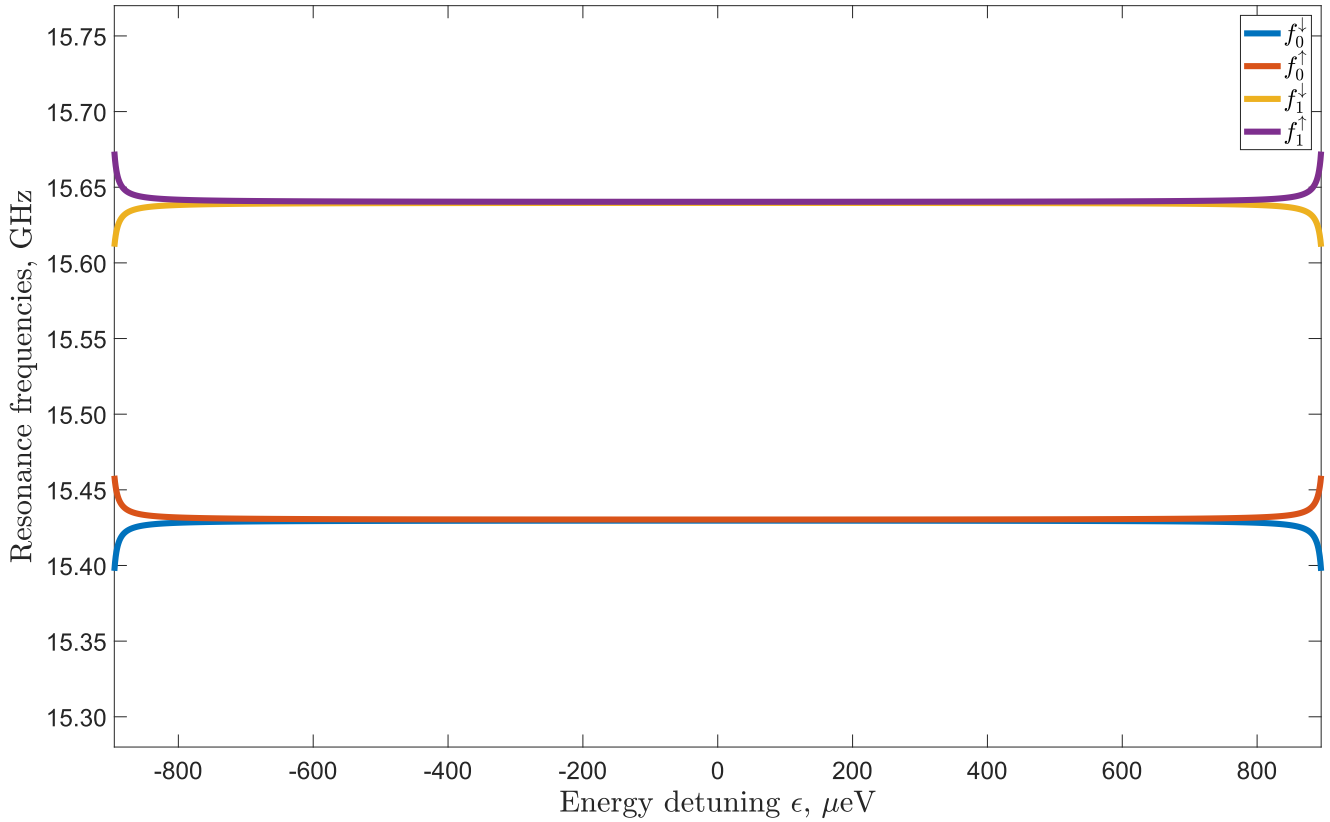
FIGURE 4. Frequency diagram of a double quantum dot system with respect to the detuning ϵ. The diagram assumes $U = 0.9$ meV, $t_0 = 1.65$ μeV, $\overline{E}_z = 64.25$ μeV and $\Delta E_z = 868.49$ neV (cf. the CPHASE regime parameters for SiMOS heterostructure of Table 7).

eigenstates in the transition region, because of avoided crossing).

2) THE LABORATORY-FRAME EFFECTIVE HAMILTONIAN

As discussed in Appendix, under the hypothesis that [56], [61] $U - \epsilon \gg t_0$, the Schrieffer-Wolff (SW) transformation can be used to project the six-level Fermi Hubbard Hamiltonian to the low-energy physical four-state basis $\{|\uparrow\uparrow\rangle, |\uparrow\downarrow\rangle, |\downarrow\uparrow\rangle, |\downarrow\downarrow\rangle\}$ to the first order, obtaining

$$\mathcal{H}'_{SW} = \begin{bmatrix} \overline{E}_z & 0 & & \\ 0 & \frac{\Delta E_z}{2} - \alpha(\Delta E_z) & & \\ 0 & \beta(\Delta E_z) & & \\ 0 & 0 & & \end{bmatrix}$$

$$\begin{matrix} 0 & 0 \\ \beta(\Delta E_z) & 0 \\ -\frac{\Delta E_z}{2} - \alpha(-\Delta E_z) & 0 \\ 0 & -\overline{E}_z \end{matrix} \Bigg], \quad (9)$$

where

$$\alpha(\Delta E_z) \triangleq \frac{t_0^2}{U - \epsilon - \frac{\Delta E_z}{2}} + \frac{t_0^2}{U + \epsilon - \frac{\Delta E_z}{2}}$$

$$\beta(\Delta E_z) \triangleq \frac{\alpha(\Delta E_z) + \alpha(-\Delta E_z)}{2} \quad (10)$$

take into account the $|S(2,0)\rangle$ and $|S(0,2)\rangle$ states effect on the system. If $|\epsilon| \ll U$ and $\Delta E_z \ll U$, then [56]

$$\alpha(\Delta E_z) \sim \beta(\Delta E_z) \sim \frac{2t_0^2}{U} = \frac{hJ}{2}. \quad (11)$$

Hence, α and β map the effect of the exchange interaction J to the four-state SW Hamiltonian. One should consider that ΔE_z only slightly influences the value of α and β, since ΔE_z is usually in the range 1×10^{-6} eV to 1×10^{-8} eV, whereas U and ϵ routinely assume values in the meV scale [56].

As discussed in Section III-A, a change of basis is required to be compliant with the canonical basis. For a two-qubit Hamiltonian, the change of basis matrix is $U_B = \sigma_x \otimes \sigma_x$. The result of the transformation is the $\mathcal{H}_{SW}$ Hamiltonian in the $\{|\downarrow\downarrow\rangle, |\downarrow\uparrow\rangle, |\uparrow\downarrow\rangle, |\uparrow\uparrow\rangle\} = \{|00\rangle, |01\rangle, |10\rangle, |11\rangle\}$ computational basis.

3) THE ROTATING-FRAME EFFECTIVE HAMILTONIAN

In analogy with Section III-A, the superposition of an alternating micro-wave magnetic field to a double quantum dot system leads to

$$\mathcal{H}_w = -\frac{\hbar}{2} \cdot 2B_w \cos(\omega_w t - \phi) \left[\gamma_0 \mathbb{I} \otimes \sigma_x + \gamma_1 \sigma_x \otimes \mathbb{I} \right]. \quad (12)$$

Defining the Rabi frequency of the i-th qubit (denoted as q_i) as $\omega_*^i = |\gamma_i| B_w = -\gamma_i B_w$, the complete Hamiltonian $\mathcal{H} =$

Exchange

FIGURE 5. Exchange diagram of a double quantum dot system with respect to the detuning ϵ. The diagram assumes $U = 0.9$ meV, $t_0 = 1.65\,\mu$eV, $\overline{E}_z = 64.25\,\mu$eV and $\Delta E_z = 868.49$ neV (cf. the CPHASE regime parameters for SiMOS heterostructure of Table 7).

$\mathcal{H}_{SW} + \mathcal{H}_w$ in the laboratory frame is:

$$
\mathcal{H} = \begin{bmatrix} -\overline{E}_z & \frac{\hbar}{2}\omega_*^0\eta \\ \frac{\hbar}{2}\omega_*^0\eta & -\frac{\Delta E_z}{2} - \alpha\left(-\Delta E_z\right) \\ \frac{\hbar}{2}\omega_*^1\eta & \beta\left(\Delta E_z\right) \\ 0 & \frac{\hbar}{2}\omega_*^1\eta \end{bmatrix}
$$

$$
\begin{bmatrix} \frac{\hbar}{2}\omega_*^1\eta & 0 \\ \beta\left(\Delta E_z\right) & \frac{\hbar}{2}\omega_*^1\eta \\ \frac{\Delta E_z}{2} - \alpha\left(\Delta E_z\right) & \frac{\hbar}{2}\omega_*^0\eta \\ \frac{\hbar}{2}\omega_*^0\eta & \overline{E}_z \end{bmatrix}, \quad (13)
$$

where $\eta = \left(e^{i\omega_w t}e^{-i\phi} + e^{-i\omega_w t}e^{i\phi}\right)$. Equation (13) shows an explicit time dependence. Accordingly, the determination of the time evolution of the system (given by the formal solution of Equation (70)) is extremely CPU and memory-demanding. The development of a light compact model requires introducing a methodology and some approximations, valid in specific ranges, to remove this time dependence. As done also in [20, Section 3.3], the first step is to bring the system into the interaction picture. Among the possible different choices for the rotating frame transformation operator, the most convenient one for the purposes of this work is $U_R = R_z(\omega_0^1 t) \otimes R_z(\omega_0^0 t)$, where ω_0^i is the Larmor frequency of qubit q_i. Accordingly, under resonance condition $\omega_w = \omega_0^0$ with q_0,

the exact rotating frame spin Hamiltonian is

$$
\begin{aligned}
\widetilde{\mathcal{H}} &= U_R \mathcal{H} U_R^\dagger - i\hbar U_R \partial_t U_R^\dagger \\
&= \frac{\hbar}{2}\Bigg\{ \omega_*^0 \left[\cos\left(2\omega_0^0 t - \phi\right) + \cos(\phi)\right] \mathbb{I} \otimes \sigma_x \\
&\quad + \omega_*^0 \left[\sin\left(2\omega_0^0 t - \phi\right) + \sin(\phi)\right] \mathbb{I} \otimes \sigma_y \\
&\quad + \omega_*^1 \left[\cos(\Omega t - \phi) + \cos(\Delta\omega_0 t + \phi)\right] \sigma_x \otimes \mathbb{I} \\
&\quad + \omega_*^1 \left[\sin(\Omega t - \phi) + \sin(\Delta\omega_0 t + \phi)\right] \sigma_y \otimes \mathbb{I} \Bigg\} \\
&\quad + \widetilde{\mathcal{H}}_J.
\end{aligned} \quad (14)
$$

where $\Delta\omega_0 = \omega_0^1 - \omega_0^0$, $\Omega = \omega_0^0 + \omega_0^1$ and

$$
\widetilde{\mathcal{H}}_J = \begin{bmatrix} 0 & 0 & 0 & 0 \\ 0 & -\alpha\left(-\Delta E_z\right) & \beta\left(\Delta E_z\right)e^{-i\Delta\omega_0 t} & 0 \\ 0 & \beta\left(\Delta E_z\right)e^{i\Delta\omega_0 t} & -\alpha\left(\Delta E_z\right) & 0 \\ 0 & 0 & 0 & 0 \end{bmatrix}. \quad (15)
$$

It shall be remarked that Equation (14) still shows an explicit time dependence. Removing the latter requires introducing some approximations, which are discussed and verified in the following.

Probability of $|\uparrow\downarrow\rangle$

FIGURE 6. Probability of the $|\uparrow\downarrow\rangle$ component in one of the antiparallel eigenstates as a function of ΔE_z for different values of the detuning ϵ. The diagram assumes $U = 0.9$ meV, $t_0 = 1.65$ µeV, $\bar{E}_z = 64.25$ µeV and $\Delta E_z = 868.49$ neV (cf. the CPHASE regime parameters for SiMOS heterostructure of Table 7).

C. SINGLE-QUBIT GATES IN DOUBLE QUANTUM DOTS

To execute single-qubit gates, the system is brought in a low-detuning low-tunnel coupling regime that yields $\mathcal{H}_J \sim 0$. Then, the micro-wave field $\boldsymbol{B}_w$ is switched on, and the rotating-frame Hamiltonian coincides with Equation (14) with $\mathcal{H}_J \sim 0$. The rotating wave approximation (RWA) [20], [62] — for a time-scale τ_{sq} such that $|\Omega|\tau_{sq} \gg 2\pi$ — leads to

$$\widetilde{\mathcal{H}} \sim \frac{\hbar}{2}\left\{\omega_*^0 \mathbb{I} \otimes \left[\cos(\phi)\sigma_x + \sin(\phi)\sigma_y\right] \right.$$
$$\left. + \omega_*^1 \left[\cos(\Delta\omega_0 t + \phi)\sigma_x + \sin(\Delta\omega_0 t + \phi)\sigma_y\right] \otimes \mathbb{I}\right\}. \quad (16)$$

If the time scale τ_{sq} can be chosen such that $|\Delta\omega_0|\tau_{sq} \gg 2\pi$, then the complex exponentials $e^{\pm i\Delta\omega_0 t \pm i\phi}$ — which describe the **off-resonance** effect — are rapidly oscillating and average to zero. Under this hypothesis, the rotating-frame Hamiltonian can be written as

$$\widetilde{\mathcal{H}} \sim \frac{\hbar\omega_*^0}{2}\left[\cos(\phi)\mathbb{I}\otimes\sigma_x + \sin(\phi)\mathbb{I}\otimes\sigma_y\right], \quad (17)$$

which coincides with the single qubit part of [20, Equation 22] and does not show any time dependence. Therefore, the implementation of single-qubit gates on quantum dots

under the resonance condition is formally modelled as discussed in [20, Section 3.4] for NMR, i.e., resorting on Equation (72) instead of Equation (71). Moreover, thanks to the formal equivalence of the single-qubit expression between NMR and quantum dots, the *Fourier method* proposed in [20, Section 4.1] — which determines the unwanted effective rotations to which not-addressed qubits are subjected — can be effortlessly exploited to provide a computationally inexpensive approach to model the off-resonance effect.

D. TWO-QUBIT GATE IN DOUBLE QUANTUM DOTS

From an operational perspective, a two-qubit gate in a double quantum dot device is implemented as follows:
- The micro-wave field is switched off.
- t_0 is set to the operating value through the barrier gate.
- Engineered voltages are applied to the plunger gates to set the detuning value in the vicinity of U to activate J.
- The detuning is brought back to $t_0 = t_0^{off} \sim 0$ after the time t required to implement the quantum gate.

This operation is fully electrical, as it only necessitates the control of the gate voltages. From a modelling perspective, the resulting rotating-frame Hamiltonian is $\mathcal{H} = \mathcal{H}_J$. In this operating regime, the system can execute two different two-qubit gates [56]: the $\sqrt{\text{SWAP}}$ and the C-PHASE. Which

gate is executed depends on the relative magnitudes of ΔE_z and t_0. Considering the natural basis Fermi Hubbard Hamiltonian of Equation (7) or the laboratory-frame Schrieffer-Wolff Hamiltonian of Equation (9) (under the hypothesis of applicability of the Schrieffer-Wolff transformation, the results are almost identical), the probability of the $|\uparrow\downarrow\rangle$ (or equivalently of $|\downarrow\uparrow\rangle$) component in one of the two antiparallel eigenstates is reported in Figure 6 as a function of ΔE_z for some values of the detuning. When ΔE_z is non-zero but **small** with respect to t_0, the energy eigenstates of Equation (9) are $\{|\downarrow\downarrow\rangle, |\downarrow\uparrow\rangle, |\uparrow\downarrow\rangle, |\uparrow\uparrow\rangle\}$ when $\epsilon \sim 0$, but $\{|\downarrow\downarrow\rangle, |S(1,1)\rangle, |T_0(1,1)\rangle, |\uparrow\uparrow\rangle\}$ for $|\epsilon| \gg 0$. Indeed, Figure 6 shows that for small ΔE_z, the probability of $|\uparrow\downarrow\rangle$ component can range from about 0.5 to about 1 for different values of ϵ. In this range of ΔE_z, the system can implement the two-qubit $\sqrt{\text{SWAP}}$ gate. Conversely, when ΔE_z is **large**, the Hamiltonian eigenstates are $\{|\downarrow\downarrow\rangle, |\downarrow\uparrow\rangle, |\uparrow\downarrow\rangle, |\uparrow\uparrow\rangle\}$ for every $|\epsilon| \ll U$ [56], as it can be ascertained from $\mathcal{P}(|\uparrow\downarrow\rangle) \sim 1 \; \forall |\epsilon| \ll U$ in Figure 6. In this range of ΔE_z, the system can implement the two-qubit **C-PHASE** gate.

1) TWO-QUBIT NATIVE GATE $\sqrt{\text{SWAP}}$
When the difference in Zeeman splittings ΔE_z is *small* and t_0 is *large*, both $\Delta\omega_0$ and the execution time t (that is inversely proportional to J) are small. More in detail, if

$$\Delta\omega_0 t \sim 2\pi\Delta f_0 \cdot \frac{h}{4\beta} \sim \frac{\pi}{4} \cdot \frac{\Delta E_z U}{t_0^2} \to 0, \qquad (18)$$

then the complex exponentials $e^{\pm i\Delta\omega_0 t}$ of $\mathcal{H}_J$ can be approximated by the zero-order Maclaurin polynomial $e^{\pm i\Delta\omega_0 t} \sim 1$. Then, the rotating-frame two-qubit Hamiltonian reduces to

$$\widetilde{\mathcal{H}} \sim \begin{bmatrix} 0 & 0 & 0 & 0 \\ 0 & -\alpha(-\Delta E_z) & \beta(\Delta E_z) & 0 \\ 0 & \beta(\Delta E_z) & -\alpha(\Delta E_z) & 0 \\ 0 & 0 & 0 & 0 \end{bmatrix}$$
$$= \frac{\beta(\Delta E_z)}{2} \cdot (\sigma_x \otimes \sigma_x + \sigma_y \otimes \sigma_y + \sigma_z \otimes \sigma_z - \mathbb{I} \otimes \mathbb{I}) +$$
$$\frac{\alpha(\Delta E_z) - \alpha(-\Delta E_z)}{4} \cdot (\sigma_z \otimes \mathbb{I} - \mathbb{I} \otimes \sigma_z), \qquad (19)$$

which does not show any explicit time dependence. Since $\widetilde{\mathcal{H}}$ has a non-zero trace, it cannot be reduced to a generalised traceless Pauli vector $\hat{n}\sigma$. So, there is no simple analytic relation to determine the corresponding evolution operator. However, numerical exponentiation with

$$t = \tau_{mq} = \frac{h}{4\beta} \sim \frac{1}{2J} \qquad (20)$$

leads to

$$U = \exp\left(-\frac{i}{\hbar}\widetilde{\mathcal{H}}t\right)\Bigg|_{t=\frac{h}{4\beta}}$$
$$\sim \begin{bmatrix} 1 & 0 & 0 & 0 \\ 0 & 0 & 1 & 0 \\ 0 & 1 & 0 & 0 \\ 0 & 0 & 0 & 1 \end{bmatrix} = \text{SWAP}. \qquad (21)$$

Therefore, halving the duration of the gate, a $\sqrt{\text{SWAP}}$ gate can be achieved:

$$U = \exp\left(-\frac{i}{\hbar}\widetilde{\mathcal{H}}t\right)\Bigg|_{t=\frac{h}{8\beta}}$$
$$\sim \begin{bmatrix} 1 & 0 & 0 & 0 \\ 0 & \frac{1+i}{2} & \frac{1-i}{2} & 0 \\ 0 & \frac{1-i}{2} & \frac{1+i}{2} & 0 \\ 0 & 0 & 0 & 1 \end{bmatrix} = \sqrt{\text{SWAP}}. \qquad (22)$$

Assuming that q_t is the target qubit and q_c the control qubit, the $\sqrt{\text{SWAP}}$ gate can be used to implement a CNOT gate:

$$\text{CNOT}_{c,t} = H_t R_{Z_t}\left(\frac{\pi}{2}\right) R_{Z_c}\left(-\frac{\pi}{2}\right)$$
$$\sqrt{\text{SWAP}} R_{Z_t}(\pi) \sqrt{\text{SWAP}} H_t, \qquad (23)$$

where the symbol A_i denotes a quantum gate A acting on qubit q_i.

2) TWO-QUBIT NATIVE GATE C-PHASE
When the difference in Zeeman splittings ΔE_z is *large* and t_0 is *small* (similar to the weak coupling condition for NMR, cf. [20]), then

$$\Delta\omega_0 t \sim 2\pi\Delta f_0 \cdot \frac{h}{4\beta} \sim \frac{\pi}{4} \cdot \frac{\Delta E_z U}{t_0^2} \to \infty. \qquad (24)$$

Accordingly, the complex exponentials of $\mathcal{H}_J$ are rapidly oscillating and average to zero $e^{-i\Delta\omega_0 t} \sim 0$. Then, the rotating-frame two-qubit Hamiltonian reduces to

$$\widetilde{\mathcal{H}} \sim \begin{bmatrix} 0 & 0 & 0 & 0 \\ 0 & -\alpha(-\Delta E_z) & 0 & 0 \\ 0 & 0 & -\alpha(\Delta E_z) & 0 \\ 0 & 0 & 0 & 0 \end{bmatrix}$$
$$= \frac{\beta(\Delta E_z)}{2} \cdot (\sigma_z \otimes \sigma_z - \mathbb{I} \otimes \mathbb{I})$$
$$+ \frac{\alpha(\Delta E_z) - \alpha(-\Delta E_z)}{4} \cdot (\sigma_z \otimes \mathbb{I} - \mathbb{I} \otimes \sigma_z). \qquad (25)$$

Being $\widetilde{\mathcal{H}}_{SW}$ diagonal, the time evolution operator has a simple analytic expression

$$U = \exp\left(-\frac{i}{\hbar}\widetilde{\mathcal{H}}t\right) = \begin{bmatrix} 1 & 0 & 0 & 0 \\ 0 & e^{i\frac{t}{\hbar}\alpha(-\Delta E_z)} & 0 & 0 \\ 0 & 0 & e^{i\frac{t}{\hbar}\alpha(\Delta E_z)} & 0 \\ 0 & 0 & 0 & 1 \end{bmatrix}. \qquad (26)$$

Considering that, as mentioned above, the difference between $\alpha(+\Delta E_z)$ and $\alpha(-\Delta E_z)$ is small

$$\alpha(+\Delta E_z) \sim \alpha(-\Delta E_z) \sim \beta(\Delta E_z). \qquad (27)$$

Then, setting the time duration to

$$t = \tau_{mq} = \frac{h}{4\beta} \sim \frac{1}{2J} \qquad (28)$$

one gets

$$U = \exp\left(-\frac{i}{\hbar}\tilde{\mathcal{H}}t\right)\Bigg|_{t=\frac{h}{4\beta}} \sim \begin{bmatrix} 1 & 0 & 0 & 0 \\ 0 & i & 0 & 0 \\ 0 & 0 & i & 0 \\ 0 & 0 & 0 & 1 \end{bmatrix}. \quad (29)$$

Eventually, the C-PHASE gate is achieved by applying a couple of rotations about the $\hat{z}$-axis:

$$\text{C-PHASE} = \begin{bmatrix} 1 & 0 & 0 & 0 \\ 0 & i & 0 & 0 \\ 0 & 0 & i & 0 \\ 0 & 0 & 0 & 1 \end{bmatrix} \left[R_z\left(-\frac{\pi}{2}\right) \otimes \mathbb{I} \right]$$
$$\left[\mathbb{I} \otimes R_z\left(-\frac{\pi}{2}\right) \right]. \quad (30)$$

It is worth highlighting that for this choice of t, the C-PHASE gate is a CZ gate: other controlled-phase rotations can be achieved with different choices for t. The time required to implement a CZ gate is twice as long as the time needed for a $\sqrt{\text{SWAP}}$ gate, but the larger difference in Zeeman splitting reduces the off-resonance errors, thus allowing for higher fidelity. The CNOT gate is obtained as

$$\text{CNOT}_{c,t} = H_t\, \text{CZ}\, H_t. \quad (31)$$

E. VERIFICATION OF THE PROPOSED APPROXIMATIONS

The approximations discussed in the previous paragraphs are employed to obtain a time-independent two-qubit Hamiltonian. These assumptions are validated through a comparison between the output density matrix computed by the MATLAB compact model and the one calculated from the solution of the Lindblad master equation, carried out using the Python-base environment QuTiP [15]. The two matrices are going to be addressed as ρ_m and ρ_q, respectively. The error percentage $\varepsilon_\%$ due to the compact model approximation is computed as the fidelity between the two density matrices, i.e.

$$\varepsilon_\% \triangleq \left(1 - \text{Tr}\left(\sqrt{\rho_m^{1/2}\, \rho_q\, \rho_m^{1/2}}\right)\right) \cdot 100. \quad (32)$$

The validation has been carried out for several different initial states. The results reported in the following assume that the initial state is

$$\psi_0 = \frac{1}{\sqrt{2}}(|00\rangle + |01\rangle). \quad (33)$$

1) $\sqrt{\text{SWAP}}$ CASE VALIDATION

The input parameters for the simulations are derived from experimental data [63], [64] except for the tunnel coupling t_0, which is extracted from low-level physical simulations in Section IV. The two resonance angular frequencies are $\omega_0^1 = 2\pi f_0^1 = 2\pi(6.9491\,\text{GHz})$ and $\omega_0^0 = 2\pi f_0^0 = 2\pi(6.9601\,\text{GHz})$, which yield $\Delta\omega_0 = 2\pi\Delta f_0 = 2\pi(11\,\text{MHz})$, the Coulomb charging energies of the dots U are both 0.9 meV and the detuning is equal to 0.7 meV. t_0 is

set to 800 MHz.[1] The simulations are performed spanning the t_0 and $\Delta\omega_0$ values around the starting experimental data and the error is plotted in Figure 7a. The two ranges of values are:

- $\Delta\omega_0 = 2\pi\Delta f_0 = 2\pi[6\,\text{MHz} : 16\,\text{MHz}]$;
- $t_0 = [700\,\text{MHz} : 900\,\text{MHz}]$.

The behaviour of the error agrees with the theoretical expectations: indeed, it is minimum for low values of Δf_0 and high t_0 since the gate duration t decreases when t_0 increases. These two conditions yield that the $e^{i\Delta\omega_0 t} \approx 1$ approximation is more accurate, and thus the error is lower. Moreover, in the centre of the plot, where the values derived from the experimental data and from the physical simulations are represented, the error is lower than $\sim 1\%$, meaning that the MATLAB model is quite accurate in the description of a realistic DQD structure with the $\sqrt{\text{SWAP}}$ as the native gate. The model validity is also tested on single-qubit gates, in particular on a $R_X(\pi)$ gate applied on q_0. The duration of the gate is set through the B_1 value to $t = 100\,\text{ns}$, and the error is computed for the same set of ΔE_z values as the two-qubit gate simulation. On the other hand, the value of t_0 is set to 10 Hz [32], which translates into switching off the barrier gate voltage, since in single-qubit gates the exchange interaction must be negligible. As expected, Figure 7b shows that the error decreases when the resonance frequencies are more distant, i.e. when the off-resonance effects are lower. Neglecting the ringing behaviour, the model error for the operating value $\Delta E_z = 11\,\text{MHz}$ is $\sim 5\%$.

2) C-PHASE CASE VALIDATION

The same analysis is performed for the C-PHASE operating regime, using the same type of simulation (see Figure 7c). The input values are again derived from experimental data and physical simulations: the two resonance angular frequencies are $\omega_0^1 = 2\pi f_0^1 = 2\pi(15.43\,\text{GHz})$ and $\omega_0^0 = 2\pi f_0^0 = 2\pi(15.64\,\text{GHz})$, which yield $\Delta\omega_0 = 2\pi\Delta f_0 = 2\pi(210\,\text{MHz})$, the Coulomb charging energies of the dots U are both 0.9 meV, and the detuning is equal to 0.3 meV. t_0 is set to 400 MHz.[2] The two ranges of values are:

- $\Delta\omega_0 = 2\pi\Delta f_0 = 2\pi[50\,\text{MHz} : 300\,\text{MHz}]$;
- $t_0 = [300\,\text{MHz} : 500\,\text{MHz}]$.

In this regime, the approximation introduced is $e^{j\Delta\omega_0 t} \approx 0$, and the plot in Figure 7c shows that the error is minimum for high ΔE_z and low t_0, as expected. The error for the operating experimental values is less than 0.1% meaning that the model describes very precisely this native gate. Again, the single-qubit gate error is also explored for a $R_X(\pi)$ on q_0, setting the gate duration to $t = 15\,\text{ns}$, $t_0 = 10\,\text{Hz}$ and analyzing the same ΔE_z span as the two-qubit gate simulation. The error plot in Figure 7d shows that the single-qubit gate error is significantly lower ($\sim 1\%$). The explanation is straightforward: the C-PHASE scenario yields a higher ΔE_z, which minimises the off-resonance effects, thus

---

[1]This value is reasonable considering the simulations carried out in Section IV.

[2]Again, this value is reasonable considering the simulations carried out in Section IV.

(a) MATLAB-QuTiP error for a $\sqrt{\text{SWAP}}$ gate.

(b) MATLAB-QuTiP error for a $R_X(\pi)$ gate on q_0 in the $\sqrt{\text{SWAP}}$ regime.

(c) MATLAB-QuTiP error for a C-PHASE gate.

(d) MATLAB-QuTiP error for a $R_X(\pi)$ gate on q_0 in the C-PHASE regime.
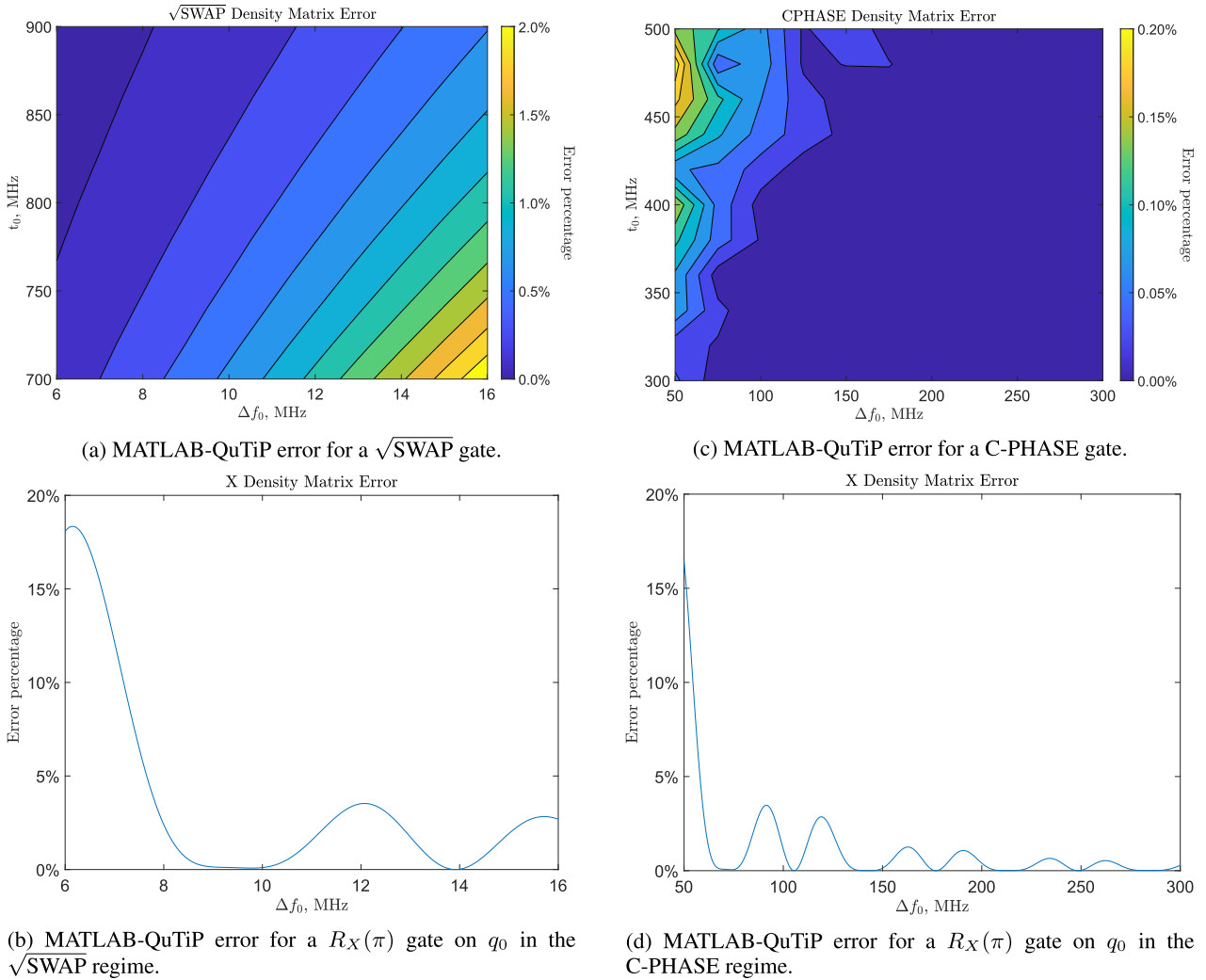
FIGURE 7. MATLAB-QuTiP error for native two-qubit gates and single-qubit gates in the $\sqrt{\text{SWAP}}$ and C-PHASE regimes.

implying that the model can accurately describe single-qubit gates in these operating conditions.

F. NOISE MODEL AND INTEGRATION IN THE SIMULATION INFRASTRUCTURE

1) RELAXATION AND DECOHERENCE

Real-world quantum systems are never completely isolated from the external environment. The resulting interactions between the qubits and the environment pave the way to several non-ideal phenomena [66] that lead to randomisation of the quantum information, thus ultimately limiting achievable performance. In the field of quantum information processing, the description is customarily tackled from a phenomenological perspective, by introducing two *comprehensive* dynamic non-ideality phenomena: **longitudinal** and **transverse relaxation**. The former — which is described in terms of exponential decay ruled by a T_1 time constant — models the loss of energy of a qubit when it is in its excited state thus forcing it to reach the ground state after a transient, whereas the latter — which is also known as decoherence —

represents the dynamic increase of uncertainty about the qubit's phase [51]. The latter phenomenon is customarily described in terms of exponential decay ruled by a T_2 or T_2^* time constant. The difference between the two representations traces back to the NMR formalism [10] and to the different experimental approaches to determine the relevant time constant: Ramsey's experiment leads to T_2^*, whereas the Hahn Echo's one allows the computation of T_2. Since $T_2^* \leq T_2$, the remaining of this article takes into account T_2^*.

Whereas the standard approach prescribes the use of Krauss operators [51], in [20, Section 4.2] a different approach — which reduces the memory requirement but still provides results that are in noteworthy agreement with the classical methodology — is proposed and verified. In a nutshell, this methodology computes decoherence by adding an exponential decay to the off-diagonal terms of the system density matrix, and relaxation through a probability redistribution. The two effects are described separately. The **decoherence** process is modelled by a matrix, computed as the Kronecker product of the decoherence matrices of each of
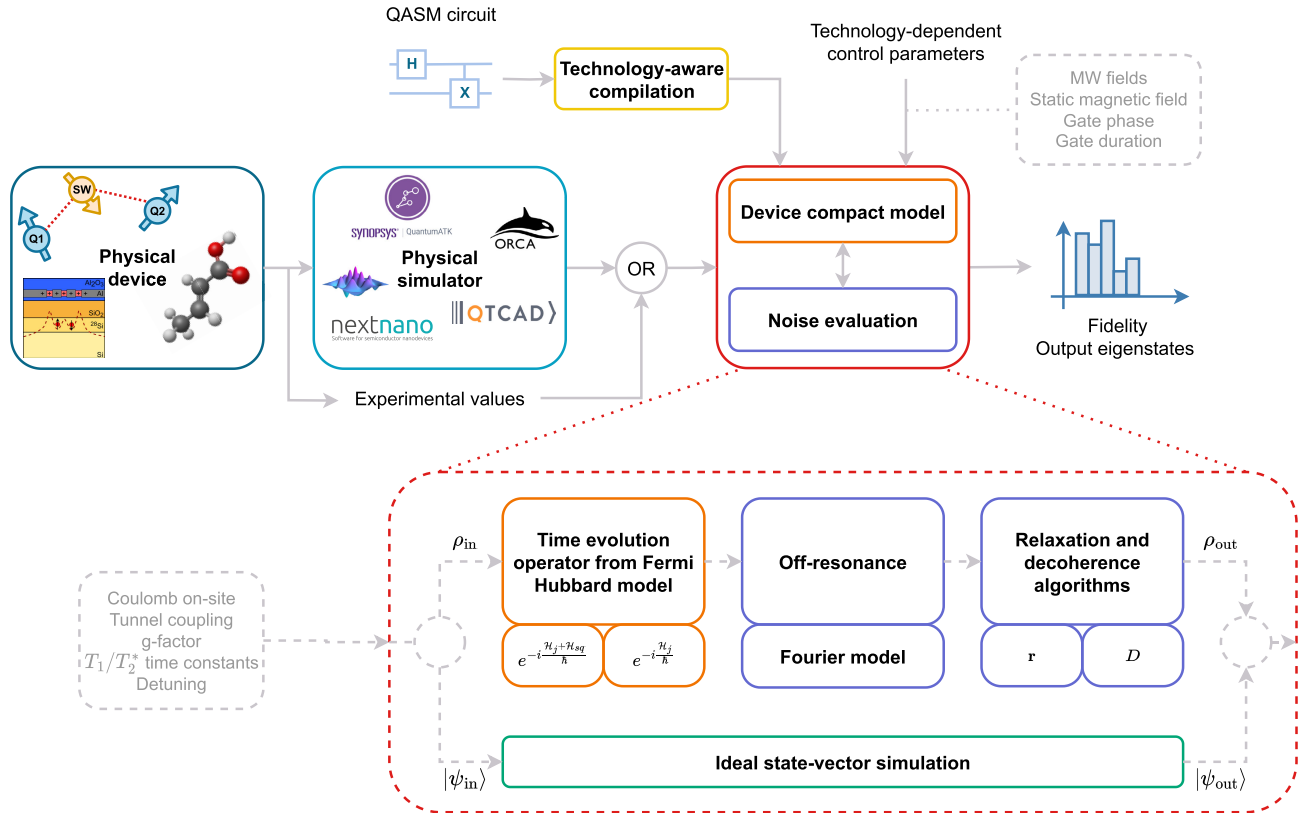
FIGURE 8. Integration of the quantum dot compact model in the quantum simulation toolchain. The symbol $\mathcal{H}_{sq}$ refers to Equation (17); $\mathcal{H}_j$ to one between Equation (19) and Equation (25); r is the relaxation vector of Equation (36) and D is the decoherence matrix of Equation (34).

the n qubit:

$$D = \bigotimes_{i=n-1}^{0} D_i = D_{n-1} \otimes \cdots D_0, \qquad (34)$$

where

$$D_i = \begin{bmatrix} 1 & e^{-\frac{t}{T_{2_i}}} \\ e^{-\frac{t}{T_{2_i}}} & 1 \end{bmatrix}, \qquad (35)$$

where T_{2_i} is the decoherence time constant of the qubit q_i. The whole D matrix is then multiplied *element by element* to the system density matrix ρ. Conversely, the **longitudinal relaxation** process — which is interpreted as a loss of probability of the excited states — is described by a relaxation vector calculated as

$$\boldsymbol{r} = \bigotimes_{i=n-1}^{0} \begin{bmatrix} 1 \\ e^{-\frac{t}{T_{1_i}}} \end{bmatrix} = \begin{bmatrix} r_{0,0}, & r_{1,1}, & \cdots, & r_{2^n-1,2^n-1} \end{bmatrix}^{\mathsf{T}}, \quad (36)$$

where T_{1_i} is the relaxation time constant of the qubit q_i. This vector is multiplied by the main diagonal of the density matrix ρ; then, the total probability lost by the excited states is computed as the sum of each state probability loss:

$$P_{lost_{tot}} = \sum_k P_{lost_k} = \sum_k (1 - r_{k,k}) \rho_{k,k}, \qquad (37)$$

where $\rho_{k,k}$ is the (k,k) element of the density matrix ρ. $P_{lost_{tot}}$ is then redistributed, according to a novel algorithm detailed

in [20, Section 4.2.2], to ensure that the trace of the system density matrix is unitary ($\mathrm{Tr}(\rho) = 1$).

2) INTEGRATION IN THE SIMULATION TOOLCHAIN
As pictorially reported in Figure 8, the compact model for double quantum dot devices discussed in this article is integrated into the multi-technology simulation infrastructure — which at the time of writing supports electron spin manipulation in molecular nanomagnets, nuclear spin manipulation in diamagnetic molecules via NMR and spin manipulation in quantum dots — introduced in [19] and [20] (solid red rectangle), which is in turn integrated into the multi-level simulation toolchain discussed in Section II. As far as quantum dots are concerned (dashed red rectangle), the infrastructure receives in input the following physical parameters:

- Electron g-factor;
- Coulomb on-site repulsion energy U;
- Tunnel coupling t_0;
- Detuning ϵ;
- Relaxation and decoherence time constants T_1 and T_2^*,

and the following control parameters:

- Static magnetic field B_0;
- Micro-wave magnetic field B_w for single-qubit gates;
- Gate phase ϕ for single-qubit gates;
- Gate duration τ for two-qubit gates,

and the compiled version of the quantum circuit. While the control parameters are chosen by the user, the physical ones can be retrieved from experimental data of exploiting low-level simulators (c.f. Section IV). Afterwards, the infrastructure carries out an ideal (state vector) and a noisy simulation (density matrix). The latter exploits the time evolution operators derived from the **Fermi-Hubbard** model for single-qubit gates, C-PHASE and $\sqrt{\text{SWAP}}$. It shall be noted that, when executing two-qubit gates, the time evolution operator is determined via direct matrix exponentiation of Equation (19) or Equation (25), whereas for single-qubit gates it is computed via direct matrix exponentiation of Equation (17) plus one between Equation (19) and Equation (25), according to the operating regime of the device (which is fixed for every run of an algorithm):

$$U_{sq} = \exp\left\{-i\left[\frac{\omega_\pm^0}{2}\left(\cos(\phi)\mathbb{I}\otimes\sigma_x + \sin(\phi)\mathbb{I}\otimes\sigma_y\right) + \frac{\mathcal{H}_J}{\hbar}\right]t\right\}$$

(38)

with

$$\mathcal{H}_J = \begin{cases} \text{Equation (19), if } \Delta E_z \ll t_0 \\ \text{Equation (25), if } \Delta E_z \gg t_0 \end{cases}.$$

(39)

This approach allows the infrastructure to consider the **unwanted residual coupling** — due to non-zero tunnel coupling t_0 — when executing single-qubit gates. Then, the **off-resonance** effects are accounted for by leveraging the Fourier model (cf. Section III-C), and **relaxation** and **decoherence** by exploiting the algorithms mentioned in Section III-F1. Eventually, the comparison between ideal and noisy simulation characterises the fidelity.

IV. PHYSICAL LEVEL SIMULATION

As discussed above and pictorially reported in Figure 8, the compact model proposed in Section III requires several input physical parameters, which can be retrieved by resorting to experimental data or leveraging existing physical simulators. In this article, a hybrid approach is pursued: some physical parameters are obtained through simulations with NextNano [17] and QTCAD [16], others — which are still beyond the reach of currently available simulators — are retrieved from experimental data available in the scientific literature. This section details the procedure followed to simulate some target structures: the first step is the description of the geometry and materials of the structures, as discussed in Section IV-A. Subsequently, one has to define a proper mesh throughout the structure and some boundary conditions for the FEM solvers. As discussed in [67], the next step is the computation of the potential throughout the structure by solving the non-linear Poisson equation. Afterwards, the solution of the single-particle effective-mass Schrödinger equation under the envelope-function approximation [68] allows the determination of the single-particle eigenspectra (bound states, their energy and their probability density). In real-world quantum devices, the overall structure is relatively large and should be divided into

- **Semiclassical** regions: regions where the solution of the non-linear Poisson equation alone allows obtaining a reasonable estimate of electrostatics.
- **Quantum** regions: regions where the Poisson and Schrödinger equations have to be coupled self-consistently.

These steps are outlined in Section IV-B — which reports the simulation results obtained with NextNano for the SiGe heterostructure —, in Section IV-C — which reports the simulation results obtained with QTCAD for the SiGe heterostructure — and in Section IV-D — which reports the simulation results obtained with QTCAD for the SiMOS heterostructure. It has to be noted that the two SiGe heterostructures simulated with QTCAD and NextNano present a different arrangement of the ohmic contacts and the n^+ doped regions to investigate two possible layouts and compare the obtained results. Finally, Table 6 summarizes the main results and the simulation conditions, allowing for a convenient comparison between the different heterostructures taken into consideration and the two software tools.

Section III highlights that modelling double-quantum dot structures is inherently a many-body problem. As outlined in several research articles [49], [69], [70], [71], [72], the accurate and quantitative computation of the on-site Coulomb energy U and the exchange interaction J requires the introduction of a full configuration interaction (full-CI, a post-Hartree Fock method) solver that, exploiting the single-particle wavefunctions determined by the self-consistent Poisson-Schrödinger solver, calculates precise many-particle wave functions and energies within the effective mass approximation. However, on the one hand, at the time of writing, NextNano – differently from QTCAD – does not support a full-CI solver, on the other hand, this post-Hartree Fock method is known to be CPU and memory intensive. Accordingly, even though the determination of many-body wavefunctions remains a relevant future work to be accomplished, this article introduces an approximation for the computation of the tunnel coupling t_0, whereas U is retrieved from experimental data. Indeed, it is known [73] that

$$t_0 \sim \frac{E_1 - E_0}{2},$$

(40)

where E_0 and E_1 are respectively the single-particle ground state and first excited state eigenenergies of a double quantum dot system with zero detuning.

A. SEMICONDUCTOR HETEROSTRUCTURES

Among the different possible heterostructures that can be used to implement quantum dots, this article focuses on a $Si_{0.7}Ge_{0.3} - {}^{28}Si - Si_{0.7}Ge_{0.3}$ heterostructure and on a $Si - {}^{28}Si - SiO_2$ (referred to as SiMOS) heterostructure, as presented in [74]. The geometry of the devices follows directly from the need to achieve 3D electron confinement through two different effects:

- Material engineering along the $\hat{z}$ direction to create a two-dimensional electron gas (2DEG).

(a) SiGe-^{28}Si-SiGe heterostructure.

(b) Si-^{28}Si-SiO$_2$ heterostructure.
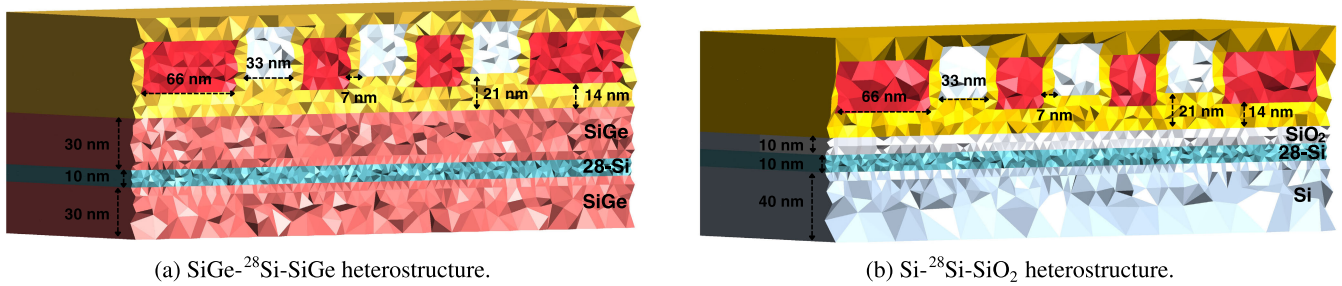
FIGURE 9. Target semiconductor heterostructure devices, obtained with GMSH [65]. The figures report a cut along a plane perpendicular to the XY plane in the quantum region.

- Potential confinement with metal gates to shape the profile of the quantum dots along the $\hat{x}$ and $\hat{y}$ directions.

It is well known that the band diagram of bulk silicon is characterized by a sixfold degenerate conduction band minimum. This sixfold degenerate level is first split into a higher energy fourfold degenerate level and a lower energy twofold degenerate one. In SiMOS, this happens thanks to the 2DEG quantum confinement across the Si/SiO$_2$ [001] interface [75], [76], while, in Si/SiGe structures, this is due to the planar tensile strain in the silicon layer (SiGe has a higher lattice constant than Si) [77]. The further twofold degeneracy is lifted by the sharp confinement potential of the 2DEG quantum well [78], [79], providing a unique spin-degenerate conduction band ground state.

Finally, it shall be highlighted that the mesh is determined with GMSH [65] when working with QTCAD, whereas NextNano has an internal software tool to compute the mesh.

1) SiGe HETEROSTRUCTURE

The description follows Figure 9a and Figure 10a. The heterostructure begins with a 300 nm linearly graded Si$_{1-x}$Ge$_x$ layer, where x ranges from 0 to 0.3.[3] On top of this, a 30 nm relaxed Si$_{0.7}$Ge$_{0.3}$ layer[4] lies below the 10 nm isotopically purified ^{28}Si quantum layer. The latter is separated from the top oxide by a 30 nm relaxed Si$_{0.7}$Ge$_{0.3}$ layer. In experimental devices, the 2 nm Si cap oxidises before the atomic layer deposition of the Al$_2$O$_3$ top oxide layer and therefore it is substituted by a 2 nm SiO$_2$ layer in NextNano and removed in QTCAD. The device utilises a three-layer metal gate stack: Y-gates, plunger gates and barrier gates, as reported in Figure 10a. As described in [74], the metal gates are fabricated with a Ti:Pd gate stack. The 3 nm of Ti are used as an adhesion layer for the Pd deposition, meaning that the gates are mostly made of Pd. For the sake of simplicity, the gates are treated as Pd volumes in the NextNano simulation

setup when choosing the metal workfunction in Section IV-B1. Each metal layer is separated from the below metal layer by a 7 nm oxide layer. The height of Y gates is 20 nm, whereas their width is 106 nm. Above the quantum region, the extension of dot plunger and barrier gates is: 33 nm along $\hat{x}$, 33 nm along $\hat{y}$ and 30 nm along $\hat{z}$. The reservoir plunger gates have a 66 nm extension along $\hat{x}$. Along the $\hat{x}$ axis, the plunger and barrier gates are mutually separated by a 7 nm Al$_2$O$_3$ layer. Along the $\hat{y}$ axis, Y gates are separated from plunger/barrier gates by a 7 nm Al$_2$O$_3$ layer. For the n^+ doped regions and the ohmic contacts, two different arrangements are adopted:

- When using NextNano, two $35 \times 33 \times 42$ nm volumes — including the SiO$_2$ cap, the Si$_{0.7}$Ge$_{0.3}$ layer and the ^{28}Si quantum layer — are n^+ doped, with a dopant concentration of 1×10^{20} cm^{-3}. The two ohmic contacts are located at the discontinuity between the Si cap and the Al$_2$O$_3$.
- When using QTCAD, at the four corners of the structure, four $40 \times 60 \times 45$ nm volumes — including the top Si$_{0.7}$Ge$_{0.3}$ layer, the ^{28}Si quantum layer and a 5 nm thick Si$_{0.7}$Ge$_{0.3}$ layer below the quantum region — are n^+ doped, with a dopant concentration of 5×10^{18} cm^{-3}. The four ohmic contacts are located at the discontinuity between the Si$_{0.7}$Ge$_{0.3}$ and the Al$_2$O$_3$.

2) SiMOS HETEROSTRUCTURE

The description follows Figure 9b and Figure 10b. The heterostructure begins with a 40 nm Si layer,[5] followed by the 10 nm isotopically purified ^{28}Si quantum layer. The latter is separated from the top Al$_2$O$_3$ oxide by a 10 nm SiO$_2$ layer. The device utilises a three-layer metal gate stack: Y-gates, plunger gates and barrier gates, as reported in Figure 10b. Each metal layer is separated from the below metal layer by a 7 nm oxide layer. The height of Y gates is 20 nm, whereas their width is 106 nm. Above the quantum region, the extension of dot plunger and barrier gates is: 33 nm along $\hat{x}$, 33 nm along $\hat{y}$ and 30 nm along $\hat{z}$. The reservoir plunger gates have a 66 nm extension along $\hat{x}$. Along the $\hat{x}$ axis, the plunger and barrier gates are mutually separated by a 7 nm

---

[3]This layer is not included in simulations with QTCAD, since, at the time of writing, the latter is not able to automatically compute the strain from the definition of materials and geometry: one has to manually provide in the input the strain tensor. Therefore, simulating this bottom layer with QTCAD would not be convenient from a computational perspective. Accordingly, this layer is not reported in Figure 9.

[4]As reported in [74], in the experimental structure, this layer is 300 nm thick. Here, it is reduced to a 30 nm layer to relax the memory requirements of the simulation.

[5]As done for the SiGe heterostructure, the 100 nm layer of the experimental device is here reduced to a 40 nm layer for computational efficiency.
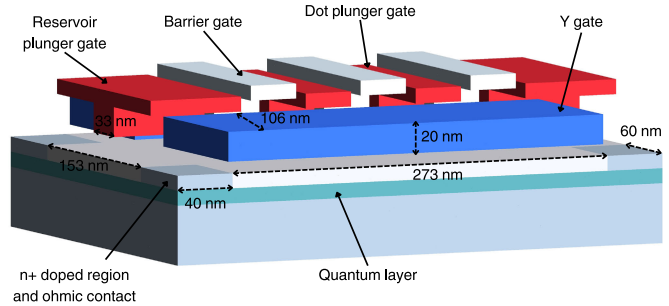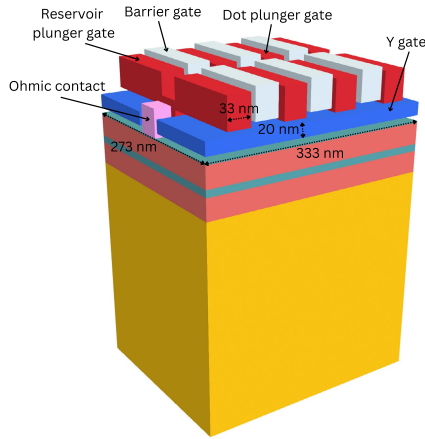
(a) SiGe-^{28}Si-SiGe heterostructure in NextNano.

(b) Si-^{28}Si-SiO$_2$ heterostructure.

FIGURE 10. Graphical representation of the SiGe and SiMOS heterostructures adopted in NextNano [17] and QTCAD [16] simulations, removing the upper oxide layer to highlight the three layers of gates. The metal gate layers, the ohmic contacts and the n^+ doped regions of the SiGe heterostructure in QTCAD follow exactly the same arrangement of the SiMOS one.

Al$_2$O$_3$ layer. Along the $\hat{y}$ axis, Y gates are separated from other gates by a 7 nm Al$_2$O$_3$ layer. At the four corners of the structure, four $40 \times 60 \times 25$nm volumes — including a top Si layer (which replaces the SiO$_2$ in these areas), the ^{28}Si quantum layer and a 5 nm thick Si layer below the quantum region — are n^+ doped, with a dopant concentration of 5×10^{18} cm^{-3}. The four ohmic contacts are located at the discontinuity between the Si and the Al$_2$O$_3$.

B. SiGe HETEROSTRUCTURE: SIMULATION WITH NEXTNANO

This section presents the setup and the results from a Poisson-Schrödinger simulation of the SiGe structure with NextNano.

1) SIMULATION SETUP

The temperature is fixed to $T = 10$ mK and the dopant concentration to $N_D = 1 \times 10^{20}$ cm^{-3} (complete ionization is assumed). The metal workfunction Φ_m is set to 5.12 eV, the reported value of the Pd workfunction in vacuum [80].

a: MESH

A static mesh obtained with the NextNano mesh generator is adopted. The mesh element size ranges from 7.5 nm in the bottom SiGe layer, to 3 nm above and below the quantum layer and to 0.15 nm in the silicon quantum layer. In the upper three-layer metal gate stack, it is set to 3 nm.

b: APPLIED VOLTAGES

The applied voltages — which act as Dirichlet boundary conditions for the FEM solver — are:

$$V_{Y1} = 1.1 \text{ V},$$
$$V_{Y2} = 1.1 \text{ V},$$
$$V_{RL} = 1 \text{ V},$$
$$V_{RR} = 1 \text{ V},$$
$$V_{PL} = 1.5 \text{ V},$$

$$V_{PR} = 1.5 \text{ V},$$
$$V_{BL} = 500 \text{ mV},$$
$$V_{BM} = 770 \text{ mV},$$
$$V_{BR} = 500 \text{ mV}, \quad (41)$$

where V_{Yi} is the voltage applied to the i Y gate, V_{Ri} is the voltage applied to the i reservoir gate, V_{Pi} is the voltage applied to the i plunger gate, V_{Bi} is the voltage applied to the i barrier gate, R means right, L left and M inter-dot. Due to meshing asymmetries along the dots direction, the plunger voltages have been slightly modified during simulations in order to obtain a symmetrically distributed wavefunction. The procedure used to achieve this is the following:

- Execute a preliminary simulation with $V_{PL} = V_{PR}$ to understand under which plunger gate the wavefunction is localized, e.g. PL;
- Increase the voltage value of the other plunger gate (PR) until the wavefunction is localized under it;
- Sweep the voltage of PR between these two values until the wavefunction is symmetrically distributed under the two plunger gates.

This is the reason why the potential profile looks mildly asymmetric in NextNano simulations.

c: STRAIN INDUCED CONDUCTION BAND SPLITTING

Bulk silicon has a six-fold degenerate conduction band minimum along Δ [42], [54]. The six equivalent minima are known as valleys. However, in the SiGe heterostructure, the Si layer is sandwiched between two Si$_{0.7}$Ge$_{0.3}$ layers. The difference in the lattice constants leads to a large in-plane strain that lifts the energies of the $\pm x$ and $\pm y$ valleys (four-fold degenerate level) with respect to the $\pm z$ valleys (two-fold degenerate level). The remaining two-fold degener-
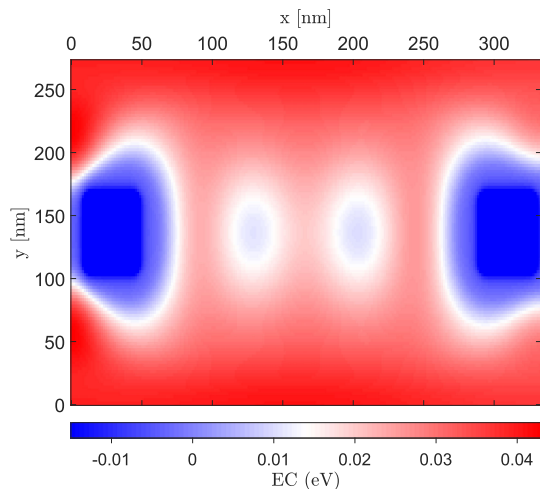
(a) Conduction band profile in a xy-plane at $z = 336$ nm.
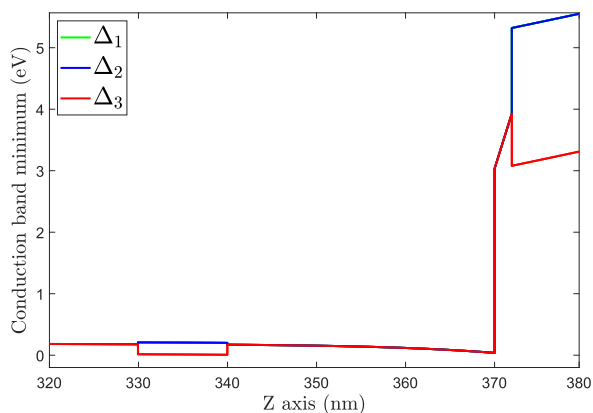
(c) A cut along the $\hat{x}$ axis through the dots at $z = 336$ nm.

(b) A cut along the $\hat{z}$ axis through one dot.
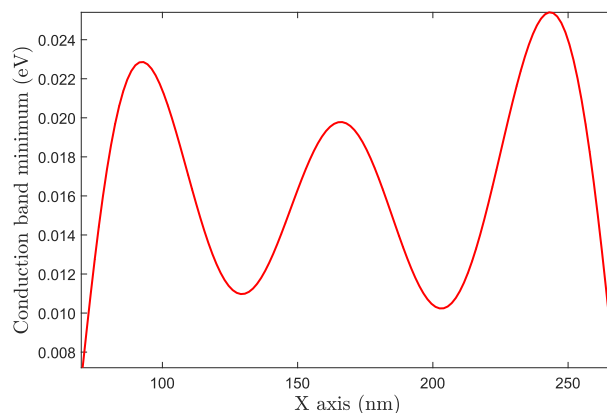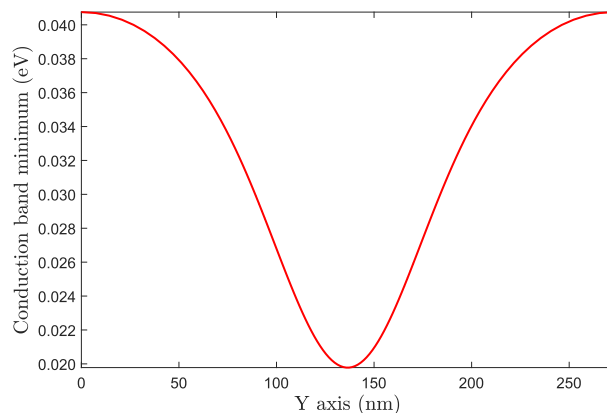
(d) A cut along the $\hat{y}$ axis through one dot at $z = 336$ nm.

FIGURE 11. SiGe heterostructure: conduction band minimum from Poisson simulation obtained with NextNano [17] at 10 mK.

acy of the $\pm z$ valleys is removed[6] by the sharp potential step in the $\hat{z}$ direction [42]. Accordingly, the band alignment in the heterostructure differs from bulk materials [81]. Indeed, the minimum in the conduction band in the ^{28}Si quantum layer is expected to lie approximately 160 meV below the minimum of the conduction band in Si$_{0.7}$Ge$_{0.3}$ layers [42]. The strain computation gives as a result that the minimum in the conduction band in the ^{28}Si quantum layer lies 161 meV below the minimum of the conduction band in Si$_{0.7}$Ge$_{0.3}$ layers.

d: ERRORS
The maximum absolute error for the Poisson solver is set to 5×10^{-7}, that for the Schrödinger solver to 1×10^{-7}.

2) POISSON SIMULATION
a: CONDUCTION BAND MINIMUM
The minimum of the conduction band in a xy-plane with $z = 336$ nm — hence located inside the quantum layer — is reported in Figure 11a, with shrunk scale to highlight

the relevant features. On the sides, the dark blue regions correspond to the n^+ doped areas. At the centre of the figure, the light blue regions indicate the 2D confinement produced by the plunger, barrier and Y gates, which generates two circular wells. The behaviour of the confinement potential (minimum of the conduction band) along the $\hat{z}$ axis for $x = 126.5$ nm and $y = 136.5$ nm — i.e., through the left dot — is outlined in Figure 11b, where the $\pm x$ and $\pm y$ valleys (Δ_1 and Δ_2) and the $\pm z$ valleys (Δ_3) are plotted. One can clearly identify the effect of the NextNano strain computation that splits the Δ_1 and Δ_2 minima (completely superimposed and thus indistinguishable in the plot) from the Δ_3 minimum, creating the 161 meV conduction band discontinuity in correspondence of the ^{28}Si quantum layer. Figure 11c represents the behaviour of the confinement potential along the $\hat{x}$ axis through the two potential valleys at $y = 136.5$ nm and $z = 336$ nm. The height of the inter-dot barrier — computed as the difference from the maximum inter-dot confinement potential and the minima in correspondence of the two valleys — is

$$E_{BM} \sim 8.8 \text{ meV}. \tag{42}$$

[6]Unfortunately, at the time of writing, NextNano does not take into account the $\pm z$ valleys splitting.
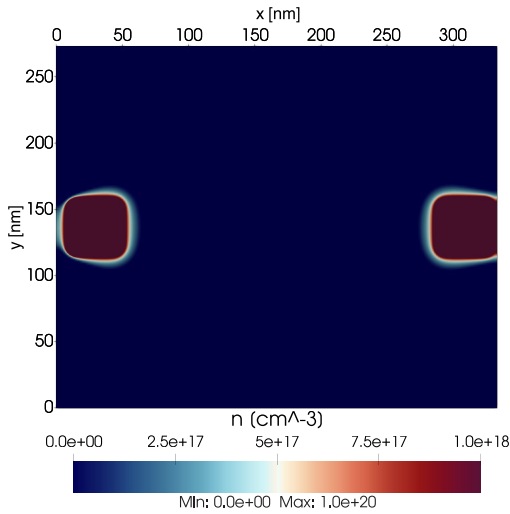
(a) Classical electron population in a xy-plane in the quantum layer ($z = 336\,\mathrm{nm}$) of the SiGe heterostructure.

(b) Tunnel coupling dependence on the inter-dot barrier.

FIGURE 12. Classical electron population and $E_1 - E_0$ splitting in dependence of the inter-dot barrier gate voltage for the SiGe heterostructure, obtained with NextNano [17] at 10 mK.
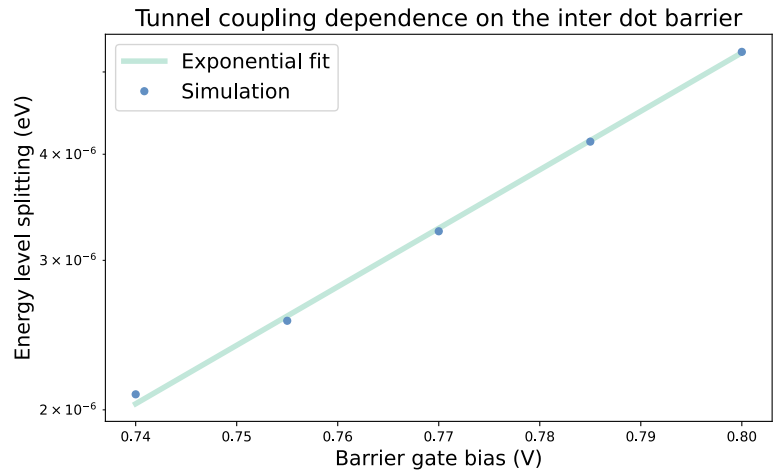
The behaviour of the confinement potential along the $\hat{y}$ axis for $x = 136.5\,\mathrm{nm}$ and $z = 336\,\mathrm{nm}$ — i.e., through the left dot — is outlined in Figure 11d.

b: CLASSICAL ELECTRON POPULATION

Figure 12a reports the classical electron population in a xy-plane inside the quantum layer at $z = 336\,\mathrm{nm}$, with shrunk scale to highlight the relevant features. At the sides, the dark red regions correspond to the n^+ doped areas and represent the reservoirs of classical electrons.

3) SCHRÖDINGER SIMULATION

The Schrödinger equation is solved in the quantum region, which extends:

- Along the $\hat{x}$ axis, from $x = 70\,\mathrm{nm}$ to $x = 263\,\mathrm{nm}$;
- Along the $\hat{y}$ axis, from $y = 89.5\,\mathrm{nm}$ to $y = 183.5\,\mathrm{nm}$;
- Along the $\hat{z}$ axis, from $z = 325\,\mathrm{nm}$ to $z = 370\,\mathrm{nm}$, thus including the SiGe above the $^{28}\mathrm{Si}$ layer.

The quantum region partially includes the confining barriers along the three Cartesian axes to provide proper boundaries to the Schrödinger equation.

a: BOUND STATES

The solution of the Schrödinger equation allows the determination of the single-particle eigenspectra. Figure 13 reports the behaviour of the real part of the eigenfunctions corresponding to the first two energy levels in a xz- and in a xy-planes. One can note that, as expected from the physical geometry, the single-particle wavefunctions are

TABLE 1. Eigenenergies of the first five eigenstates of the SiGe heterostructure obtained with NextNano [17] at 10 mK.

Energy Level	Energy
0	18.186 96 meV
1	18.190 21 meV
2	21.176 80 meV
3	21.221 51 meV
4	21.383 63 meV

equally distributed in the two dots.[7] Moreover, the barriers effectively force the electron to be localised in the two dots since the probability of finding it outside them is negligible. The eigenenergies of the first five eigenstates are reported in Table 1.

b: TUNNEL COUPLING

As reported in Equation (40), the tunnel coupling approximately depends on the difference between the single-particle first excited state and ground state. With the simulation setup outlined in Section IV-B1 and considering Table 1:

$$t_0 \sim \frac{E_1 - E_0}{2} \sim 1.625\,\mathrm{\mu eV} \longrightarrow 392.92\,\mathrm{MHz}. \qquad (43)$$

The $E_1 - E_0$ splitting, in turn, traces back to the inter-dot barrier:

---

[7] An ideal structure would be perfectly symmetric with respect to the inter-dot barrier gate, and thus the potential profile would be symmetric, allowing for an equally distributed wavefunction in the two dots. However, as discussed in Section IV-B1, both experimental devices and simulation models are not exactly symmetric, and some voltage tuning is required to compensate for the asymmetries. For what concerns simulation models, the mesh introduces some asymmetries that lead to a non-symmetric potential profile and a localisation of the electron exclusively in one of the dots. A small offset voltage applied to one of the plunger gates can compensate for this asymmetric behaviour. It was found that increasing the voltage applied to the right plunger gate of 15.4085 meV totally compensates for the issue.
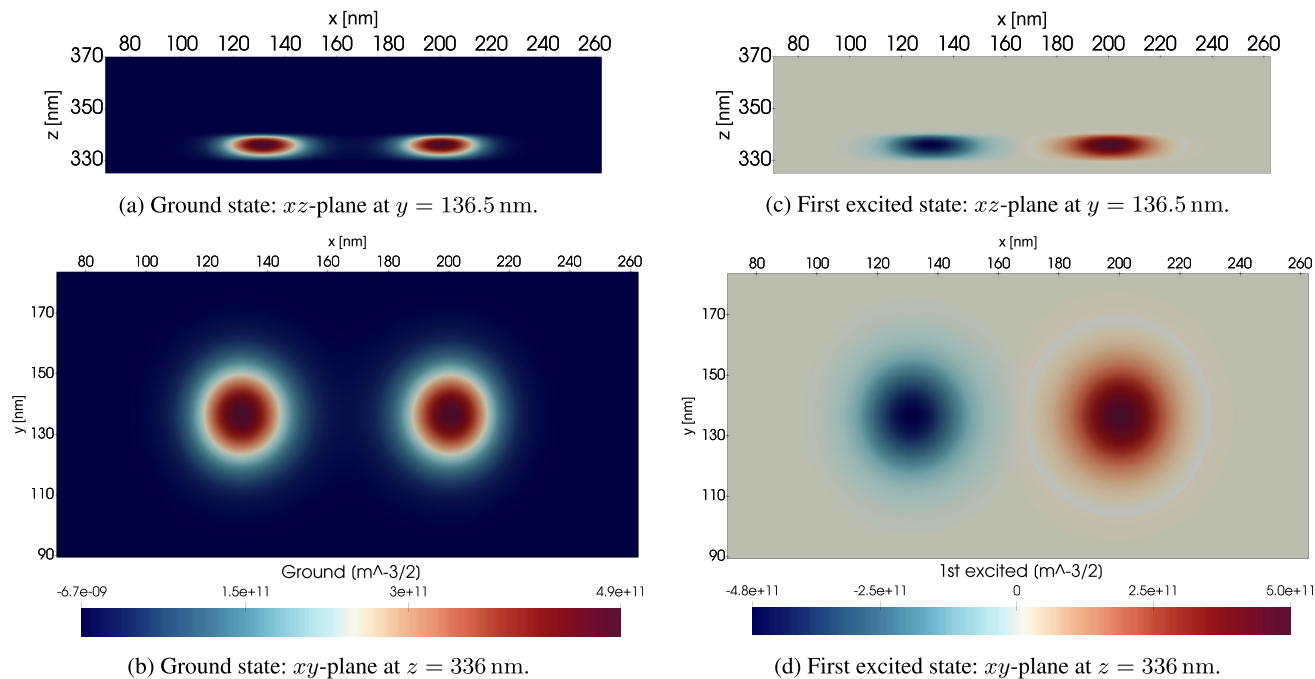
(a) Ground state: xz-plane at $y = 136.5\,\mathrm{nm}$.

(c) First excited state: xz-plane at $y = 136.5\,\mathrm{nm}$.

(b) Ground state: xy-plane at $z = 336\,\mathrm{nm}$.

(d) First excited state: xy-plane at $z = 336\,\mathrm{nm}$.

FIGURE 13. **SiGe heterostructure: bonding ground and anti-bonding first excited state eigenfunctions obtained with NextNano [17] at 10 mK.**

- A high inter-dot barrier means that the two dots are almost independent and consequently $E_0 \sim E_1$.
- A low inter-dot barrier leads to strongly interacting dots and consequently $E_0 < E_1$.

Indeed, the tunnel coupling t_0 is known to show approximately an exponential dependence on the $E_1 - E_0$ splitting and the inter-dot distance [54], [64], [82]. Figure 12b reports the energy level splitting in dependence of the voltage applied to the inter-dot barrier gate when all other gates assume the values of Equation (41): it can be ascertained that, as expected from the above description, the simulation results follow the exponential fit

$$2\,t_0 \sim e^{15.87 \cdot V_{BM}} \cdot 16.19\,\mathrm{peV} \longrightarrow$$

$$V_{BM} \sim \frac{\log_e\left(\frac{2t_0}{1\,\mathrm{eV}}\right) + 24.85}{15.87}\,\mathrm{V}. \qquad (44)$$

C. SiGe HETEROSTRUCTURE: SIMULATION WITH QTCAD

This section presents the setup and the results from a self-consistent Poisson-Schrödinger simulation of the SiGe heterostructure with QTCAD.

1) SIMULATION SETUP

The temperature is fixed to $T = 15\,\mathrm{mK}$ and the dopant concentration to $N_D = 5 \times 10^{18}\,\mathrm{cm}^{-3}$ (complete ionization is assumed). The metal workfunction Φ_m is assumed to be

$$\Phi_m = \chi_{\mathrm{Si}_{0.7}\mathrm{Ge}_{0.3}} + \frac{E_{g-\mathrm{Si}_{0.7}\mathrm{Ge}_{0.3}}}{2}, \qquad (45)$$

where $\chi_{\mathrm{Si}_{0.7}\mathrm{Ge}_{0.3}}$ and $E_{g-\mathrm{Si}_{0.7}\mathrm{Ge}_{0.3}}$ are respectively the affinity and the band gap of $\mathrm{Si}_{0.7}\mathrm{Ge}_{0.3}$.

a: MESH

A static mesh obtained with GMSH [65] is adopted. The mesh element size ranges from 4 nm in the bottom SiGe layer, to 2 nm above and below the quantum layer and to 1 nm in the silicon quantum layer. In the upper three-layer metal gate stack, it ranges from 2 nm to 4 nm.

b: APPLIED VOLTAGES

The applied voltages — which act as Dirichlet boundary conditions for the FEM solver — are:

$$
\begin{aligned}
V_{Y1} &= 290\,\mathrm{mV}, \\
V_{Y2} &= 290\,\mathrm{mV}, \\
V_{RL} &= 600\,\mathrm{mV}, \\
V_{RR} &= 600\,\mathrm{mV}, \\
V_{PL} &= 780\,\mathrm{mV}, \\
V_{PR} &= 780\,\mathrm{mV}, \\
V_{BL} &= -200\,\mathrm{mV}, \\
V_{BM} &= -150\,\mathrm{mV}, \\
V_{BR} &= -200\,\mathrm{mV}, \qquad (46)
\end{aligned}
$$

where V_{Yi} is the voltage applied to the i Y gate, V_{Ri} is the voltage applied to the i reservoir gate, V_{Pi} is the voltage applied to the i plunger gate, V_{Bi} is the voltage applied to the i barrier gate, R means right, L left and M inter-dot.

c: STRAIN INDUCED CONDUCTION BAND SPLITTING

At the time of writing, QTCAD cannot automatically determine the strain from the materials and the geometry. Therefore, the strain computation is carried out with
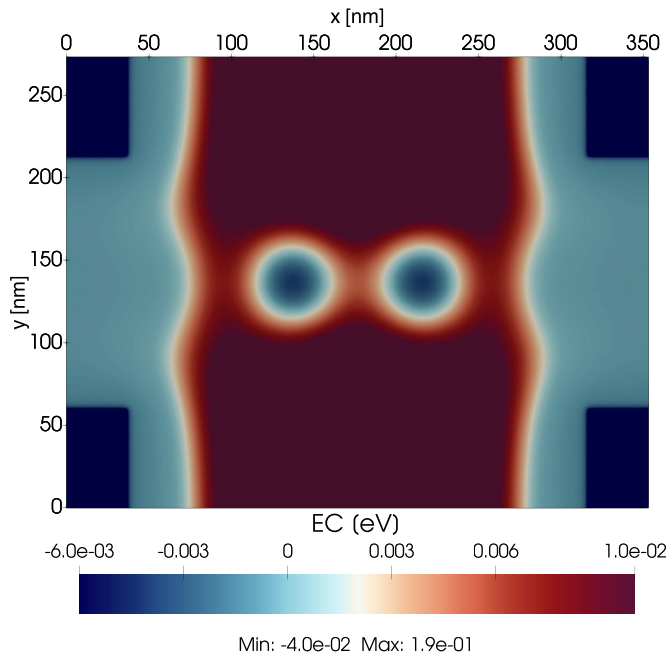
(a) Conduction band profile in a xy-plane in the quantum layer ($z = 36$ nm).
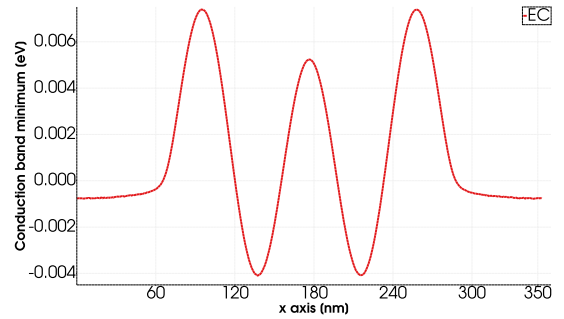
(b) A cut along the $\hat{x}$ axis through the dots at $z = 36$ nm.
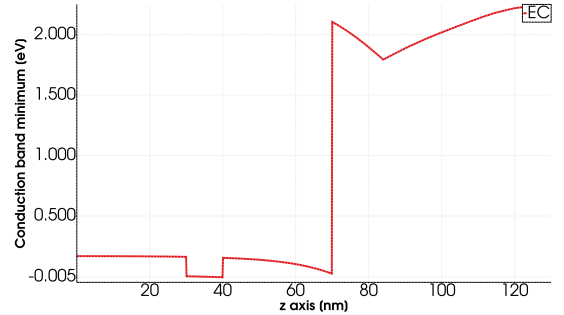
(c) A cut along the $\hat{z}$ axis through one dot.

FIGURE 14. SiGe heterostructure: conduction band minimum from Poisson simulation obtained with QTCAD [16] at 15 mK.

NextNano in Section IV-B1. The alignment between the minimum in the conduction band in the ^{28}Si quantum layer and the minimum of the conduction band in $Si_{0.7}Ge_{0.3}$ can be reproduced in QTCAD by adding a fictitious potential $V_{st} = -146$ mV to the Si quantum layer.

d: ERRORS
The maximum absolute error for the Poisson solver is set to 1×10^{-7}, that for the Schrödinger solver to 1×10^{-9} and that for the self-consistent Poisson-Schrödinger solver to 1×10^{-5}.

2) POISSON SIMULATION
a: CONDUCTION BAND MINIMUM
The minimum of the conduction band in a xy-plane with $z = 36$ nm — hence located inside the quantum layer — is reported in Figure 14a, with shrunk scale to highlight the relevant features. At the four corners, the dark blue regions correspond to the n^+ doped areas. At the centre of the figure, one can clearly identify the 2D confinement — induced by the plunger, barrier and Y gates — that creates a couple of circularly shaped local wells. Figure 14b represents the behaviour of the confinement potential (minimum of the conduction band) along the $\hat{x}$ axis through the two potential valleys at $y = 136.5$ nm and $z = 36$ nm. The height of the inter-dot barrier — computed as the difference from the maximum inter-dot confinement potential and the minima in correspondence of the two valleys — is

$$E_{BM} \sim 9.33 \text{ meV}. \tag{47}$$

The behaviour of the confinement potential along the $\hat{z}$ axis for $x = 136$ nm and $y = 136.5$ nm — i.e., through the left dot — is outlined in Figure 14c, where one can identify the 161 meV conduction band discontinuity in correspondence of the ^{28}Si quantum layer.

b: CLASSICAL ELECTRON POPULATION
Figure 15a reports the classical electron population in a xy-plane inside the quantum layer at $z = 36$ nm, with shrunk scale to highlight the relevant features. At the four corners, the dark red regions correspond to the n^+ doped areas. The light blue areas, which in the central region along the $\hat{x}$ axis reach the external dot barriers, represent the reservoirs of classical electrons.

3) SCHRÖDINGER SIMULATION
The Schrödinger equation is solved in the quantum region, which extends:
- Along the $\hat{x}$ axis, from $x = 93.5$ nm to $x = 259.5$ nm;
- Along the $\hat{y}$ axis, from $y = 60$ nm to $y = 213$ nm;
- Along the $\hat{z}$ axis, from $z = 25$ nm to $z = 45$ nm, thus including 5 nm of SiGe below and above the ^{28}Si layer.

The quantum region partially includes the confining barriers along the three Cartesian axes to provide proper boundaries to the Schrödinger equation.

a: BOUND STATES
Figure 16 reports the behaviour of the real part of the eigenfunctions corresponding to the first two energy levels in a xz and in a xy planes. Once more, the single-particle
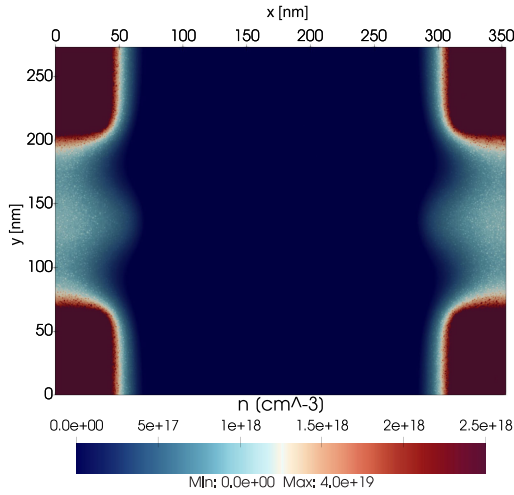
(a) Classical electron population in a xy-plane in the quantum layer ($z = 36\,\text{nm}$) of the SiGe heterostructure.

(b) Tunnel coupling dependence on the inter-dot barrier.

FIGURE 15. Classical electron population and $E_1 - E_0$ splitting in dependence of the inter-dot barrier gate voltage for the SiGe heterostructure, obtained with QTCAD [16] at 15 mK.

TABLE 2. Eigenenergies of the first five eigenstates of the SiGe heterostructure obtained with QTCAD [16] at 15 mK.

Energy Level	Energy
0	3.270 88 meV
1	3.271 49 meV
2	6.288 17 meV
3	6.308 17 meV
4	6.480 04 meV

wavefunctions are equally distributed in the two dots.[8] The eigenenergies of the first five eigenstates are reported in Table 2.

b: LEVER ARM

The lever arm α_G is a unitless coefficient that determines the extent to which a gate G is able to tune the chemical potentials of a quantum dot

$$\mu = \mu_0 - e\alpha_G V_G, \qquad (48)$$

where μ is the chemical potential of the dot [43], μ_0 is the chemical potential of the dot when $V_G = 0$ and e is the elementary charge. Within the constant interaction model, the lever arm can be shown to be [83]

$$\alpha_G = -\frac{C_G}{C_\Sigma}, \qquad (49)$$

where C_G is the capacitance between the dot and gate G, $C_\Sigma = -\sum_i C_i$ and C_i is the capacitance between the dot and the i-th gate. However, the lever arm can also be computed by performing a linear fit of the response of the electronic structure of the quantum dot upon gate bias changes [84]. More in detail, one fixes the potential on all gates but gate G and solves the Poisson-Schrödinger equation for a range of voltages

---

[8] In this case, it was found that increasing the voltage applied to the right plunger gate of 329.96 μeV totally compensates for the mesh-induced asymmetries.
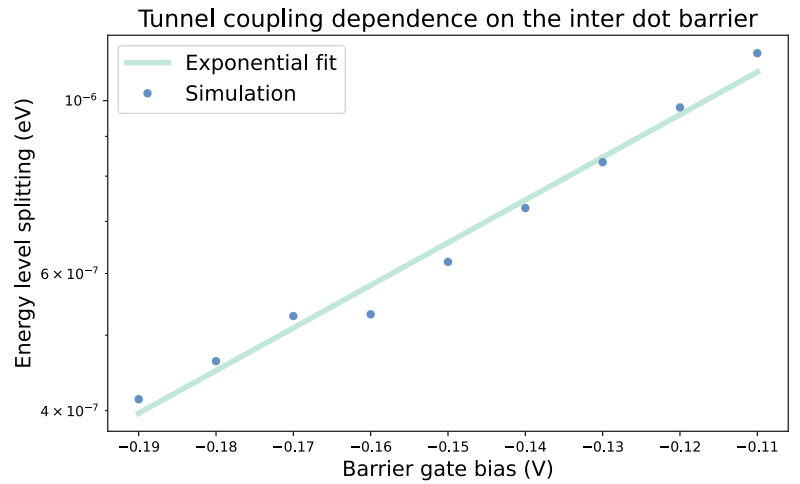
TABLE 3. Lever arm matrix considering the first five eigenstates and the left plunger gate, the inter-dot barrier gate and the right plunger gate of the SiGe heterostructure obtained with QTCAD [16] at 15 mK. The voltage increment used to estimate the lever arm matrix is 100 μV.

Eigenstate	α_{PL}	α_{BM}	α_{PR}
0	7.764×10^{-2}	2.440×10^{-2}	7.764×10^{-2}
1	2.089×10^{-2}	2.439×10^{-2}	2.077×10^{-2}
2	4.738×10^{-2}	2.529×10^{-2}	4.813×10^{-2}
3	7.455×10^{-2}	2.311×10^{-2}	1.579×10^{-2}
4	1.840×10^{-2}	2.311×10^{-2}	7.705×10^{-2}

V_G. Finally, one carries out a linear fit of the ground state energy with respect to gate bias: the obtained slope is $-e\alpha_G$. This procedure is automatically handled by QTCAD [85], which can compute a lever arm matrix (reported in Table 3), repeating the procedure mentioned above for all gates of interest and for all energy levels of interest.
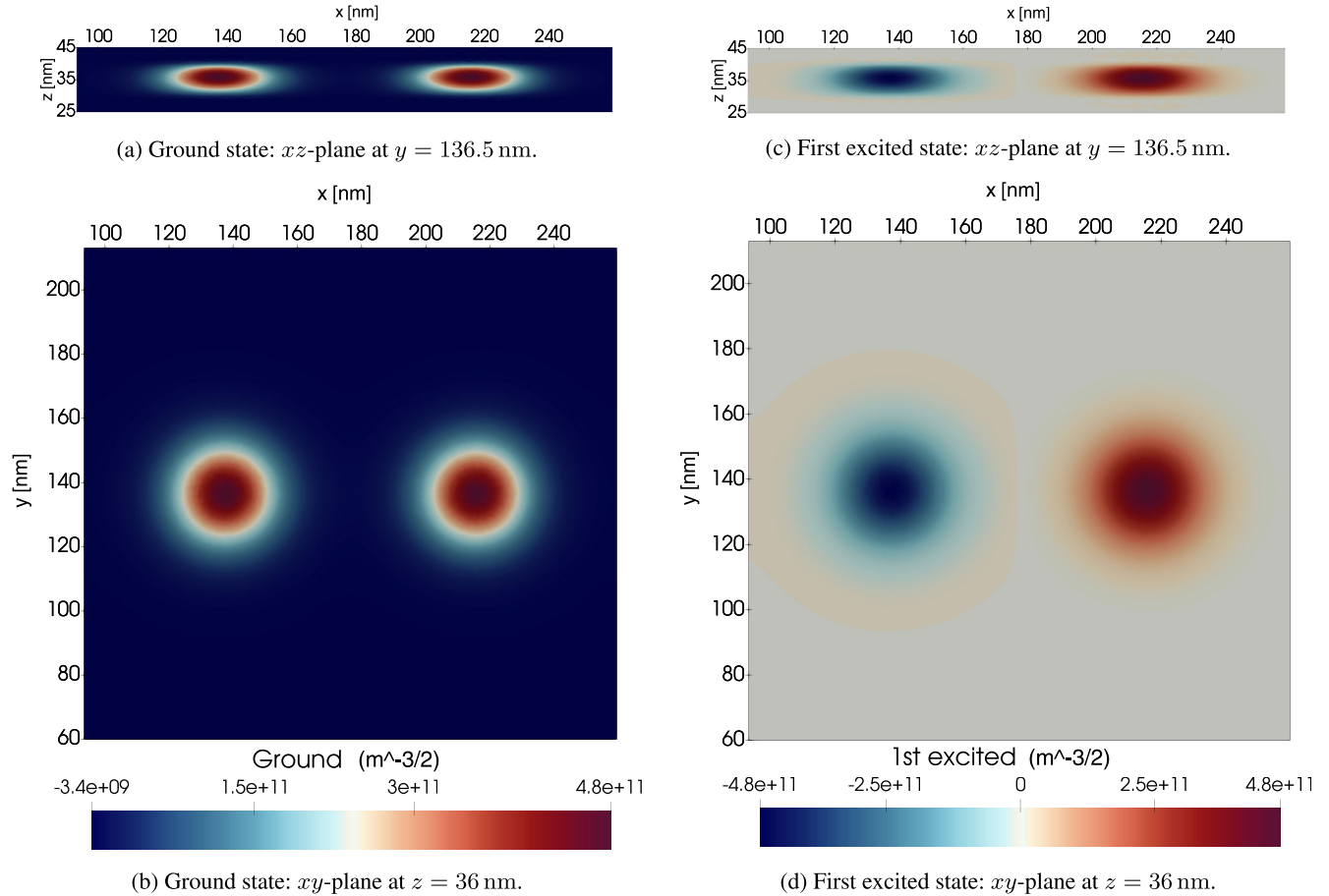
c: TUNNEL COUPLING

With the simulation setup outlined in Section IV-C1 and considering Table 2:

$$t_0 \sim \frac{E_1 - E_0}{2} \sim 305\,\text{neV} \longrightarrow 73.75\,\text{MHz}. \qquad (50)$$

Figure 15b reports the energy level splitting in dependence of the voltage applied to the inter-dot barrier gate when all other gates assume the values of Equation (46): it can be ascertained that the simulation results follow the exponential fit

$$2\,t_0 \sim e^{12.61 \cdot V_{BM}} \cdot 4.36\,\mu\text{eV} \longrightarrow$$

$$V_{BM} \sim \frac{\log_e(\frac{2t_0}{1\,\text{eV}}) + 12.34}{12.61}\text{V}. \qquad (51)$$

To get this physically plausible behaviour, one has to compensate for the small mesh-induced asymmetries, with a similar approach to the one outlined for the determination of bound states.

(a) Ground state: xz-plane at $y = 136.5\,\mathrm{nm}$.

(c) First excited state: xz-plane at $y = 136.5\,\mathrm{nm}$.

(b) Ground state: xy-plane at $z = 36\,\mathrm{nm}$.

(d) First excited state: xy-plane at $z = 36\,\mathrm{nm}$.

FIGURE 16. SiGe heterostructure: bonding ground and anti-bonding first excited state eigenfunctions obtained with QTCAD [16] at 15 mK.

D. SiMOS HETEROSTRUCTURE: SIMULATION WITH QTCAD

This section presents the setup and the results from a self-consistent Poisson-Schrödinger simulation of the SiMOS heterostructure with QTCAD.

1) SIMULATION SETUP

The temperature is fixed to $T = 15\,\mathrm{mK}$ and the dopant concentration to $N_D = 5 \times 10^{18}\,\mathrm{cm}^{-3}$ (complete ionization is assumed). The metal workfunction Φ_m is assumed to be

$$\Phi_m = \chi_{\mathrm{Si}} + \frac{E_{g-\mathrm{Si}}}{2}, \qquad (52)$$

where χ_{Si} and $E_{g-\mathrm{Si}}$ are respectively the affinity and the band gap of Si.

a: MESH

A static mesh obtained with GMSH [65] is adopted. The mesh element size ranges from 8 nm in the bottom Si layer, to 2 nm above and below the quantum layer and to 1 nm in the silicon quantum layer. In the upper three-layer metal gate stack, it ranges from 2 nm to 8 nm.

b: APPLIED VOLTAGES

The applied voltages — which act as Dirichlet boundary conditions for the FEM solver — are:

$$\begin{aligned}
V_{Y1} &= 535\,\mathrm{mV}, \\
V_{Y2} &= 535\,\mathrm{mV}, \\
V_{RL} &= 1.3\,\mathrm{V}, \\
V_{RR} &= 1.3\,\mathrm{V}, \\
V_{PL} &= 700\,\mathrm{mV}, \\
V_{PR} &= 700\,\mathrm{mV}, \\
V_{BL} &= 40\,\mathrm{mV}, \\
V_{BM} &= 400\,\mathrm{mV}, \\
V_{BR} &= 40\,\mathrm{mV}, \qquad (53)
\end{aligned}$$

where V_{Yi} is the voltage applied to the i Y gate, V_{Ri} is the voltage applied to the i reservoir gate, V_{Pi} is the voltage applied to the i plunger gate, V_{Bi} is the voltage applied to the i barrier gate, R means right, L left and M inter-dot.

c: ERRORS

The maximum absolute error for the Poisson solver is set to 1×10^{-7}, that for the Schrödinger solver to 1×10^{-9} and that for the self-consistent Poisson-Schrödinger solver to 1×10^{-5}.
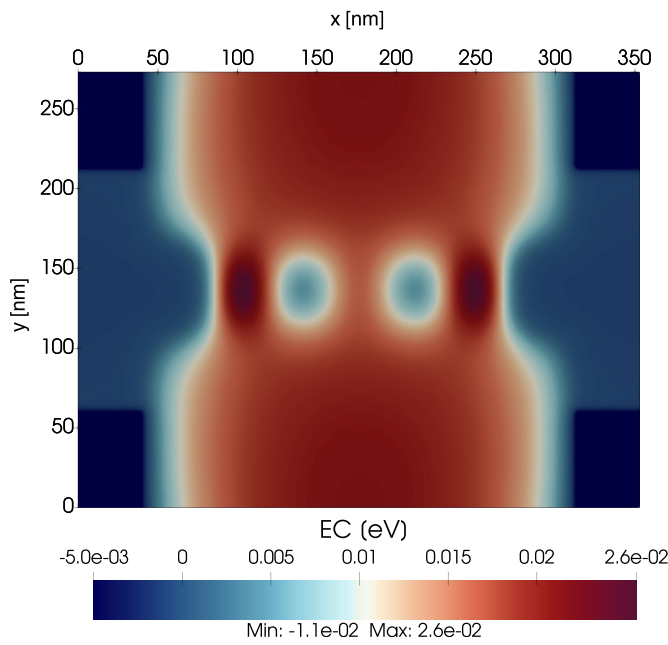
(a) Conduction band profile in a xy-plane in the quantum layer ($z = 45\,\text{nm}$).
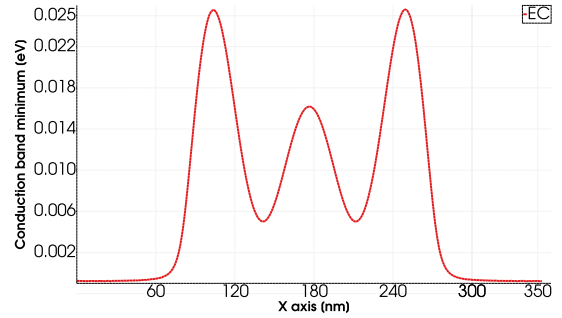
(b) A cut along the $\hat{x}$ axis through the dots at $z = 45\,\text{nm}$.
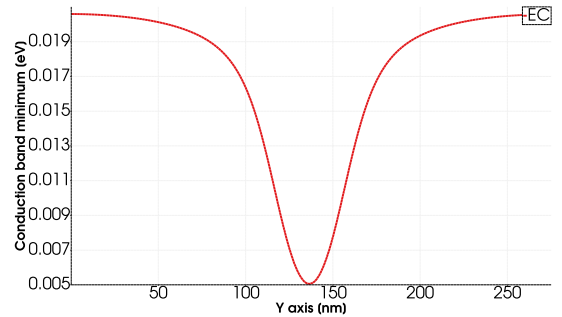
(c) A cut along the $\hat{y}$ axis through one dot at $z = 45\,\text{nm}$.

FIGURE 17. SiMOS heterostructure: conduction band minimum from Poisson simulation obtained with QTCAD [16] at 15 mK.

2) POISSON SIMULATION

a: CONDUCTION BAND MINIMUM

The minimum of the conduction band in a xy-plane with $z = 45\,\text{nm}$ — hence located inside the quantum layer — is reported in Figure 17a, with shrunk scale to highlight the relevant features. Similarly to the SiGe case, the dark blue regions at the four corners correspond to the n^+ doped areas. At the centre of the figure, the 2D confinement — induced by the plunger, barrier and Y gates — creates a couple of circularly shaped local wells. Figure 17b represents the behaviour of the confinement potential (minimum of the conduction band) along the $\hat{x}$ axis through the two valleys at $y = 136.5\,\text{nm}$ and $z = 45\,\text{nm}$. The height of the inter-dot barrier — computed again as the difference from the maximum inter-dot confinement potential and the minima in correspondence of the two valleys — is

$$E_{BM} \sim 11.15\,\text{meV}. \tag{54}$$

The behaviour of the confinement potential along the $\hat{y}$ axis for $x = 140\,\text{nm}$ and $z = 45\,\text{nm}$ — i.e., through the left dot — is outlined in Figure 17c.

b: CLASSICAL ELECTRON POPULATION

Figure 18a reports the classical electron population in a xy-plane inside the quantum layer at $z = 45\,\text{nm}$, with shrunk scale to highlight the relevant features. Also for this structure, one can see the n^+ doped areas and the reservoirs of classical electrons, which in the central region along the $\hat{x}$ axis reach the external dot barriers.

TABLE 4. Eigenenergies of the first five eigenstates of the SiMOS heterostructure obtained with QTCAD [16] at 15 mK.

Energy Level	Energy
0	11.294 78 meV
1	11.297 73 meV
2	14.079 99 meV
3	14.089 14 meV
4	14.489 30 meV

3) SCHRÖDINGER SIMULATION

The Schrödinger equation is solved in the quantum region, which extends:

- Along the $\hat{x}$ axis, from $x = 96.5\,\text{nm}$ to $x = 256.5\,\text{nm}$;
- Along the $\hat{y}$ axis, from $y = 60\,\text{nm}$ to $y = 213\,\text{nm}$;
- Along the $\hat{z}$ axis, from $z = 35\,\text{nm}$ to $z = 55\,\text{nm}$, thus including 5 nm of Si below ^{28}Si layer and 5 nm of SiO$_2$ above the ^{28}Si layer.

As for the SiGe heterostructure, the quantum region partially includes the confining barriers along the three Cartesian axes to provide proper boundaries to the Schrödinger equation.

a: BOUND STATES

Figure 19 reports the behaviour of the real part of the eigenfunctions corresponding to the first two energy levels in a xz and in a xy planes. The single-particle wavefunctions are again equally distributed in the two strongly confined dots.[9] The eigenenergies of the first five eigenstates are reported in Table 4.

---

[9]In this case, it was found that increasing the voltage applied to the right plunger gate of 329.96 μeV totally compensates for the mesh-induced asymmetries.
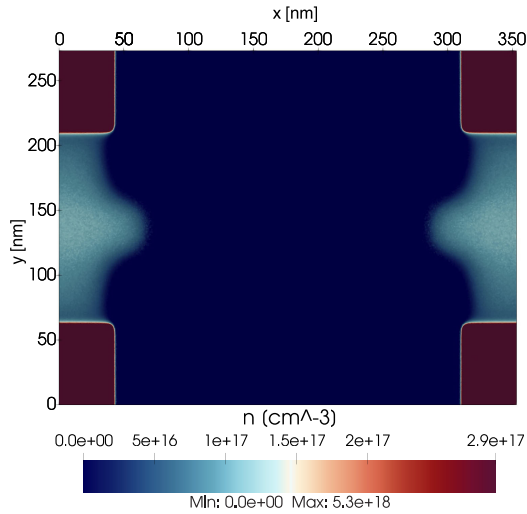
(a) Classical electron population in a xy-plane in the quantum layer ($z = 45\,\mathrm{nm}$) of the SiMOS heterostructure.
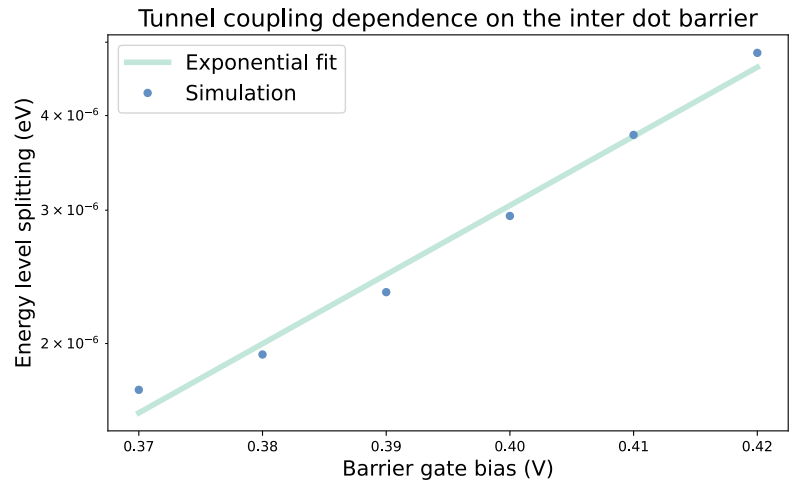
(b) Tunnel coupling dependence on the inter-dot barrier.

FIGURE 18. Classical electron population and $E_1 - E_0$ splitting in dependence of the inter-dot barrier gate voltage for the SiMOS heterostructure, obtained with QTCAD [16] at 15 mK.

TABLE 5. Lever arm matrix considering the first five eigenstates and the left plunger gate, the inter-dot barrier gate and the right plunger gate of the SiMOS heterostructure obtained with QTCAD [16] at 15 mK. The voltage increment used to estimate the lever arm matrix is 5 mV.

Eigenstate	α_{PL}	α_{BM}	α_{PR}
0	1.275×10^{-1}	3.448×10^{-2}	1.276×10^{-1}
1	1.951×10^{-2}	3.440×10^{-2}	1.949×10^{-2}
2	1.069×10^{-1}	3.103×10^{-2}	1.816×10^{-2}
3	1.928×10^{-2}	3.087×10^{-2}	1.081×10^{-1}
4	1.016×10^{-1}	3.911×10^{-2}	1.011×10^{-1}

b: LEVER ARM

Following the procedure outlined in Section IV-C3.b, one can determine the lever arm matrix, which is reported in Table 5.

c: TUNNEL COUPLING

With the simulation setup outlined in Section IV-D1 and considering Table 4, the tunnel coupling is:

$$t_0 \sim \frac{E_1 - E_0}{2} \sim 1.474\,\mathrm{\mu eV} \longrightarrow 356.41\,\mathrm{MHz}. \qquad (55)$$

Figure 18b reports the energy level splitting in dependence of the voltage applied to the inter-dot barrier gate when all other gates assume the values of Equation (53): it can be ascertained that the simulation results follow the exponential fit

$$2\,t_0 \sim e^{21.02 \cdot V_{BM}} \cdot 678.87\,\mathrm{peV} \longrightarrow$$

$$V_{BM} \sim \frac{\log_e(\frac{2t_0}{1\,\mathrm{eV}}) + 21.11}{21.02}\,\mathrm{V}. \qquad (56)$$

As mentioned above, to get this physically plausible behaviour, one has to compensate for the small mesh-induced asymmetries, with a similar approach to the one outlined for the determination of bound states.

V. RESULTS AND DISCUSSION

Whereas Section III-E validates the approximations introduced in the compact model, this section is devoted to the results obtained comparing the proposed model with QuTiP [15] when relevant quantum circuits and algorithms are simulated.

A. SIMULATION SETUP

This section describes the simulation setup adopted to validate the proposed methodology (whose block scheme is reported in Figure 8) and the corresponding assumptions. The same configuration parameters — such as the qubit timescales T_1 and T_2^*, the duration of quantum gates and the quantum circuits to be tested described in OpenQASM language [47] — are provided to the MATLAB simulator, taking into account the discussed models of semiconductor qubits, and to QuTiP [15]. The MATLAB simulator and the direct integration return the **fidelity** and the probability distribution of eigenstates.

1) GENERAL ASSUMPTIONS

Analogously to [20], the model discussed in this article assumes that:
- The initial state is a **pure fiducial initial state**, i.e., $\rho_0 = (|0\rangle\langle 0|)^{\otimes n}$.
- The measurement operation is an ideal projective measurement, i.e., when a measurement call is provided to the simulator, it returns the main diagonal of the density matrix corresponding to the qubits' probability distribution.

2) MODEL STRUCTURE AND INTERFACE

As discussed in Section III-F2, the proposed model for semiconductor-based quantum dots is embedded in the simulation infrastructure presented in [19], [20]. Accordingly:
- The quantum algorithm description is read from a .qasm file written according to OpenQASM description language.
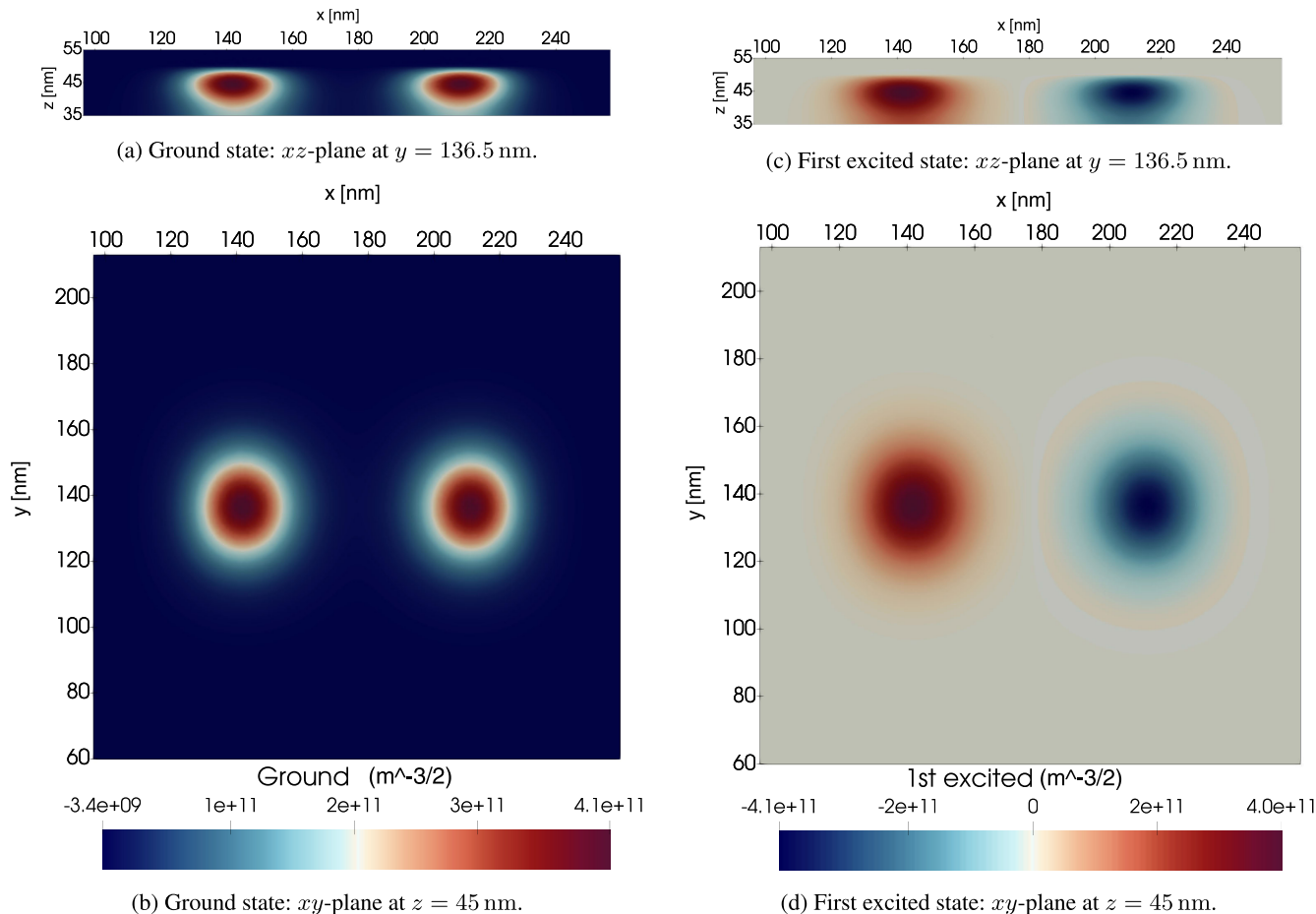
(a) Ground state: xz-plane at $y = 136.5\,\text{nm}$.

(b) Ground state: xy-plane at $z = 45\,\text{nm}$.

(c) First excited state: xz-plane at $y = 136.5\,\text{nm}$.

(d) First excited state: xy-plane at $z = 45\,\text{nm}$.

FIGURE 19. SiMOS heterostructure: bonding ground and anti-bonding first excited state eigenfunctions obtained with QTCAD [16] at 15 mK.

- The system is initialised in its pure ground state, corresponding to a density matrix $\rho_0 = (|0\rangle\langle 0|)^{\otimes n}$, as mentioned above.
- Each quantum gate is applied for a time amount τ_{sq} or τ_{mq}, thus changing both ρ (physical evolution) and $|\psi_{\text{ideal}}\rangle$ (ideal evolution). In the same time interval, the effects of non-ideality phenomena on the density matrix are evaluated.
- After a measurement operation call, the infrastructure provides in the output the ideal outcomes, those obtained resorting to the proposed model and the corresponding fidelities.

3) COMPARISON WITH QUTIP

The model introduced in Section III adopts a **time-independent** Hamiltonian, as discussed at the end of Section III-F2, with the corresponding set of approximations. The off-resonance evolution of not-addressed qubits is taken into account thanks to the so-called Fourier model. To validate the proposed simulation methodology, the obtained results are compared with the outcomes produced by a **direct numerical integration** — performed with QuTiP [15] — of the complete time-dependent rotating-frame Hamiltonian of Equation (14). Two-qubit quantum circuits are used as

benchmarks and the evolution corresponding to each quantum gate is simulated according to both approaches. It has to be remarked that both methods adopt the decoherence model proposed in Section III-F1 and resort to the assumptions of Section V-A1. The comparison between the provided results takes into account:

- The **fidelity**, which is a scalar quantity that determines the distance between two quantum states. According to [51], the fidelity between two mixed states represented by density matrices ρ_a and ρ_b is:

$$\mathcal{F}(\rho_a, \rho_b) \triangleq \text{Tr}\left(\sqrt{\rho_a^{1/2}\,\rho_b\,\rho_a^{1/2}}\right), \qquad (57)$$

where Tr is the matrix trace. If one of the two states is described by a state vector $|\psi\rangle$ and the other by a density matrix ρ, the fidelity can be expressed as

$$\mathcal{F}(|\psi\rangle, \rho) = \sqrt{\langle\psi|\,\rho\,|\psi\rangle}. \qquad (58)$$

It can be shown that $0 \leq \mathcal{F} \leq 1$ and $\mathcal{F} = 1$ when the two states coincide [51]. For every quantum algorithm and for every combination of physical parameters, the fidelity resulting from the MATLAB model $\mathcal{F}_M = \mathcal{F}(|\psi\rangle, \rho_{\text{MATLAB}})$ and that resulting from the QuTiP direct integration $\mathcal{F}_Q = \mathcal{F}(|\psi\rangle, \rho_{\text{QuTiP}})$ are reported.

TABLE 6. Main input and output physical parameters for the different heterostructures and the different software tools. T is the temperature; N_D is the doping concentration; Φ_m is the metal workfunction; V_{Yi} is the voltage applied to the i Y gate; V_{Ri} is the voltage applied to the i reservoir gate; V_{Pi} is the voltage applied to the i plunger gate; V_{Bi} is the voltage applied to the i barrier gate; CB min refers to the minimum of the conduction band in the dot region; $\Delta_2 - \Delta_3$ is the computed strain-induced conduction band splitting along the $\hat{z}$ axis; E_Y is the Y energy barrier computed as the energy difference between the maximum and the minimum of the conduction band in the quantum region along the $\hat{y}$ axis (cf. Figure 11d and Figure 17c); E_{BL} is the left-barrier gate energy barrier computed as the energy difference between the minimum of the conduction band in the quantum region along the $\hat{x}$ axis and the maximum of the conduction band in the quantum region below the left barrier gate (cf. Figure 11c, Figure 14b and Figure 17b); E_{BM} and E_{BR} have similar definitions; E_i is the eigenenergy of the i-th single-particle eigenstate; α_{PL}, α_{BM} and α_{PR} are the lever arms of the left plunger gate, inter-dot barrier gate and right plunger gate to the single-particle ground state; t_0 is the tunnel coupling computed according to Equation (40), ζ and κ are the fitting parameters of $V_{BM} \sim \left\{ \log_e\left(\frac{2t_0}{1\,\text{eV}}\right) + \zeta \right\} / \kappa$; the symbol — means that the corresponding parameter cannot be computed.

	Names		Physical values in the heterostructures		
	Group	Parameter	SiGe – NextNano	SiGe – QTCAD	SiMOS – QTCAD
Inputs	Setup	T	10 mK	15 mK	15 mK
		N_D	$1 \times 10^{20}\,\text{cm}^{-3}$	$5 \times 10^{18}\,\text{cm}^{-3}$	$5 \times 10^{18}\,\text{cm}^{-3}$
		Φ_m	$\sim 5.12\,\text{eV}$	$\sim 4.55\,\text{eV}$	$\sim 4.61\,\text{eV}$
	Applied DC voltages	V_{Y1}	1100 mV	290 mV	535 mV
		V_{Y2}	1100 mV	290 mV	535 mV
		V_{RL}	1000 mV	600 mV	1300 mV
		V_{RR}	1000 mV	600 mV	1300 mV
		V_{PL}	1500 mV	780 mV	700 mV
		V_{PR}	1500 mV	780 mV	700 mV
		V_{BL}	500 mV	-200 mV	40 mV
		V_{BM}	770 mV	-150 mV	400 mV
		V_{BR}	500 mV	-200 mV	40 mV
Outputs	Conduction band	CB min	10 meV	-7 meV	5 meV
		$\Delta_2 - \Delta_3$	161 meV	—	—
		E_Y	21 meV	31 meV	25 meV
		E_{BL}	12 meV	14 meV	30 meV
		E_{BM}	8.80 meV	9.33 meV	11.15 meV
		E_{BR}	15 meV	14 meV	31 meV
	Energy levels	E_0	18.1870 meV	3.2709 meV	11.2948 meV
		E_1	18.1902 meV	3.2715 meV	11.2977 meV
		E_2	21.1768 meV	6.2882 meV	14.0800 meV
		E_3	21.2215 meV	6.3082 meV	14.0891 meV
		E_4	21.3836 meV	6.4800 meV	14.4893 meV
	Lever arms	$\alpha_{PL}(E_0)$	—	7.764×10^{-2}	1.275×10^{-1}
		$\alpha_{BM}(E_0)$	—	2.440×10^{-2}	3.448×10^{-2}
		$\alpha_{PR}(E_0)$	—	7.764×10^{-2}	1.276×10^{-1}
	Tunnel	t_0	1625 neV	305 neV	1474 neV
		ζ	24.85	12.34	21.11
		κ	15.87	12.61	21.02

In the previous expressions, $|\psi\rangle$ denotes the ideal noiseless expected output, whereas ρ represents the noisy output.

- The **most probable eigenstate** determined by the MATLAB model (MPE_M) and that determined by the QuTiP direct integration (MPE_Q).
- The **Kullback-Leibler (KL) divergence** [86], [87], which measures the distance of a target discrete probability distribution P — for instance coming from experimental data — from a reference one Q. Accordingly, if dealing with mixed states, the computation of

the KL divergence requires exclusively the diagonals of the corresponding density matrices. This metric has been already employed in [87] for evaluating the reliability of the execution of a circuit on a superconducting quantum computer and in [20]. For an n-qubit distribution, the KL divergence is defined as

$$\mathcal{D}_{\text{KL}}(P \parallel Q) \triangleq \sum_{i=0}^{N-1} P(|e_i\rangle) \log_2\left(\frac{P(|e_i\rangle)}{Q(|e_i\rangle)}\right), \quad (59)$$

where $N = 2^n$ and $|e_i\rangle_{0 \leq i < N}$ are the orthonormal eigenstates of the $\sigma_z^{\otimes n}$ Pauli spin operator. By construction, $0 \leq \mathcal{D}_{KL}(P \parallel Q) \leq +\infty$, and $\mathcal{D}_{KL}(P \parallel Q) = 0$ if and only if the two probability distributions coincide. Hence, the smaller $\mathcal{D}_{KL}(P \parallel Q)$ is, the closer P and Q are. By identifying:

$$P(|e_i\rangle) = \rho_{\text{MATLAB}}(i, i),$$
$$Q(|e_i\rangle) = \rho_{\text{QuTiP}}(i, i), \qquad (60)$$

$\mathcal{D}_{KL}(P \parallel Q)$ evaluates the similarity between the probability distribution of the eigenstates provided by the MATLAB simulator and the corresponding distribution provided by QuTiP.

- The percentage matrix **2-norm of the difference** between the output density matrices provided by the MATLAB model and the direct integration with QuTiP:

$$\varepsilon_\% = \|\rho_{\text{MATLAB}} - \rho_{\text{QuTiP}}\| \cdot 100. \qquad (61)$$

- The **wall-clock time** t_M^{ck} required to emulate the execution of a quantum algorithm with the MATLAB model and the wall-clock time t_Q^{ck} required to emulate the execution of a quantum algorithm with QuTiP direct integration.

4) PHYSICAL AND CONTROL PARAMETERS

As discussed in Section III-D, depending on the physical parameters of the structures — in particular, the difference in Zeeman splittings, the detuning and the tunnel coupling — the native two-qubit gate can be either the $\sqrt{\text{SWAP}}$ or the C-PHASE. To prove the validity and identify the limits of the proposed approach, the simulation methodology is tested by emulating the execution of several quantum algorithms on two semiconductor heterostructures — SiGe and SiMOS — with two different sets of input physical parameters: the first set — henceforth referred to as $\sqrt{\text{SWAP}}$-*regime* — encompasses values routinely found in experimental devices intended to exploit the $\sqrt{\text{SWAP}}$ gate as the native two-qubit gate, whereas the second one — henceforth referred to as *C-PHASE-regime* — consists of values routinely found in experimental devices intended to exploit the C-PHASE gate as the native two-qubit gate. The physical and (some) control parameters — extracted from experimental data or obtained with simulations — are reported in Table 7. Since the values of the tunnel coupling t_0 and the detuning ϵ for multi-qubit gates directly influence the duration of the native gates, they are determined[10] considering realistic gate times from experimental data [21], [63], [88], [89]. Equation (51), Equation (56) and Equation (44) allow retrieving the corresponding voltages to be applied to the inter-dot barrier gate. Once the duration of single-qubit gates τ_{sq} is fixed according to Table 7, the corresponding value of the microwave magnetic field is

$$B_w = \frac{\theta}{|\gamma| \tau_{sq}}, \qquad (62)$$

---

[10]The t_0 values are coherent with the simulation results from Section IV.

where θ is the rotation angle of the single-qubit gate. The quantum algorithms presented in Section V-B2 are simulated by fixing the amplitude of the pulse ($\propto B_w$) to an optimised value and varying the pulse width (τ) according to the quantum gate that has to be implemented.

B. RESULTS

This section collects the obtained results. Firstly, for each heterostructure and for each two-gate scenario, the microwave pulse amplitude is optimised computing, via direct Hamiltonian integration with QuTiP [15], the fidelity when a set of gates is sequentially applied to all qubits, for different values of the pulse width and amplitude. Then, the τ_{sq} value that maximises the device fidelity is used to compare the MATLAB model and the QuTiP results.
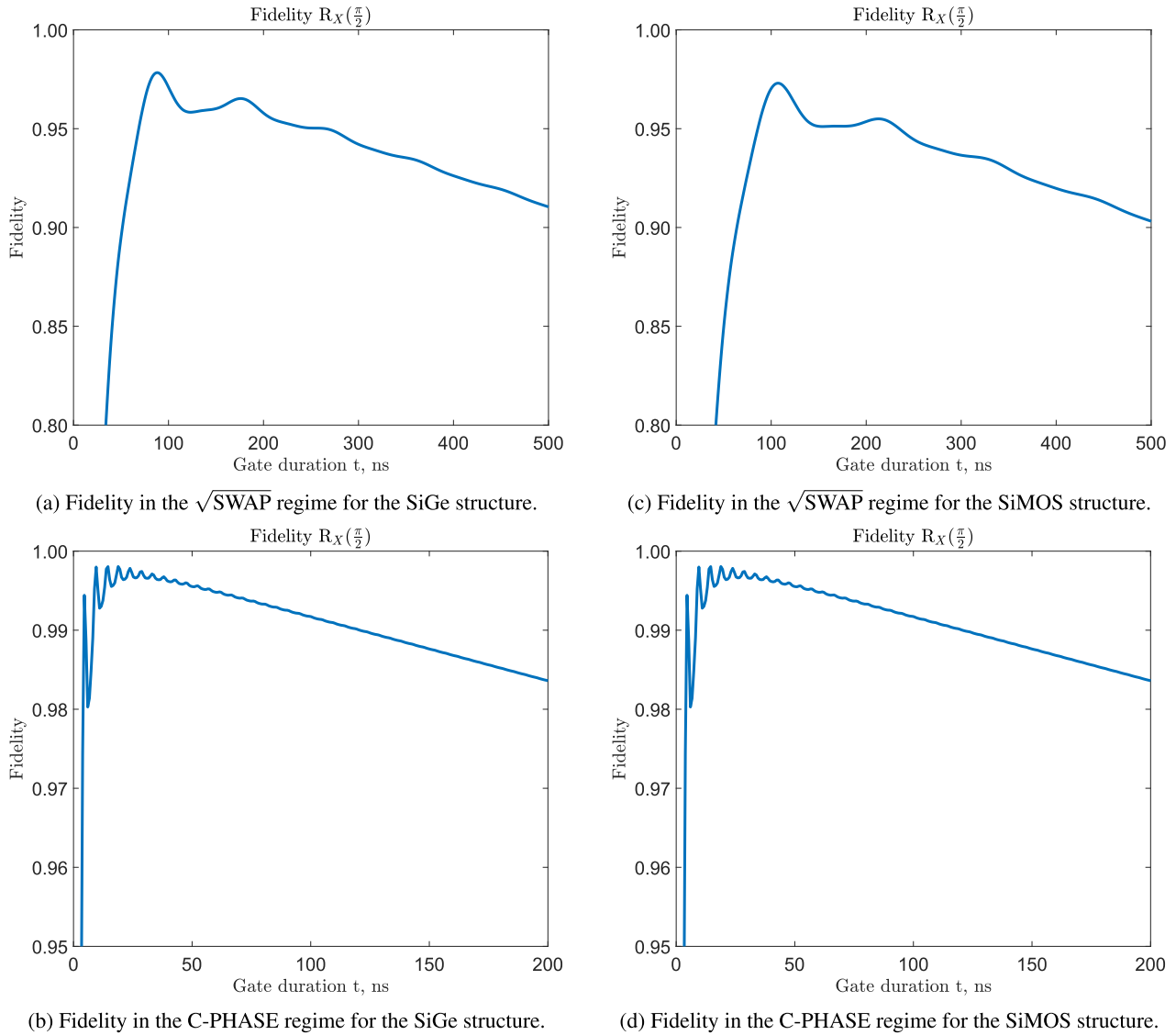
1) FIDELITY OPTIMISATION

The fidelity is calculated — resorting to Equation (58) — by applying a sequence of $R_x(\frac{\pi}{2})$ from the most significant qubit (q_1) to the least significant one (q_0), for different values of the pulse width and amplitude, and comparing the output noisy density matrix of QuTiP with the expected ideal state-vector. In analogy with [20], the choice of this kind of benchmark is motivated by the fact that the rotation of $\pi/2$ about $\hat{x}$ axis is a fundamental rotation to implement quantum gates and by the fact that once a qubit is along the $-\hat{y}$ axis, it is sensitive to the unwanted exchange coupling evolution which mainly causes an unwanted rotation about $\hat{z}$.

a: SiGe HETEROSTRUCTURE

The behaviour of the fidelity for different pulse amplitudes is reported in Figure 20a and Figure 20b for both the $\sqrt{\text{SWAP}}$ and C-PHASE scenarios. The fidelity plots show a noteworthy ringing whose periods $T = 2\pi/|\Delta\omega_0|$ coincide with the period of the Hamiltonian of Equation (16), where the term in square brackets represents the unwanted effects that a field intended to act on qubit 0 has on qubit 1. Therefore, local maxima occur when the time interval is an integer multiple of the period of the unwanted time-dependent part of the overall rotating-frame Hamiltonian. The optimal time duration τ_{sq} for a single-qubit gate should be sufficiently long for the corresponding Fourier spectrum to be selective on the frequency of the target qubit. At the same time, it should be sufficiently short to minimize the unwanted evolution due to the residual non-zero coupling and to the relaxation and decoherence phenomena. Therefore, as already discussed in [20] and considering the noise model of Section III-F1, the single-qubit pulse width shall be such that:

$$\frac{2\pi}{|\Delta\omega_0|} \ll \tau_{sq} \ll \min\left\{ \frac{1}{|J_{\text{off}}|}, \frac{\prod_i^n T_2^{*i}}{\sum_i^n T_2^{*i}}, \frac{\prod_i^n T_1^i}{\sum_i^n T_1^i} \right\}, \qquad (63)$$

where J_{off} is the residual exchange interaction in the single-qubit regime. Accordingly, the optimal τ_{sq} and the corresponding optimal B_w to be used in the simulation of the

(a) Fidelity in the $\sqrt{\text{SWAP}}$ regime for the SiGe structure.

(c) Fidelity in the $\sqrt{\text{SWAP}}$ regime for the SiMOS structure.

(b) Fidelity in the C-PHASE regime for the SiGe structure.

(d) Fidelity in the C-PHASE regime for the SiMOS structure.

FIGURE 20. QuTiP fidelity of a sequence of $R_X(\frac{\pi}{2})$ gate on each qubit in the $\sqrt{\text{SWAP}}$ and C-PHASE regimes for SiGe and SiMOS heterostructures.

quantum algorithms are:

$$\tau_{sq}^{\sqrt{\text{SWAP}}} = 88.68 \text{ ns} \longrightarrow B_w^{\sqrt{\text{SWAP}}} = 101.25 \text{ μT},$$
$$\tau_{sq}^{\text{C-PHASE}} = 10.69 \text{ ns} \longrightarrow B_w^{\text{C-PHASE}} = 820.29 \text{ μT},$$
$$(64)$$

where $\tau_{sq}^{\sqrt{\text{SWAP}}}$ is the single-qubit gate duration in the $\sqrt{\text{SWAP}}$ regime and similarly for $\tau_{sq}^{\text{C-PHASE}}$.

b: SiMOS HETEROSTRUCTURE

The behaviour of the fidelity for different pulse amplitudes is reported in Figure 20c and Figure 20d for both the $\sqrt{\text{SWAP}}$ and C-PHASE scenarios. As in the SiGe case, the fidelity plots show a remarkable ringing whose periods $T = 2\pi / |\Delta\omega_0|$ coincide with the period of the Hamiltonian of Equation (16). The optimal τ_{sq} and the corresponding optimal B_w to be used in the simulation of the quantum algorithms are:

$$\tau_{sq}^{\sqrt{\text{SWAP}}} = 107.22 \text{ ns} \longrightarrow B_w^{\sqrt{\text{SWAP}}} = 83.78 \text{ μT},$$

$$\tau_{sq}^{\text{C-PHASE}} = 14.20 \text{ ns} \longrightarrow B_w^{\text{C-PHASE}} = 630.16 \text{ μT}.$$
$$(65)$$

2) SIMULATION OF QUANTUM ALGORITHMS

The simulation of quantum algorithms shows promising results in terms of the MATLAB model performance. Indeed, as shown in Tables 8 to 11, it is always capable of correctly simulating the algorithms in tens of milliseconds, while the QuTiP simulation takes tens of seconds. However, results are quite different depending on the device scenario. Overall, the simulations are worse for the $\sqrt{\text{SWAP}}$ case, substantiating the MATLAB-QuTiP error analysis carried out in Section III-E. The lowest fidelities occur for the Deutsch-Josza and the Grover algorithms, with the QuTiP simulation giving wrong results. It can be speculated this is due to a greater effect of the non-idealities — such as off-resonance effects — especially considering the fairly long duration of the single-qubit gates. In order to check this, the algorithms have been

TABLE 7. Physical and control parameters adopted in the simulations. For the tunnel coupling t_0, the detuning ϵ and the gate duration τ, sq refers to the values used when carrying out single-qubit gates, whereas mq stands for the multi-qubit gate regime. The acronym asm. denotes an assumed parameter.

Parameter		SiGe				SiMOS			
		$\sqrt{\text{SWAP}}$	ref.	C-PHASE	ref.	$\sqrt{\text{SWAP}}$	ref.	C-PHASE	ref.
U		0.9 meV	[88]	0.9 meV	[88]	0.9 meV	[88]	0.9 meV	[88]
t_0	sq	41.357 feV	[32]	41.357 feV	[32]	41.357 feV	[32]	41.357 feV	[32]
	mq	3.308 µeV	[20]	2.895 µeV	[20]	3.308 µeV	[21]	1.654 µeV	Paragraph IV-D3c
ϵ	sq	0 eV	asm.	0 eV	asm.	0 eV	asm.	0 eV	asm.
	mq	0.7 meV	[20]	0.3 meV	[20]	0.7 meV	[20]	0.3 meV	[20]
f_0^0		6.950 GHz	[89]	15.600 GHz	[22]	6.949 GHz	[21]	15.43 GHz	[63]
f_0^1		6.961 GHz	[89]	15.880 GHz	[22]	6.958 GHz	[21]	15.64 GHz	[63]
ΔE_z		45.492 neV	[89]	1157.987 neV	[22]	37.221 neV	[21]	868.490 neV	[63]
B_0		250 mT	[89]	557 mT	asm.	250 mT	[21]	560 mT	asm.
τ	sq	88.68 ns	Eq. (64)	10.69 ns	Eq. (64)	107.22 ns	Eq. (65)	14.20 ns	Eq. (65)
	mq	9.00 ns	[89]	41.67 ns	[21]	9.00 ns	[88]	150 ns	[63]
T_1	q[0]	2.0 ms	[21]	2.0 ms	[21]	2.0 ms	[21]	20 ms	[63]
	q[1]	3.7 ms	[21]	3.7 ms	[21]	3.7 ms	[21]	20 ms	[63]
T_2^*	q[0]	3.7 µs	[22]	3.0 µs	[22]	2.1 µs	[21]	7.1 µs	[63]
	q[1]	3.7 µs	[22]	2.5 µs	[22]	2.7 µs	[21]	5.2 µs	[63]

performed again on QuTiP with a larger ΔE_z to mitigate the off-resonance. This resulted in a correct simulation with higher fidelity, confirming that the $\sqrt{\text{SWAP}}$ scenario strongly suffers from the relatively low ΔE_z. Moreover, also the error between the MATLAB model and QuTiP is worse for these two algorithms. This may be due to the discrepancies between the two models when taking non-idealities into account. On the other hand, the C-PHASE scenario shows excellent results in every field. The fidelities are always higher than 90% and the error and the KL divergence between the two models are generally low. Instead, the differences between the SiGe and SiMOS structures are very few and they almost only arise from the non-identical T_1 and T_2^* parameters and duration of the single-qubit gates. Indeed, for the $\sqrt{\text{SWAP}}$ case, the SiGe simulations yield lower errors since, as shown in Table 7, the single-qubit gates are slightly faster and the T_2^* is better with respect to the SiMOS counterpart. On the other hand, the T_2^* of the SiMOS structure in the C-PHASE regime is quite bigger than the T_2^* of the SiGe case, thus resulting in higher fidelities.

VI. CONCLUSION

Moving from the analysis of the qubits' physical systems — in terms of many-body Hamiltonian characterisation — this article, on the one hand, discusses the derivation of a novel CPU-friendly compact model for semiconductor quantum dots systems for quantum computers, which leverages the methodology introduced in [20] and [19], and on the other hand, it proposes the development a comprehensive classical simulation toolchain that, starting from currently available physical-level simulators or experimental values and an arbitrary quantum circuit described in `OpenQASM`

`2.0` — which is compiled by an in-house technology-aware compilation toolchain —, can determine the expected outcomes in terms of the eigenstate probability distribution, the fidelity and the execution time.

Even though this work does not propose a definitive model and shall be regarded as a first step towards the development of a simulation toolchain able to assist the engineering of semiconductor quantum dot devices, the obtained results are encouraging. Indeed, the comparison of the outcomes provided by the model with those provided by QuTiP [15] — a software tool able to solve the Lindblad master equation for the density matrix — for several quantum circuits and for two different heterostructures — namely a SiGe-Si-SiGe one and a Si-SiO$_2$ one — proves that, on the one hand, the model can support different families of semiconductor heterostructures, and on the other hand, it is well performing in the simulation where the native gate is the C-PHASE, whereas the error is slightly but notably higher in the $\sqrt{\text{SWAP}}$ case. These preliminary results justify the development of a *fast intermediate-level* simulation infrastructure capable of providing physically-reliable evaluations of the execution of quantum algorithms on some target devices. As a matter of fact, one of the most relevant advantages of the compact model methodology is its simulation time. Whereas the QuTiP simulations are computationally demanding — taking even hours for the most precise simulations ($\sim$ 1200 data points) — the MATLAB model takes at most seconds for the same set of simulations.

The germinal proposal of a multi-level simulation infrastructure, which mimics the well-established approach of classical electronics, seems to be a reasonable approach for the optimal analysis of the design space of real-world quan-

TABLE 8. The table reports the fidelity $\mathcal{F}_M$ ($\mathcal{F}_Q$) and the most probable eigenstate MPE$_M$ (MPE$_Q$) resulting from the MATLAB simulator (QuTiP [15] direct integration), the divergence $\mathcal{D}_{KL}$ between the eigenstate probability distribution provided by the model and that obtained with QuTiP, the percentage 2-norm $\varepsilon_\%$ of the difference between the corresponding two density matrices and the wall-clock time required to emulate the execution of the quantum algorithms with the MATLAB model (t_M^{ck}) and the QuTiP direct integration (t_Q^{ck}) for the $\sqrt{\text{SWAP}}$ scenario for the SiGe heterostructure.

SiGe Heterostructure								
	$\sqrt{\text{SWAP}}$							
Algorithm		$\mathcal{F}_M$	$\mathcal{F}_Q$	MPE$_M$	MPE$_Q$	$\mathcal{D}_{KL}$	$\varepsilon_\%$	t_M^{ck}	t_Q^{ck}
cnot_01	[20]	91.02%	88.37%	$|11\rangle$	$|11\rangle$	1.77	16.9%	18.6 ms	8.85 s
dcx_01	[20]	82.7%	78.45%	$|10\rangle$	$|10\rangle$	1.69	19.38%	23.15 ms	19.16 s
iswap_01	[20]	73.07%	68.46%	$|10\rangle$	$|10\rangle$	4.54	14.59%	46.51 ms	25.95 s
dj_balanced	[20]	83.23%	41.51%	$|01\rangle$	$|10\rangle$	87.69	54.23%	36.11 ms	15.18 s
grover_10	[20]	67.12%	50.95%	$|10\rangle$	$|00\rangle$	14.64	23.20%	43.44 ms	32.94 s
SWAP_01	[20]	75.71%	70.03%	$|10\rangle$	$|10\rangle$	2.35	17.98%	45.05 ms	34.37 s

TABLE 9. The table reports the fidelity $\mathcal{F}_M$ ($\mathcal{F}_Q$) and the most probable eigenstate MPE$_M$ (MPE$_Q$) resulting from the MATLAB simulator (QuTiP [15] direct integration), the divergence $\mathcal{D}_{KL}$ between the eigenstate probability distribution provided by the model and that obtained with QuTiP, the percentage 2-norm $\varepsilon_\%$ of the difference between the corresponding two density matrices and the wall-clock time required to emulate the execution of the quantum algorithms with the MATLAB model (t_M^{ck}) and the QuTiP direct integration (t_Q^{ck}) for the C-PHASE scenario for the SiGe heterostructure.

SiGe Heterostructure								
	C-PHASE							
Algorithm		$\mathcal{F}_M$	$\mathcal{F}_Q$	MPE$_M$	MPE$_Q$	$\mathcal{D}_{KL}$	$\varepsilon_\%$	t_M^{ck}	t_Q^{ck}
cnot_01	[20]	98.63%	97.9%	$|11\rangle$	$|11\rangle$	0.6	8.49%	30.35 ms	3.75 s
dcx_01	[20]	97.05%	95.93%	$|10\rangle$	$|10\rangle$	0.56	16.51%	35.83 ms	7.2 s
iswap_01	[20]	93.58%	92.23%	$|10\rangle$	$|10\rangle$	1.09	10.13%	42.63 ms	8.88 s
dj_balanced	[20]	96.86%	89.27%	$|01\rangle$	$|01\rangle$	10.95	36.25%	33.05 ms	6.08 s
grover_10	[20]	91.62%	89.01%	$|10\rangle$	$|10\rangle$	2.36	17.65%	40.28 ms	10.18 s
SWAP_01	[20]	95.74%	93.54%	$|10\rangle$	$|10\rangle$	1.66	19.86%	53.21 ms	11.76 s

TABLE 10. The table reports the fidelity $\mathcal{F}_M$ ($\mathcal{F}_Q$) and the most probable eigenstate MPE$_M$ (MPE$_Q$) resulting from the MATLAB simulator (QuTiP [15] direct integration), the divergence $\mathcal{D}_{KL}$ between the eigenstate probability distribution provided by the model and that obtained with QuTiP, the percentage 2-norm $\varepsilon_\%$ of the difference between the corresponding two density matrices and the wall-clock time required to emulate the execution of the quantum algorithms with the MATLAB model (t_M^{ck}) and the QuTiP direct integration (t_Q^{ck}) for the $\sqrt{\text{SWAP}}$ scenario for the SiMOS heterostructure.

SiMOS Heterostructure								
	$\sqrt{\text{SWAP}}$							
Algorithm		$\mathcal{F}_M$	$\mathcal{F}_Q$	MPE$_M$	MPE$_Q$	$\mathcal{D}_{KL}$	$\varepsilon_\%$	t_M^{ck}	t_Q^{ck}
cnot_01	[20]	83.82%	82.76%	$|11\rangle$	$|11\rangle$	1.09	14.5%	18.87 ms	11.4 s
dcx	[20]	71.40%	69.29%	$|10\rangle$	$|10\rangle$	1.03	11.87%	24.84 ms	23.07 s
iswap_01	[20]	61.43%	58.18%	$|10\rangle$	$|10\rangle$	1.40	7.61%	28.59 ms	28.20 s
dj_balanced_01	[20]	73.08%	48.40%	$|01\rangle$	$|10\rangle$	31.42	33.32%	25.10 ms	14.09 s
grover_10	[20]	55.86%	50.14%	$|10\rangle$	$|00\rangle$	2.09	8.35%	31.83 ms	35.83 s
SWAP_01	[20]	62.48%	69.29%	$|10\rangle$	$|10\rangle$	4.17	17.87%	27.95 ms	25.01 s

tum devices. The presence of different levels of abstractions, starting from the physical simulation (FEM and/or ab-initio) whose outcomes — possibly with some approximations as done for the tunnel coupling — are provided to the compact models, up to the quantum algorithms, should ease and accelerate the design of practical devices able to meet the requirements of a rapidly inflating application-driven market. Indeed, the quantum engineer, once the toolchain is completed, shall be able to conceive and design a physical architecture resorting to low-level simulators, then extract the relevant physical parameters, carry out a fast compact model-based simulation of a set of quantum algorithms to benchmark the device and come back to optimise the physical layout.

A latere, it shall be noted that the smooth integration of the semiconductor quantum dot compact model in the simulation

TABLE 11. The table reports the fidelity $\mathcal{F}_M$ ($\mathcal{F}_Q$) and the most probable eigenstate MPE$_M$ (MPE$_Q$) resulting from the MATLAB simulator (QuTiP [15] direct integration), the divergence $\mathcal{D}_{KL}$ between the eigenstate probability distribution provided by the model and that obtained with QuTiP, the percentage 2-norm $\varepsilon_\%$ of the difference between the corresponding two density matrices and the wall-clock time required to emulate the execution of the quantum algorithms with the MATLAB model (t_M^{ck}) and the QuTip direct integration (t_Q^{ck}) for the C-PHASE scenario for the SiMOS heterostructure.

SiMOS Heterostructure								
C-PHASE								
Algorithm		$\mathcal{F}_M$	$\mathcal{F}_Q$	MPE$_M$	MPE$_Q$	$\mathcal{D}_{KL}$	$\varepsilon_\%$	t_M^{ck}	t_Q^{ck}
cnot_01	[20]	99.40%	98.23%	$|11\rangle$	$|11\rangle$	1.82	6.57%	19.59 ms	3.45 s
dcx	[20]	98.65%	96.75%	$|10\rangle$	$|10\rangle$	2.48	13.14%	19.97 ms	7.01 s
iswap_01	[20]	97.02%	93.29%	$|10\rangle$	$|10\rangle$	4.44	13.69%	21.94 ms	9.63 s
dj_balanced_01	[20]	98.31%	90.43%	$|01\rangle$	$|01\rangle$	14.44	37.43%	20.51 ms	5.74 s
grover_10	[20]	95.50%	89.02%	$|10\rangle$	$|10\rangle$	9.26	25.79%	23.90 ms	10.92 s
SWAP	[20]	98.04%	94.97%	$|10\rangle$	$|10\rangle$	3.63	16.54%	26.43 ms	12.17 s

infrastructure of [20] proves the claim that the methodology envisioned in [20] — encompassing the compact model approach, the Fourier model and the relaxation and decoherence algorithms — can be straightforwardly extended to other quantum technologies.

Overall, the compact model approach has proved to be capable of handling quite accurately a quantum circuit simulation. Moreover, the versatility of the proposed methodology will enable the introduction of several types of enhancement. First and foremost, the compact model for quantum dots shall be extended to support architectures with an arbitrary number of qubits (as already done for NMR and molecular nanomagnets). The main problem concerning this point is that the Fermi-Hubbard model Hamiltonian scales very fast with the number of qubits. A possible solution could be to adopt a Heisenberg NMR-like model and derive the Heisenberg coupling constants between neighbouring dots from the Fermi-Hubbard model. Secondly, another improvement to mention is the modelling of the state readout operation. Indeed, this operation — which has to be performed in a very precise manner in order to yield a correct outcome [54] — directly influences the outcome of real hardware, since it is always carried out after the manipulation, and it can introduce a large amount of noise. Thirdly, additional noise sources — such as the temperature, the valley physics, the interaction with the magnetic field, the charge noise [90], the nuclear spin noise, and the possible disturbances affecting the EM signals — should be included in the compact model and their relation with the T_1 and T_2^* experimental constants shall be investigated. These last two improvements are expected to foster a fairer and more reliable comparison with hardware devices, thus paving the way for constructive feedback between experimental devices and simulation, which is the actual aim of the development of this toolchain. Fourthly, the capabilities of the simulation infrastructure shall be broadened, by adding support for other quantum dot encodings (for instance, singlet-triplet and exchange-only encodings) and other solid-state technologies, such as donor-based [91] and hole-based qubits [92]. Finally, the physical-level simulation must be improved to allow

for the computation of other physical parameters, such as the on-site coulomb energy U and the singlet-triplet splitting J. In this regard, it would be interesting to compare the value of J calculated starting from t_0 (as done in this article) with that determined as the singlet-triplet splitting.

In conclusion, it can be stated that the route towards practically employable quantum computing must inevitably pass through quantum device engineering. Even if the prototype model proposed in this article is still a work in progress, it might be regarded as a step forward towards the enhancement of semiconductor quantum devices.

APPENDIX. DENSITY MATRIX FORMALISM

In a finite-dimension complex Hilbert space $\mathbb{H}^N$ equipped with a complete orthonormal basis $|e_i\rangle_{0 \leq i < N}$, the Fisher-Riesz theorem ensures that a pure single-particle state can be represented — according to Dirac's representation of quantum mechanics — by an abstract state vector $|\psi\rangle$, which can be expanded as a Fourier series over the basis [93]

$$|\psi\rangle = \sum_i c_i |e_i\rangle , \qquad (66)$$

where the coefficients c_i can be interpreted as complex probability amplitudes. It is well-known that — according to the probabilistic interpretation of quantum mechanics — the probability p_i to measure the basis state $|e_i\rangle$ is $p_i = |c_i|^2$. The time evolution of a pure state is ruled by the Schrödinger equation. However, many real-world quantum physical systems — such as those interacting with the external environment through decoherence and relaxation phenomena — require a description in terms of so-called **mixed states**, instead of pure states. This means that a semi-classical probability distribution of pure states $|\psi_i\rangle$, each of them occurring with a probability p_i, is associated with the quantum state [94], [95], [96]. In these cases, the most appropriate methodology is to describe the system by adopting the **density matrix** formalism

$$\rho = \sum_i p_i |\psi_i\rangle\langle\psi_i| . \qquad (67)$$

The density matrix of a pure state is $\rho = |\psi\rangle\langle\psi|$. The elements on the main diagonal of ρ are, by definition, the probabilities of finding the system in a basis state. Hence its trace — i.e., the sum of the terms on the main diagonal — is always equal to one. The time evolution of a system described by a density matrix ρ is given by the Liouville – von Neumann equation [95]:

$$i\hbar \frac{d\rho}{dt} = [\mathcal{H}(t), \rho], \tag{68}$$

where $\mathcal{H}(t)$ is the Hamiltonian of the system with explicit time dependence and $[A, B] = AB - BA$ is the commutator [51]. The time evolution of mixed states is customarily represented as:

$$\rho(t) = U(t)\rho(t = 0)U(t)^\dagger, \tag{69}$$

where the unitary time evolution operator $U(t)$ is a *formal* solution of the Liouville – von Neuman equation

$$U(t) = \mathcal{T} \exp\left\{-\frac{i}{\hbar} \int_{t_0}^t \mathcal{H}(\tau) d\tau\right\}, \tag{70}$$

and $\mathcal{T}$ represents the *time-ordered product*. The evolution operator allows the definition of quantum gates and quantum algorithms on physical devices. As a matter of fact, given a system described by a Hamiltonian $\mathcal{H}_{\text{sys}}(t)$ and a control Hamiltonian $\mathcal{H}_{\text{ctr}}(t; \eta(t))$, the expected unitary transformation U_{alg} can be achieved if there exists a set of control parameters $\eta(t)$ (as the phase and frequency of the applied field) of the total Hamiltonian $\mathcal{H}(t; \eta(t)) = \mathcal{H}_{\text{sys}}(t) + \mathcal{H}_{\text{ctr}}(t; \eta(t))$ such that the time evolution operator [62]

$$U[t, \eta(t)] = \mathcal{T} \exp\left\{-\frac{i}{\hbar} \int_{t_0}^t \mathcal{H}(\tau; \eta(\tau)) d\tau\right\} \tag{71}$$

is as similar as possible to U_{alg}. If the Hamiltonian does not show any explicit time dependence and the control parameters are taken to be piecewise constant — i.e., in each time step $t_k \rightarrow t_{k+1}$ they are chosen such that the corresponding evolution operator $U(t_{k+1})$ implements the desired quantum gate — then this operator reduces to [95]

$$U[t, \eta(t)] = \mathcal{T} \exp\left\{-\frac{i}{\hbar} \int_{t_0}^t \mathcal{H}(\eta(\tau)) d\tau\right\}$$
$$= e^{-\frac{i}{\hbar} \int_{t_{n-1}}^{t_n} \mathcal{H}(\eta(t_{n-1})) d\tau} \cdots e^{-\frac{i}{\hbar} \int_{t_0}^{t_1} \mathcal{H}(\eta(t_0)) d\tau}$$
$$= e^{-\frac{\mathcal{H}(\eta(t_n)) \cdot (t_{n-1} - t_n)}{\hbar} d\tau} \cdots e^{-\frac{\mathcal{H}(\eta(t_0)) \cdot (t_1 - t_0)}{\hbar} d\tau}$$
$$= U(t_n) \cdots U(t_1). \tag{72}$$

APPENDIX. MATRIX EXPRESSION OF THE FERMI HUBBARD HAMILTONIAN

In the following, $a^\dagger$ is the microscopic construction operator and a the destruction operator satisfying the fermionic algebraic character

$$\{a_\chi, a_\xi^\dagger\} = \delta_{\chi,\xi}, \quad \{a_\chi^\dagger, a_\xi^\dagger\} = 0 = \{a_\chi, a_\xi\} \quad \forall \chi\, \xi \tag{73}$$

where $\{A, B\} = AB + BA$ denotes the fermionic anticommutator and δ is the Kronecker delta. Adopting this notation, the second-quantization components of Equation (5) are [57], [97], [98], [99]:

- On-site energy (detuning between the dots)

$$\mathcal{H}_\epsilon = \sum_{\sigma,v,k} \mu_k n_{\sigma,v,k}, \tag{74}$$

where $n = a^\dagger a$ is the microscopic fermionic number operator and μ_k is the chemical potential of dot k. This Hamiltonian introduces an energy contribution that takes into account the number of electrons in every dot, spin state and valley state, weighted by the chemical potentials of the dots. As shown in the Appendix, thanks to the antiparallel spin arrangement of the electrons in the singlet states, the net effect of the component is to add an energy contribution proportional to the detuning (the difference in chemical potentials of the two dots) between the two dots $\epsilon = \mu_1 - \mu_0$ that, according to the sign of the detuning itself, increases/reduces the energy of the singlet states.

- Valley degeneracy

$$\mathcal{H}_v = \sum_{\sigma,k} \frac{1}{2} \left(n_{\sigma,+,k} - n_{\sigma,-,k}\right). \tag{75}$$

- On-site Coulomb repulsion

$$\mathcal{H}_u = \sum_{\sigma,v,k} \sum_{\sigma',v'} \frac{U_k}{2} n_{\sigma,v,k} n_{\sigma',v',k} \quad \sigma, v \neq \sigma', v', \tag{76}$$

where U_k is the on-site interaction energy of the quantum dot, i.e., the energy required for moving both electrons in the same dot. Hence, this term accounts for the Coulomb interaction between two electrons residing on the same site and therefore is a simplification of the full Coulomb interaction term, which includes other interactions, such as that between electrons in different dots [54].

- Hopping term

$$\mathcal{H}_t = -\sum_{v,k} \sum_{v',k'} t_0 \left(a_{\uparrow,v,k}^\dagger a_{\uparrow,v',k'} + a_{\downarrow,v,k}^\dagger a_{\downarrow,v',k'}\right)$$
$$k, v \neq k', v', \tag{77}$$

where t_0 is the tunnel coupling (in energy units). This term accounts for electron tunnelling between two sites.

- Zeeman term

$$\mathcal{H}_z = \sum_{k,v} \frac{E_{z_k}}{2} \left(n_{\uparrow,k,v} - n_{\downarrow,k,v}\right), \tag{78}$$

where E_{z_k} is the Zeeman energy.

In order to derive the matrix expression of the Fermi-Hubbard Hamiltonian, one can consider the six lowest energy states (thus neglecting the valley contribution) for two electrons in two dots. Under this assumption, the physical basis can be

expressed by exploiting the second-quantization microscopic fermionic operators acting on the vacuum state $|0\rangle$ as [100]:

$$|\uparrow\uparrow\rangle = a_{\uparrow,1}^\dagger a_{\uparrow,0}^\dagger |0\rangle ,$$

$$|\uparrow\downarrow\rangle = a_{\uparrow,1}^\dagger a_{\downarrow,0}^\dagger |0\rangle ,$$

$$|\downarrow\uparrow\rangle = a_{\downarrow,1}^\dagger a_{\uparrow,0}^\dagger |0\rangle ,$$

$$|\downarrow\downarrow\rangle = a_{\downarrow,1}^\dagger a_{\downarrow,0}^\dagger |0\rangle ,$$

$$|S(0,2)\rangle = \frac{1}{\sqrt{2}} |0, \uparrow\downarrow - \downarrow\uparrow\rangle = a_{\downarrow,0}^\dagger a_{\uparrow,0}^\dagger |0\rangle ,$$

$$|S(2,0)\rangle = \frac{1}{\sqrt{2}} |\uparrow\downarrow - \downarrow\uparrow, 0\rangle = a_{\downarrow,1}^\dagger a_{\uparrow,1}^\dagger |0\rangle . \quad (79)$$

A. ON-SITE ENERGY
The action of $\mathcal{H}_\epsilon$ on the $|\uparrow\uparrow\rangle$ basis state is:

$$\mathcal{H}_\epsilon |\uparrow\uparrow\rangle = \mathcal{H}_\epsilon a_{\uparrow,1}^\dagger a_{\uparrow,0}^\dagger |0\rangle$$
$$= \left[(\mu_0(n_{\downarrow,0} + n_{\uparrow,0}) + \mu_1(n_{\downarrow,1} + n_{\uparrow,1})\right] |\uparrow\uparrow\rangle \quad (80)$$

where

$$\begin{cases} \mu_0 a_{\downarrow,0}^\dagger a_{\downarrow,0} a_{\uparrow,1}^\dagger a_{\uparrow,0}^\dagger |0\rangle \to 0 \\ \mu_0 a_{\uparrow,0}^\dagger a_{\uparrow,0} a_{\uparrow,1}^\dagger a_{\uparrow,0}^\dagger |0\rangle \to \mu_0 |\uparrow\uparrow\rangle \\ \mu_1 a_{\downarrow,1}^\dagger a_{\downarrow,1} a_{\uparrow,1}^\dagger a_{\uparrow,0}^\dagger |0\rangle \to 0 \\ \mu_1 a_{\uparrow,1}^\dagger a_{\uparrow,1} a_{\uparrow,1}^\dagger a_{\uparrow,0}^\dagger |0\rangle \to \mu_1 |\uparrow\uparrow\rangle . \end{cases} \quad (81)$$

It follows similarly that

$$\langle\uparrow\uparrow| \mathcal{H}_\epsilon |\uparrow\uparrow\rangle = \mu_0 + \mu_1$$
$$\langle\uparrow\downarrow| \mathcal{H}_\epsilon |\uparrow\downarrow\rangle = \mu_0 + \mu_1$$
$$\langle\downarrow\uparrow| \mathcal{H}_\epsilon |\downarrow\uparrow\rangle = \mu_0 + \mu_1$$
$$\langle\downarrow\downarrow| \mathcal{H}_\epsilon |\downarrow\downarrow\rangle = \mu_0 + \mu_1 \quad (82)$$

For what concerns the singlet states with two electrons in the same dot, the action of $\mathcal{H}_\epsilon$ is:

$$\mathcal{H}_\epsilon |S(0,2)\rangle = \mathcal{H}_\epsilon a_{\downarrow,0}^\dagger a_{\uparrow,0}^\dagger |0\rangle$$
$$= \left[(\mu_0(n_{\downarrow,0} + n_{\uparrow,0}) + \mu_1(n_{\downarrow,1} + n_{\uparrow,1})\right] |S(0,2)\rangle \quad (83)$$

where

$$\begin{cases} \mu_0 a_{\downarrow,0}^\dagger a_{\downarrow,0} a_{\downarrow,0}^\dagger a_{\uparrow,0}^\dagger |0\rangle \to \mu_0 |S(0,2)\rangle \\ \mu_0 a_{\uparrow,0}^\dagger a_{\uparrow,0} a_{\downarrow,0}^\dagger a_{\uparrow,0}^\dagger |0\rangle \to \mu_0 |S(0,2)\rangle \\ \mu_1 a_{\downarrow,1}^\dagger a_{\downarrow,1} a_{\downarrow,0}^\dagger a_{\uparrow,0}^\dagger |0\rangle \to 0 \\ \mu_1 a_{\uparrow,1}^\dagger a_{\uparrow,1} a_{\downarrow,0}^\dagger a_{\uparrow,0}^\dagger |0\rangle \to 0 . \end{cases} \quad (84)$$

It follows similarly that

$$\langle S(0,2)| \mathcal{H}_\epsilon |S(0,2)\rangle = 2\mu_0$$
$$\langle S(2,0)| \mathcal{H}_\epsilon |S(2,0)\rangle = 2\mu_1 . \quad (85)$$

Since all non-diagonal terms can be shown to be zero, the on-site energy Hamiltonian reduces to

$$\mathcal{H}_\epsilon \sim \mathcal{H}_\epsilon - (\mu_0 + \mu_1)\mathbb{I}$$

$$= \begin{bmatrix} 0 & 0 & 0 & 0 & 0 & 0 \\ 0 & 0 & 0 & 0 & 0 & 0 \\ 0 & 0 & 0 & 0 & 0 & 0 \\ 0 & 0 & 0 & 0 & 0 & 0 \\ 0 & 0 & 0 & 0 & -\epsilon & 0 \\ 0 & 0 & 0 & 0 & 0 & \epsilon \end{bmatrix} , \quad (86)$$

where $(\mu_0 + \mu_1)\mathbb{I}$ only causes an irrelevant rigid shift of the energy eigenspectrum and can be ignored.

B. COULOMB ON-SITE ENERGY
The action of the on-site Coulomb Hamiltonian on the basis states can be retrieved by direct inspection of Equation (76): indeed, when $\mathcal{H}_u$ acts on a basis state, it gives non-zero contribution only for the sites k in which both $n_{\uparrow,k}$ and $n_{\downarrow,k}$ count one fermion. Accordingly, all terms in the (1, 1) block of the Hamiltonian are zero. The action of $\mathcal{H}_u$ on the singlet states is:

$$\mathcal{H}_u |S(0,2)\rangle = \mathcal{H}_u a_{\downarrow,0}^\dagger a_{\uparrow,0}^\dagger |0\rangle$$
$$= (U_0 \cdot n_{\downarrow,0} n_{\uparrow,0} + U_1 \cdot n_{\downarrow,1} n_{\uparrow,1}) |S(0,2)\rangle \quad (87)$$

where it has been exploited that $[n_\chi, n_\xi] = 0 , \forall \chi \neq \xi$. Then,

$$\begin{cases} U_0 a_{\downarrow,0}^\dagger a_{\downarrow,0} a_{\uparrow,0}^\dagger a_{\downarrow,0}^\dagger a_{\uparrow,0}^\dagger |0\rangle \to \\ U_1 a_{\downarrow,1}^\dagger a_{\downarrow,1} a_{\uparrow,1}^\dagger a_{\uparrow,1} a_{\downarrow,0}^\dagger a_{\uparrow,0}^\dagger |0\rangle \to \end{cases}$$
$$\begin{cases} U_0 a_{\downarrow,0}^\dagger a_{\uparrow,0}^\dagger a_{\downarrow,0} a_{\downarrow,0}^\dagger a_{\uparrow,0} a_{\uparrow,0}^\dagger |0\rangle \to U_0 |S(0,2)\rangle \\ U_1 a_{\downarrow,1}^\dagger a_{\downarrow,1} a_{\downarrow,0}^\dagger a_{\uparrow,0}^\dagger a_{\uparrow,1}^\dagger a_{\uparrow,1} |0\rangle \to 0, \end{cases} \quad (88)$$

where the algebraic properties of fermionic operators have been exploited. Therefore,

$$\langle S(0,2)| \mathcal{H}_u |S(0,2)\rangle = U_0$$
$$\langle S(2,0)| \mathcal{H}_u |S(2,0)\rangle = U_1 \quad (89)$$

are the only non-zero terms.

C. HOPPING ENERGY
The action of $\mathcal{H}_t$ on $|\uparrow\uparrow\rangle$ and $|\downarrow\downarrow\rangle$ leads to all-zero columns since the tunnelling is Pauli-spin blocked. For two spinful fermions in two sites, Equation (77) reduces to

$$\mathcal{H}_t = -t_0 \left(a_{\uparrow,0}^\dagger a_{\uparrow,1} + a_{\downarrow,0}^\dagger a_{\downarrow,1} + a_{\uparrow,1}^\dagger a_{\uparrow,0} + a_{\downarrow,1}^\dagger a_{\downarrow,0} \right) \quad (90)$$

Considering the $|\uparrow\downarrow\rangle$ state:

$$\mathcal{H}_t |\uparrow\downarrow\rangle = \mathcal{H}_t a_{\uparrow,1}^\dagger a_{\downarrow,0}^\dagger |0\rangle$$
$$= t_0 \begin{cases} -a_{\uparrow,0}^\dagger a_{\uparrow,1} a_{\uparrow,1}^\dagger a_{\downarrow,0}^\dagger |0\rangle \\ -a_{\downarrow,0}^\dagger a_{\downarrow,1} a_{\uparrow,1}^\dagger a_{\downarrow,0}^\dagger |0\rangle \\ -a_{\uparrow,1}^\dagger a_{\uparrow,0} a_{\uparrow,1}^\dagger a_{\downarrow,0}^\dagger |0\rangle \\ -a_{\downarrow,1}^\dagger a_{\downarrow,0} a_{\uparrow,1}^\dagger a_{\downarrow,0}^\dagger |0\rangle \end{cases}$$

$$= t_0 \begin{cases} |S(0,2)\rangle \\ 0 \\ 0 \\ |S(2,0)\rangle \end{cases} . \tag{91}$$

Considering the $|\downarrow\uparrow\rangle$ state:

$$\mathcal{H}_t |\uparrow\downarrow\rangle = \mathcal{H}_t a_{\downarrow,1}^\dagger a_{\uparrow,0}^\dagger |0\rangle$$

$$= t_0 \begin{cases} -a_{\uparrow,0}^\dagger a_{\uparrow,1} a_{\downarrow,1}^\dagger a_{\uparrow,0}^\dagger |0\rangle \\ -a_{\downarrow,0}^\dagger a_{\downarrow,1} a_{\downarrow,1}^\dagger a_{\uparrow,0}^\dagger |0\rangle \\ -a_{\uparrow,1}^\dagger a_{\uparrow,0} a_{\downarrow,1}^\dagger a_{\uparrow,0}^\dagger |0\rangle \\ -a_{\downarrow,1}^\dagger a_{\downarrow,0} a_{\downarrow,1}^\dagger a_{\uparrow,0}^\dagger |0\rangle \end{cases}$$

$$= t_0 \begin{cases} 0 \\ -|S(0,2)\rangle \\ -|S(2,0)\rangle \\ 0 \end{cases} . \tag{92}$$

Considering the $|S(0,2)\rangle$ state:

$$\mathcal{H}_t |S(0,2)\rangle = \mathcal{H}_t a_{\downarrow,0}^\dagger a_{\uparrow,0}^\dagger |0\rangle$$

$$= t_0 \begin{cases} -a_{\uparrow,0}^\dagger a_{\uparrow,1} a_{\downarrow,0}^\dagger a_{\uparrow,0}^\dagger |0\rangle \\ -a_{\downarrow,0}^\dagger a_{\downarrow,1} a_{\downarrow,0}^\dagger a_{\uparrow,0}^\dagger |0\rangle \\ -a_{\uparrow,1}^\dagger a_{\uparrow,0} a_{\downarrow,0}^\dagger a_{\uparrow,0}^\dagger |0\rangle \\ -a_{\downarrow,1}^\dagger a_{\downarrow,0} a_{\downarrow,0}^\dagger a_{\uparrow,0}^\dagger |0\rangle \end{cases}$$

$$= t_0 \begin{cases} 0 \\ 0 \\ +|\uparrow\downarrow\rangle \\ -|\downarrow\uparrow\rangle \end{cases} . \tag{93}$$

Considering the $|S(2,0)\rangle$ state:

$$\mathcal{H}_t |S(2,0)\rangle = \mathcal{H}_t a_{\downarrow,1}^\dagger a_{\uparrow,1}^\dagger |0\rangle$$

$$= t_0 \begin{cases} -a_{\uparrow,0}^\dagger a_{\uparrow,1} a_{\downarrow,1}^\dagger a_{\uparrow,1}^\dagger |0\rangle \\ -a_{\downarrow,0}^\dagger a_{\downarrow,1} a_{\downarrow,1}^\dagger a_{\uparrow,1}^\dagger |0\rangle \\ -a_{\uparrow,1}^\dagger a_{\uparrow,0} a_{\downarrow,1}^\dagger a_{\uparrow,1}^\dagger |0\rangle \\ -a_{\downarrow,1}^\dagger a_{\downarrow,0} a_{\downarrow,1}^\dagger a_{\uparrow,1}^\dagger |0\rangle \end{cases}$$

$$= t_0 \begin{cases} -|\downarrow\uparrow\rangle \\ +|\uparrow\downarrow\rangle \\ 0 \\ 0 \end{cases} . \tag{94}$$

Accordingly, the matrix expression of $\mathcal{H}_t$ is

$$\mathcal{H}_t = \begin{bmatrix} 0 & 0 & 0 & 0 & 0 & 0 \\ 0 & 0 & 0 & 0 & t_0 & t_0 \\ 0 & 0 & 0 & 0 & -t_0 & -t_0 \\ 0 & 0 & 0 & 0 & 0 & 0 \\ 0 & t_0 & -t_0 & 0 & 0 & 0 \\ 0 & t_0 & -t_0 & 0 & 0 & 0 \end{bmatrix} . \tag{95}$$

D. ZEEMAN ENERGY

For two electrons in two sites, Equation (78) reduces to

$$\mathcal{H}_z = \frac{1}{2} \Big(E_{z_0} \left(a_{\uparrow,0}^\dagger a_{\uparrow,0} - a_{\downarrow,0}^\dagger a_{\downarrow,0} \right) + E_{z_1} \left(a_{\uparrow,1}^\dagger a_{\uparrow,1} - a_{\downarrow,1}^\dagger a_{\downarrow,1} \right) \Big) . \tag{96}$$

Considering the $|\uparrow\uparrow\rangle$ state:

$$\mathcal{H}_z |\uparrow\downarrow\rangle = \mathcal{H}_z a_{\uparrow,1}^\dagger a_{\uparrow,0}^\dagger |0\rangle$$

$$= \frac{1}{2} \begin{cases} +E_{z_0} a_{\uparrow,0}^\dagger a_{\uparrow,0} a_{\uparrow,1}^\dagger a_{\uparrow,0}^\dagger |0\rangle \\ -E_{z_0} a_{\downarrow,0}^\dagger a_{\downarrow,0} a_{\uparrow,1}^\dagger a_{\uparrow,0}^\dagger |0\rangle \\ +E_{z_1} a_{\uparrow,1}^\dagger a_{\uparrow,1} a_{\uparrow,1}^\dagger a_{\uparrow,0}^\dagger |0\rangle \\ -E_{z_1} a_{\downarrow,1}^\dagger a_{\downarrow,1} a_{\uparrow,1}^\dagger a_{\uparrow,0}^\dagger |0\rangle \end{cases}$$

$$= \frac{1}{2} \begin{cases} +E_{z_0} |\uparrow\uparrow\rangle \\ 0 \\ +E_{z_1} |\uparrow\uparrow\rangle \\ 0 \end{cases} = \overline{E}_z |\uparrow\uparrow\rangle . \tag{97}$$

Considering the $|\uparrow\downarrow\rangle$ state:

$$\mathcal{H}_z |\uparrow\downarrow\rangle = \mathcal{H}_z a_{\uparrow,1}^\dagger a_{\downarrow,0}^\dagger |0\rangle$$

$$= \frac{1}{2} \begin{cases} +E_{z_0} a_{\uparrow,0}^\dagger a_{\uparrow,0} a_{\uparrow,1}^\dagger a_{\downarrow,0}^\dagger |0\rangle \\ -E_{z_0} a_{\downarrow,0}^\dagger a_{\downarrow,0} a_{\uparrow,1}^\dagger a_{\downarrow,0}^\dagger |0\rangle \\ +E_{z_1} a_{\uparrow,1}^\dagger a_{\uparrow,1} a_{\uparrow,1}^\dagger a_{\downarrow,0}^\dagger |0\rangle \\ -E_{z_1} a_{\downarrow,1}^\dagger a_{\downarrow,1} a_{\uparrow,1}^\dagger a_{\downarrow,0}^\dagger |0\rangle \end{cases}$$

$$= \frac{1}{2} \begin{cases} 0 \\ -E_{z_0} |\uparrow\downarrow\rangle \\ +E_{z_1} |\uparrow\downarrow\rangle \\ 0 \end{cases} = \frac{\Delta E_z}{2} |\uparrow\downarrow\rangle . \tag{98}$$

Considering the $|\downarrow\uparrow\rangle$ state:

$$\mathcal{H}_z |\downarrow\uparrow\rangle = \mathcal{H}_z a_{\downarrow,1}^\dagger a_{\uparrow,0}^\dagger |0\rangle$$

$$= \frac{1}{2} \begin{cases} +E_{z_0} a_{\uparrow,0}^\dagger a_{\uparrow,0} a_{\downarrow,1}^\dagger a_{\uparrow,0}^\dagger |0\rangle \\ -E_{z_0} a_{\downarrow,0}^\dagger a_{\downarrow,0} a_{\downarrow,1}^\dagger a_{\uparrow,0}^\dagger |0\rangle \\ +E_{z_1} a_{\uparrow,1}^\dagger a_{\uparrow,1} a_{\downarrow,1}^\dagger a_{\uparrow,0}^\dagger |0\rangle \\ -E_{z_1} a_{\downarrow,1}^\dagger a_{\downarrow,1} a_{\downarrow,1}^\dagger a_{\uparrow,0}^\dagger |0\rangle \end{cases}$$

$$= \frac{1}{2} \begin{cases} E_{z_0} |\downarrow\uparrow\rangle \\ 0 \\ 0 \\ -E_{z_1} |\downarrow\uparrow\rangle \end{cases} = -\frac{\Delta E_z}{2} |\downarrow\uparrow\rangle . \tag{99}$$

Considering the $|\downarrow\downarrow\rangle$ state:

$$\mathcal{H}_z |\downarrow\downarrow\rangle = \mathcal{H}_z a_{\downarrow,1}^\dagger a_{\downarrow,0}^\dagger |0\rangle$$

$$= \frac{1}{2} \begin{cases} +E_{z_0} a_{\uparrow,0}^\dagger a_{\uparrow,0} a_{\downarrow,1}^\dagger a_{\downarrow,0}^\dagger |0\rangle \\ -E_{z_0} a_{\downarrow,0}^\dagger a_{\downarrow,0} a_{\downarrow,1}^\dagger a_{\downarrow,0}^\dagger |0\rangle \\ +E_{z_1} a_{\uparrow,1}^\dagger a_{\uparrow,1} a_{\downarrow,1}^\dagger a_{\downarrow,0}^\dagger |0\rangle \\ -E_{z_1} a_{\downarrow,1}^\dagger a_{\downarrow,1} a_{\downarrow,1}^\dagger a_{\downarrow,0}^\dagger |0\rangle \end{cases}$$

$$= \frac{1}{2}\begin{cases} 0 \\ -E_{z_0} |\downarrow\downarrow\rangle \\ 0 \\ -E_{z_1} |\downarrow\downarrow\rangle \end{cases} = -\overline{E}_z |\downarrow\downarrow\rangle \,. \qquad (100)$$

Considering the $|S(0, 2)\rangle$ state:

$$\mathcal{H}_z |S(0, 2)\rangle = \mathcal{H}_z a^\dagger_{\downarrow,0} a^\dagger_{\uparrow,0} |0\rangle$$

$$= \frac{1}{2}\begin{cases} +E_{z_0} a^\dagger_{\uparrow,0} a_{\uparrow,0} a^\dagger_{\downarrow,0} a^\dagger_{\uparrow,0} |0\rangle \\ -E_{z_0} a^\dagger_{\downarrow,0} a_{\downarrow,0} a^\dagger_{\downarrow,0} a^\dagger_{\uparrow,0} |0\rangle \\ +E_{z_1} a^\dagger_{\uparrow,1} a_{\uparrow,1} a^\dagger_{\downarrow,0} a^\dagger_{\uparrow,0} |0\rangle \\ -E_{z_1} a^\dagger_{\downarrow,1} a_{\downarrow,1} a^\dagger_{\downarrow,0} a^\dagger_{\uparrow,0} |0\rangle \end{cases}$$

$$= \frac{1}{2}\begin{cases} +E_{z_0} |S(0, 2)\rangle \\ -E_{z_0} |S(0, 2)\rangle \\ 0 \\ 0 \end{cases} = 0 \,. \qquad (101)$$

Considering the $|S(2, 0)\rangle$ state:

$$\mathcal{H}_z |S(2, 0)\rangle = \mathcal{H}_z a^\dagger_{\downarrow,1} a^\dagger_{\uparrow,1} |0\rangle$$

$$= \frac{1}{2}\begin{cases} +E_{z_0} a^\dagger_{\uparrow,0} a_{\uparrow,0} a^\dagger_{\downarrow,1} a^\dagger_{\uparrow,1} |0\rangle \\ -E_{z_0} a^\dagger_{\downarrow,0} a_{\downarrow,0} a^\dagger_{\downarrow,1} a^\dagger_{\uparrow,1} |0\rangle \\ +E_{z_1} a^\dagger_{\uparrow,1} a_{\uparrow,1} a^\dagger_{\downarrow,1} a^\dagger_{\uparrow,1} |0\rangle \\ -E_{z_1} a^\dagger_{\downarrow,1} a_{\downarrow,1} a^\dagger_{\downarrow,1} a^\dagger_{\uparrow,1} |0\rangle \end{cases}$$

$$= \frac{1}{2}\begin{cases} 0 \\ 0 \\ +E_{z_1} |S(2, 0)\rangle \\ -E_{z_1} |S(2, 0)\rangle \end{cases} = 0 \,. \qquad (102)$$

Accordingly, the matrix expression of $\mathcal{H}_z$ is

$$\mathcal{H}_z = \begin{bmatrix} \overline{E}_z & 0 & 0 & 0 & 0 & 0 \\ 0 & \frac{\Delta E_z}{2} & 0 & 0 & 0 & 0 \\ 0 & 0 & -\frac{\Delta E_z}{2} & 0 & 0 & 0 \\ 0 & 0 & 0 & -\overline{E}_z & 0 & 0 \\ 0 & 0 & 0 & 0 & 0 & 0 \\ 0 & 0 & 0 & 0 & 0 & 0 \end{bmatrix}. \qquad (103)$$

APPENDIX. SCHRIEFFER-WOLFF TRANSFORMATION

The Schrieffer-Wolff transformation is a unitary transformation used to perturbatively decouple low-energy and high-energy subspaces with the aim of achieving a low-energy effective many-body Hamiltonian [101]. Suppose the complete many-body Hamiltonian can be written as

$$\mathcal{H} = \mathcal{H}_0 + \lambda \mathcal{V} \qquad (104)$$

where $\mathcal{H}_0$ is diagonal, $\mathcal{V}$ acts as a *small perturbation* and λ is an arbitrary constant used to keep track of the order. The Schrieffer-Wolff transformation aims to reduce the small coupling between the high and low energy subspaces,

by moving to a generic rotating frame where the Hamiltonian $\mathcal{H}$ is diagonal up to the n-th order of λ (usually, $n = 1$):

$$\mathcal{H} \longrightarrow \mathcal{H}_{SW} = e^{\lambda S} \mathcal{H} e^{-\lambda S} \,, \qquad (105)$$

where S is the generator of the transformation, and it must be anti-hermitian (for e^S to be unitary) and block-off diagonal [102]. The previous definition can be expanded using the well-known Baker-Campbell-Haussdorf formula (or by replacing the definition of matrix exponential $e^S = \sum_{k=0}^\infty \frac{1}{k!} S^k$):

$$\mathcal{H}_{SW} = \mathcal{H} + \lambda [S, \mathcal{H}] + \frac{\lambda^2}{2!}[S, [S, \mathcal{H}]]$$
$$+ \frac{\lambda^3}{3!}[S, [S, [S, \mathcal{H}]]] + \dots \qquad (106)$$

Replacing the definition of $\mathcal{H}$, one gets

$$\mathcal{H}_{SW} = \mathcal{H}_0 + \lambda \mathcal{V} + \lambda [S, \mathcal{H}_0] + \lambda^2 [S, \mathcal{V}]$$
$$\frac{\lambda^2}{2}[S, [S, \mathcal{H}_0]] + \frac{\lambda^3}{2}[S, [S, \mathcal{V}]] + \dots . \qquad (107)$$

To make the Hamiltonian diagonal to the first order in λ, the generator S must be chosen such that no linear term in λ shows up in $\mathcal{H}_{SW}$ expression. More in detail, assuming that

$$S \,: \, [S, \mathcal{H}_0] = -\mathcal{V} \,, \qquad (108)$$

then to the second order in λ

$$\mathcal{H}_{SW} = \mathcal{H}_0 + \frac{\lambda^2}{2}[S, \mathcal{V}] + \mathcal{O}(\lambda^3) \,. \qquad (109)$$

Considering the six-level Fermi Hubbard Hamiltonian of Equation (7), under the hypothesis that [56], [61]

$$U - \epsilon \gg t_0 \,, \qquad (110)$$

a low-energy subspace $\{|\uparrow\uparrow\rangle, |\uparrow\downarrow\rangle, |\downarrow\uparrow\rangle, |\downarrow\downarrow\rangle\}$ and a high energy subspace $\{|S(0, 2)\rangle, |S(2, 0)\rangle\}$ can be identified. Hence, the Schrieffer-Wolff (SW) transformation can be used to project $\mathcal{H}'_H$ to the physical four-state basis $\{|\uparrow\uparrow\rangle, |\uparrow\downarrow\rangle, |\downarrow\uparrow\rangle, |\downarrow\downarrow\rangle\}$ to the first order. The Fermi Hubbard Hamiltonian can be decomposed as the sum of a diagonal matrix and a *perturbation* off-diagonal matrix

$$\mathcal{H}'_H = \underbrace{\begin{bmatrix} \overline{E}_z & 0 & 0 & 0 & 0 & 0 \\ 0 & \frac{\Delta E_z}{2} & 0 & 0 & 0 & 0 \\ 0 & 0 & -\frac{\Delta E_z}{2} & 0 & 0 & 0 \\ 0 & 0 & 0 & -\overline{E}_z & 0 & 0 \\ 0 & 0 & 0 & 0 & U-\epsilon & 0 \\ 0 & 0 & 0 & 0 & 0 & U+\epsilon \end{bmatrix}}_{\mathcal{H}_0} +$$

$$+ \underbrace{\begin{bmatrix} 0 & 0 & 0 & 0 & 0 & 0 \\ 0 & 0 & 0 & 0 & t_0 & t_0 \\ 0 & 0 & 0 & 0 & -t_0 & -t_0 \\ 0 & 0 & 0 & 0 & 0 & 0 \\ 0 & t_0 & -t_0 & 0 & 0 & 0 \\ 0 & t_0 & -t_0 & 0 & 0 & 0 \end{bmatrix}}_{\mathcal{V}}. \qquad (111)$$

It can be shown that, to second order, S has the following expression [56]:

$$S = \begin{bmatrix} 0 & 0 & 0 \\ 0 & 0 & 0 \\ 0 & 0 & 0 \\ 0 & 0 & 0 \\ 0 & \gamma(+\Delta E_z) & -\gamma(-\Delta E_z) \\ 0 & \sigma(+\Delta E_z) & -\sigma(-\Delta E_z) \end{bmatrix}$$

$$\begin{matrix} 0 & 0 & 0 \\ 0 & -\gamma(+\Delta E_z) & -\sigma(+\Delta E_z) \\ 0 & \gamma(-\Delta E_z) & \sigma(-\Delta E_z) \\ 0 & 0 & 0 \\ 0 & 0 & 0 \\ 0 & 0 & 0 \end{matrix} \Bigg], \quad (112)$$

where

$$\gamma(\Delta E_z) = \frac{t_0}{U - \epsilon - \frac{\Delta E_z}{2}}$$

$$\sigma(\Delta E_z) = \frac{t_0}{U + \epsilon - \frac{\Delta E_z}{2}}, \quad (113)$$

and it is trivial to see that $[S, \mathcal{H}_0] = -\mathcal{V}$. The next step is the computation of the commutator $[S, \mathcal{V}]$, as reported in Equation (114), where

$$\alpha(\Delta E_z) \triangleq \frac{t_0^2}{U - \epsilon - \frac{\Delta E_z}{2}} + \frac{t_0^2}{U + \epsilon - \frac{\Delta E_z}{2}}$$

$$= t(\gamma(+\Delta E_Z) + \sigma(\Delta E_Z)),$$

$$\beta(\Delta E_z) \triangleq \frac{\alpha(\Delta E_z) + \alpha(-\Delta E_z)}{2}. \quad (115)$$

Therefore, the Schrieffer-Wolff Hamiltonian ($\lambda = 1$) to the second order can be written as reported in Equation (116). It shall be noted that, thanks to the Schrieffer-Wolff transformation, the Hamiltonian is now block diagonal and there are no terms that couple the $(1, 1)$ subspace with the $(0, 2)$ and $(2, 0)$ subspaces. Therefore, an effective Hamiltonian can be retrieved projecting Equation (116) to the physical four-state basis $\{|\uparrow\uparrow\rangle, |\uparrow\downarrow\rangle, |\downarrow\uparrow\rangle, |\downarrow\downarrow\rangle\}$:

$$\mathcal{H}'_{SW} = \begin{bmatrix} \overline{E}_z & 0 \\ 0 & \frac{\Delta E_z}{2} - \alpha(\Delta E_z) \\ 0 & \beta(\Delta E_z) \\ 0 & 0 \end{bmatrix}$$

$$\begin{matrix} 0 & 0 \\ \beta(\Delta E_z) & 0 \\ -\frac{\Delta E_z}{2} - \alpha(-\Delta E_z) & 0 \\ 0 & -\overline{E}_z \end{matrix} \Bigg]. \quad (117)$$

REFERENCES

[1] G. A. Cirillo, "Engineering quantum computing technologies: From compact modelling to applications," Ph.D. thesis, Doctorate Program Elect., Electron. Commun. Eng., Politecnico di Torino, Turin, Italy, 2022.

$$[S, \mathcal{V}] = 2 \begin{bmatrix} 0 & 0 & 0 & 0 & 0 & 0 \\ 0 & -\alpha(+\Delta E_z) & \beta & 0 & 0 & 0 \\ 0 & \beta & -\alpha(-\Delta E_z) & 0 & 0 & 0 \\ 0 & 0 & 0 & 0 & 0 & 0 \\ 0 & 0 & 0 & 0 & t(\gamma(+\Delta E_Z) + \gamma(-\Delta E_Z)) & \beta \\ 0 & 0 & 0 & 0 & \beta & t(\sigma(+\Delta E_Z) + \sigma(-\Delta E_Z)) \end{bmatrix} \quad (114)$$

$$\mathcal{H}'_{SW} = \mathcal{H}_0 + \frac{1}{2}[S, \mathcal{V}]$$

$$= \begin{bmatrix} E_z & 0 & 0 & 0 \\ 0 & \frac{\Delta E_z}{2} - \alpha(\Delta E_z) & \beta & 0 \\ 0 & \beta & -\frac{\Delta E_z}{2} - \alpha(-\Delta E_z) & 0 \\ 0 & 0 & 0 & -E_z \\ 0 & 0 & 0 & 0 \\ 0 & 0 & 0 & 0 \end{bmatrix}$$

$$\begin{matrix} 0 & 0 \\ 0 & 0 \\ 0 & 0 \\ 0 & 0 \\ U - \epsilon + t(\gamma(\Delta E_Z) + \gamma(-\Delta E_Z)) & \beta \\ \beta & U + \epsilon + t(\sigma(\Delta E_Z) + \sigma(-\Delta E_Z)) \end{matrix} \Bigg] \quad (116)$$

[2] E. Zahedinejad and A. Zaribafiyan, "Combinatorial optimization on gate model quantum computers: A survey," 2017, *arXiv:1708.05294*.

[3] F. Yan, A. M. Iliyasu, and S. E. Venegas-Andraca, "A survey of quantum image representations," *Quantum Inf. Process.*, vol. 15, no. 1, pp. 1–35, Dec. 2015, doi: 10.1007/s11128-015-1195-6.

[4] N. Mishra et al., "Quantum machine learning: A review and current status," in *Data Management, Analytics and Innovation*. Singapore: Springer, 2021, pp. 101–145, doi: 10.1007/978-981-15-5619-7_8.

[5] Y. Cao, J. Romero, J. P. Olson, M. Degroote, P. D. Johnson, M. Kieferová, I. D. Kivlichan, T. Menke, B. Peropadre, N. P. D. Sawaya, S. Sim, L. Veis, and A. Aspuru-Guzik, "Quantum chemistry in the age of quantum computing," *Chem. Rev.*, vol. 119, no. 19, pp. 10856–10915, Aug. 2019, doi: 10.1021/acs.chemrev.8b00803.

[6] P. Krantz, M. Kjaergaard, F. Yan, T. P. Orlando, S. Gustavsson, and W. D. Oliver, "A quantum engineer's guide to superconducting qubits," *Appl. Phys. Rev.*, vol. 6, no. 2, Jun. 2019, Art. no. 021318, doi: 10.1063/1.5089550.

[7] C. D. Bruzewicz, J. Chiaverini, R. McConnell, and J. M. Sage, "Trapped-ion quantum computing: Progress and challenges," *Appl. Phys. Rev.*, vol. 6, no. 2, Jun. 2019, Art. no. 021314, doi: 10.1063/1.5088164.

[8] X. Zhang, H.-O. Li, G. Cao, M. Xiao, G.-C. Guo, and G.-P. Guo, "Semiconductor quantum computation," *Nat. Sci. Rev.*, vol. 6, no. 1, pp. 32–54, Jan. 2019, doi: 10.1093/nsr/nwy153.

[9] A. Gaita-Ariño, F. Luis, S. Hill, and E. Coronado, "Molecular spins for quantum computation," *Nature Chem.*, vol. 11, no. 4, pp. 301–309, Apr. 2019, doi: 10.1038/s41557-019-0232-y.

[10] L. M. K. Vandersypen and I. L. Chuang, "NMR techniques for quantum control and computation," *Rev. Mod. Phys.*, vol. 76, no. 4, pp. 1037–1069, Jan. 2005, doi: 10.1103/RevModPhys.76.1037.

[11] (2021). *IBM Quantum*. [Online]. Available: https://quantum-computing.ibm.com/

[12] *Quantinuum*. Accessed: Mar. 10, 2023. [Online]. Available: https://www.quantinuum.com/

[13] QuTech. (2018). *Quantum Inspire Home*. [Online]. Available: https://www.quantum-inspire.com/

[14] J. Preskill, "Quantum computing in the NISQ era and beyond," *Quantum*, vol. 2, p. 79, Aug. 2018, doi: 10.22331/q-2018-08-06-79.

[15] J. R. Johansson, P. D. Nation, and F. Nori, "QuTiP: An open-source Python framework for the dynamics of open quantum systems," *Comput. Phys. Commun.*, vol. 183, no. 8, pp. 1760–1772, Aug. 2012, doi: 10.1016/j.cpc.2012.02.021.

[16] F. Beaudoin, P. Philippopoulos, C. Zhou, I. Kriekouki, M. Pioro-Ladrière, H. Guo, and P. Galy, "Robust technology computer-aided design of gated quantum dots at cryogenic temperature," *Appl. Phys. Lett.*, vol. 120, no. 26, Jun. 2022, Art. no. 264001, doi: 10.1063/5.0097202.

[17] S. Birner, T. Zibold, T. Andlauer, T. Kubis, M. Sabathil, A. Trellakis, and P. Vogl, "Nextnano: General purpose 3-D simulations," *IEEE Trans. Electron Devices*, vol. 54, no. 9, pp. 2137–2142, Sep. 2007, doi: 10.1109/TED.2007.902871.

[18] H. Abraham et al., "Qiskit: An open-source framework for quantum computing," IBM, Tech. Rep., 2019, doi: 10.5281/zenodo.2562110.

[19] G. A. Cirillo, G. Turvani, M. Simoni, and M. Graziano, "Advances in molecular quantum computing: From technological modeling to circuit design," in *Proc. IEEE Comput. Soc. Annu. Symp. VLSI (ISVLSI)*, Jul. 2020, pp. 132–137, doi: 10.1109/ISVLSI49217.2020.00033.

[20] M. Simoni, G. A. Cirillo, G. Turvani, M. Graziano, and M. Zamboni, "Towards compact modeling of noisy quantum computers: A molecular-spin-qubit case of study," *ACM J. Emerg. Technol. Comput. Syst.*, vol. 18, no. 1, pp. 1–26, Sep. 2021, doi: 10.1145/3474223.

[21] L. Petit, H. G. J. Eenink, M. Russ, W. I. L. Lawrie, N. W. Hendrickx, S. G. J. Philips, J. S. Clarke, L. M. K. Vandersypen, and M. Veldhorst, "Universal quantum logic in hot silicon qubits," *Nature*, vol. 580, no. 7803, pp. 355–359, Apr. 2020, doi: 10.1038/s41586-020-2170-7.

[22] S. G. J. Philips, M. T. Mądzik, S. V. Amitonov, S. L. de Snoo, M. Russ, N. Kalhor, C. Volk, W. I. L. Lawrie, D. Brousse, L. Tryputen, B. P. Wuetz, A. Sammak, M. Veldhorst, G. Scappucci, and L. M. K. Vandersypen, "Universal control of a six-qubit quantum processor in silicon," *Nature*, vol. 609, no. 7929, pp. 919–924, Sep. 2022, doi: 10.1038/s41586-022-05117-x.

[23] N. W. Hendrickx, W. I. L. Lawrie, M. Russ, F. van Riggelen, S. L. de Snoo, R. N. Schouten, A. Sammak, G. Scappucci, and M. Veldhorst, "A four-qubit germanium quantum processor," *Nature*, vol. 591, no. 7851, pp. 580–585, Mar. 2021, doi: 10.1038/s41586-021-03332-6.

[24] F. Ansaloni, H. Bohuslavskyi, F. Fedele, T. Rasmussen, B. Brovang, F. Berritta, A. Heskes, J. Li, L. Hutin, B. Venitucci, B. Bertrand, M. Vinet, Y.-M. Niquet, A. Chatterjee, and F. Kuemmeth, "Gate reflectometry in dense quantum dot arrays," *New J. Phys.*, vol. 25, no. 3, Mar. 2023, Art. no. 033023, doi: 10.1088/1367-2630/acc126.

[25] M. De Michielis, E. Ferraro, E. Prati, L. Hutin, B. Bertrand, E. Charbon, D. J. Ibberson, and M. Fernando Gonzalez-Zalba, "Silicon spin qubits from laboratory to industry," *J. Phys. D, Appl. Phys.*, vol. 56, no. 36, Jun. 2023, Art. no. 363001, doi: 10.1088/1361-6463/acd8c7.

[26] J. J. Pla, K. Y. Tan, J. P. Dehollain, W. H. Lim, J. J. L. Morton, F. A. Zwanenburg, D. N. Jamieson, A. S. Dzurak, and A. Morello, "High-fidelity readout and control of a nuclear spin qubit in silicon," *Nature*, vol. 496, no. 7445, pp. 334–338, Apr. 2013, doi: 10.1038/nature12011.

[27] A. Morello, J. J. Pla, F. A. Zwanenburg, K. W. Chan, K. Y. Tan, H. Huebl, M. Möttönen, C. D. Nugroho, C. Yang, J. A. van Donkelaar, A. D. C. Alves, D. N. Jamieson, C. C. Escott, L. C. L. Hollenberg, R. G. Clark, and A. S. Dzurak, "Single-shot readout of an electron spin in silicon," *Nature*, vol. 467, no. 7316, pp. 687–691, Oct. 2010, doi: 10.1038/nature09392.

[28] S. Asaad, V. Mourik, B. Joecker, M. A. I. Johnson, A. D. Baczewski, H. R. Firgau, M. T. Mądzik, V. Schmitt, J. J. Pla, F. E. Hudson, K. M. Itoh, J. C. McCallum, A. S. Dzurak, A. Laucht, and A. Morello, "Coherent electrical control of a single high-spin nucleus in silicon," *Nature*, vol. 579, no. 7798, pp. 205–209, Mar. 2020, doi: 10.1038/s41586-020-2057-7.

[29] T. H. Taminiau, J. Cramer, T. van der Sar, V. V. Dobrovitski, and R. Hanson, "Universal control and error correction in multi-qubit spin registers in diamond," *Nature Nanotechnol.*, vol. 9, no. 3, pp. 171–176, Mar. 2014, doi: 10.1038/nnano.2014.2.

[30] L. M. Vandersypen and M. A. Eriksson, "Quantum computing with semiconductor spins," *Phys. Today*, vol. 72, no. 8, pp. 38–45, 2019, doi: 10.1063/PT.3.4270.

[31] L. M. K. Vandersypen, H. Bluhm, J. S. Clarke, A. S. Dzurak, R. Ishihara, A. Morello, D. J. Reilly, L. R. Schreiber, and M. Veldhorst, "Interfacing spin qubits in quantum dots and donors—Hot, dense, and coherent," *NPJ Quantum Inf.*, vol. 3, no. 1, p. 34, Sep. 2017, doi: 10.1038/s41534-017-0038-y.

[32] R. Li, L. Petit, D. P. Franke, J. P. Dehollain, J. Helsen, M. Steudtner, N. K. Thomas, Z. R. Yoscovits, K. J. Singh, S. Wehner, L. M. K. Vandersypen, J. S. Clarke, and M. Veldhorst, "A crossbar network for silicon quantum dot qubits," *Sci. Adv.*, vol. 4, no. 7, Jul. 2018, Art. no. eaar3960, doi: 10.1126/sciadv.aar3960.

[33] J. M. Taylor, H.-A. Engel, W. Dür, A. Yacoby, C. M. Marcus, P. Zoller, and M. D. Lukin, "Fault-tolerant architecture for quantum computation using electrically controlled semiconductor spins," *Nature Phys.*, vol. 1, no. 3, pp. 177–183, Dec. 2005, doi: 10.1038/nphys174.

[34] M. Veldhorst, H. G. J. Eenink, C. H. Yang, and A. S. Dzurak, "Silicon CMOS architecture for a spin-based quantum computer," *Nature Commun.*, vol. 8, no. 1, pp. 1–8, Dec. 2017, doi: 10.1038/s41467-017-01905-6.

[35] X. Zhang, H.-O. Li, K. Wang, G. Cao, M. Xiao, and G.-P. Guo, "Qubits based on semiconductor quantum dots," *Chin. Phys. B*, vol. 27, no. 2, Feb. 2018, Art. no. 020305, doi: 10.1088/1674-1056/27/2/020305.

[36] M. Veldhorst, J. C. C. Hwang, C. H. Yang, A. W. Leenstra, B. de Ronde, J. P. Dehollain, J. T. Muhonen, F. E. Hudson, K. M. Itoh, A. Morello, and A. S. Dzurak, "An addressable quantum dot qubit with fault-tolerant control-fidelity," *Nature Nanotechnol.*, vol. 9, no. 12, pp. 981–985, Dec. 2014, doi: 10.1038/nnano.2014.216.

[37] D. Loss and D. P. DiVincenzo, "Quantum computation with quantum dots," *Phys. Rev. A, Gen. Phys.*, vol. 57, no. 1, pp. 120–126, Jan. 1998, doi: 10.1103/PhysRevA.57.120.

[38] J. Gorman, D. G. Hasko, and D. A. Williams, "Charge-qubit operation of an isolated double quantum dot," *Phys. Rev. Lett.*, vol. 95, no. 9, Aug. 2005, Art. no. 090502, doi: 10.1103/PhysRevLett.95.090502.

[39] X. Wu, D. R. Ward, J. R. Prance, D. Kim, J. K. Gamble, R. T. Mohr, Z. Shi, D. E. Savage, M. G. Lagally, M. Friesen, S. N. Coppersmith, and M. A. Eriksson, "Two-axis control of a singlet–triplet qubit with an integrated micromagnet," *Proc. Nat. Acad. Sci. USA*, vol. 111, no. 33, pp. 11938–11942, Aug. 2014, doi: 10.1073/pnas.1412230111.

[40] K. W. Chan, W. Huang, C. H. Yang, J. C. C. Hwang, B. Hensen, T. Tanttu, F. E. Hudson, K. M. Itoh, A. Laucht, A. Morello, and A. S. Dzurak, "Assessment of a silicon quantum dot spin qubit environment via noise spectroscopy," *Phys. Rev. Appl.*, vol. 10, no. 4, Oct. 2018, Art. no. 044017, doi: 10.1103/PhysRevApplied.10.044017.

[41] E. Kawakami, P. Scarlino, D. R. Ward, F. R. Braakman, D. E. Savage, M. G. Lagally, M. Friesen, S. N. Coppersmith, M. A. Eriksson, and L. M. K. Vandersypen, "Electrical control of a long-lived spin qubit in a Si/SiGe quantum dot," *Nature Nanotechnol.*, vol. 9, no. 9, pp. 666–670, Sep. 2014, doi: 10.1038/nnano.2014.153.

[42] F. A. Zwanenburg, A. S. Dzurak, A. Morello, M. Y. Simmons, L. C. L. Hollenberg, G. Klimeck, S. Rogge, S. N. Coppersmith, and M. A. Eriksson, "Silicon quantum electronics," *Rev. Mod. Phys.*, vol. 85, no. 3, pp. 961–1019, Jul. 2013, doi: 10.1103/RevModPhys.85.961.

[43] R. Hanson, L. P. Kouwenhoven, J. R. Petta, S. Tarucha, and L. M. K. Vandersypen, "Spins in few-electron quantum dots," *Rev. Mod. Phys.*, vol. 79, no. 4, pp. 1217–1265, Oct. 2007, doi: 10.1103/RevModPhys.79.1217.

[44] F. Neese, "The ORCA program system," *WIREs Comput. Mol. Sci.*, vol. 2, pp. 73–78, Jan. 2012. [Online]. Available: https://onlinelibrary.wiley.com/doi/10.1002/wcms.81

[45] F. Neese, "Software update: The ORCA program system, version 4.0," *WIREs Comput. Mol. Sci.*, vol. 8, Jan. 2018, Art. no. e1327. [Online]. Available: https://onlinelibrary.wiley.com/doi/10.1002/wcms.1327

[46] S. Smidstrup et al., "QuantumATK: An integrated platform of electronic and atomic-scale modelling tools," *J. Phys., Condens. Matter*, vol. 32, no. 1, Jan. 2020, Art. no. 015901, doi: 10.1088/1361-648X/ab4007.

[47] A. W. Cross, L. S. Bishop, J. A. Smolin, and J. M. Gambetta, "Open quantum assembly language," 2017, arXiv:1707.03429.

[48] M. F. Gonzalez-Zalba, S. de Franceschi, E. Charbon, T. Meunier, M. Vinet, and A. S. Dzurak, "Scaling silicon-based quantum computing using CMOS technology," *Nature Electron.*, vol. 4, no. 12, pp. 872–884, Dec. 2021, doi: 10.1038/s41928-021-00681-y.

[49] F. A. Mohiyaddin, G. Simion, N. I. D. Stuyck, R. Li, F. Ciubotaru, G. Eneman, F. M. Bufler, S. Kubicek, J. Jussot, B. Chan, T. Ivanov, A. Spessot, P. Matagne, J. Lee, B. Govoreanu, and I. P. Raduimec, "Multiphysics simulation & design of silicon quantum dot qubit devices," in *IEDM Tech. Dig.*, San Francisco, CA, USA, Dec. 2019, pp. 39.5.1–39.5.4, doi: 10.1109/IEDM19573.2019.8993541.

[50] M. Avitabile, G. A. Cirillo, M. Simoni, G. Turvani, and M. Graziano, "Development of a multi-technology, template-based quantum circuits compilation toolchain," *Quantum Inf. Process.*, vol. 21, no. 11, p. 379, Nov. 2022, doi: 10.1007/s11128-022-03649-9.

[51] M. A. Nielsen and I. L. Chuang, *Quantum Computation and Quantum Information*. Cambridge, U.K.: Cambridge Univ. Press, 2010.

[52] C. Cohen-Tannoudji, B. Diu, and F. Laloe, *Quantum Mechanics*, vol. 1. Weinheim, Germany: Wiley, 2020.

[53] J. M. Brown, R. J. Buenker, A. Carrington, C. Di Lauro, R. N. Dixon, R. W. Field, J. T. Hougen, W. Hüttner, K. Kuchitsu, M. Mehring, A. J. Merer, T. A. Miller, M. Quack, D. A. Ramsay, L. Veseth, and R. N. Zare, "Remarks on the signs of g factors in atomic and molecular Zeeman spectroscopy," *Mol. Phys.*, vol. 98, no. 20, pp. 1597–1601, Oct. 2000, doi: 10.1080/00268970009483366.

[54] G. Burkard, T. D. Ladd, J. M. Nichol, A. Pan, and J. R. Petta, "Semiconductor spin qubits," 2021, arXiv:2112.08863.

[55] J. Cavanagh, W. J. Fairbrother, A. G. Palmer, III, N. J. Skelton, and M. Rance, *Protein NMR Spectroscopy: Principles and Practice*, 2nd ed. London, U.K.: Elsevier, 2007.

[56] T. Meunier, V. E. Calado, and L. M. K. Vandersypen, "Efficient controlled-phase gate for single-spin qubits in quantum dots," *Phys. Rev. B, Condens. Matter*, vol. 83, no. 12, Mar. 2011, Art. no. 121403. [Online]. Available: https://link.aps.org/doi/10.1103/PhysRevB.83.121403

[57] M. Veldhorst, C. H. Yang, J. C. C. Hwang, W. Huang, J. P. Dehollain, J. T. Muhonen, S. Simmons, A. Laucht, F. E. Hudson, K. M. Itoh, A. Morello, and A. S. Dzurak, "A two-qubit logic gate in silicon," *Nature*, vol. 526, no. 7573, pp. 410–414, Oct. 2015, doi: 10.1038/nature15263.

[58] A. Jamalzada, "Simulating dynamics of two electron spins in a Si-based double quantum dot," Ph.D. thesis, Faculty Sci., Leiden Univ., Leiden, The Netherlands, 2019.

[59] X. Hu and S. D. Sarma, "Hilbert-space structure of a solid-state quantum computer: Two-electron states of a double-quantum-dot artificial molecule," *Phys. Rev. A, Gen. Phys.*, vol. 61, no. 6, May 2000, Art. no. 062301, doi: 10.1103/PhysRevA.61.062301.

[60] D. Kotekar-Patil, A. Corna, R. Maurand, A. Crippa, A. Orlov, S. Barraud, L. Hutin, M. Vinet, X. Jehl, S. De Franceschi, and M. Sanquer, "Pauli spin blockade in CMOS double quantum dot devices," *Phys. Status Solidi B*, vol. 254, no. 3, Mar. 2017, Art. no. 1600581, doi: 10.1002/pssb.201600581.

[61] C.-H. Huang, C.-H. Yang, C.-C. Chen, A. S. Dzurak, and H.-S. Goan, "High-fidelity and robust two-qubit gates for quantum-dot spin qubits in silicon," *Phys. Rev. A, Gen. Phys.*, vol. 99, no. 4, Apr. 2019, Art. no. 042310, doi: 10.1103/physreva.99.042310.

[62] M. Nakahara, S. Kanemitsu, M. Salomaa, and S. Takagi, *Physical Realizations of Quantum Computing: Are the Divincenzo Criteria Fulfilled in 2004?*, 1st ed. Singapore: World Scientific, 2006.

[63] T. Last, N. Samkharadze, P. Eendebak, R. Versluis, X. Xue, A. Sammak, D. Brousse, K. Loh, H. Polinder, G. Scappucci, M. Veldhorst, L. Vandersypen, K. Maturová, J. Veltin, and G. Alberts, "Quantum inspire: QuTech's platform for co-development and collaboration in quantum computing," *Proc. SPIE*, vol. 11324, pp. 49–59, Mar. 2020, doi: 10.1117/12.2551853.

[64] H. G. J. Eenink, L. Petit, W. I. L. Lawrie, J. S. Clarke, L. M. K. Vandersypen, and M. Veldhorst, "Tunable coupling and isolation of single electrons in silicon metal-oxide-semiconductor quantum dots," *Nano Lett.*, vol. 19, no. 12, pp. 8653–8657, Dec. 2019, doi: 10.1021/acs.nanolett.9b03254.

[65] C. Geuzaine and J.-F. Remacle, "GMSH: A 3-D finite element mesh generator with built-in pre- and post-processing facilities," *Int. J. Numer. Methods Eng.*, vol. 79, no. 11, pp. 1309–1331, Sep. 2009, doi: 10.1002/nme.2579.

[66] J. Fischer, M. Trif, W. A. Coish, and D. Loss, "Spin interactions, relaxation and decoherence in quantum dots," *Solid State Commun.*, vol. 149, nos. 35–36, pp. 1443–1450, Sep. 2009, doi: 10.1016/j.ssc.2009.04.033.

[67] X. Gao, E. Nielsen, R. P. Müller, R. W. Young, A. G. Salinger, N. C. Bishop, M. P. Lilly, and M. S. Carroll, "Quantum computer aided design simulation and optimization of semiconductor quantum dots," *J. Appl. Phys.*, vol. 114, no. 16, Oct. 2013, Art. no. 164302, doi: 10.1063/1.4825209.

[68] R. Winkler, *Spin-orbit Coupling Effects in Two-Dimensional Electron and Hole Systems* (Springer Tracts in Modern Physics), vol. 191. Berlin, Germany: Springer, 2003, doi: 10.1007/b13586.

[69] M. F. Gyure, A. A. Kiselev, R. S. Ross, R. Rahman, and C. G. Van de Walle, "Materials and device simulations for silicon qubit design and optimization," *MRS Bull.*, vol. 46, no. 7, pp. 634–641, Jul. 2021, doi: 10.1557/s43577-021-00140-1.

[70] E. Nielsen, R. Rahman, and R. P. Müller, "A many-electron tight binding method for the analysis of quantum dot systems," *J. Appl. Phys.*, vol. 112, no. 11, Dec. 2012, Art. no. 114304, doi: 10.1063/1.4759256.

[71] F. A. Mohiyaddin, G. Simion, N. I. D. Stuyck, R. Li, A. Elsayed, M. Shehata, S. Kubicek, C. Godfrin, B. T. Chan, J. Jussot, F. C. Ubotaru, S. Brebels, F. M. Bufler, G. Eneman, P. Weckx, P. Matagne, A. Spessot, B. Govoreanu, and I. P. Radu, "TCAD-assisted multiphysics modeling & simulation for accelerating silicon quantum dot qubit design," in *Proc. Int. Conf. Simulation Semiconductor Processes Devices (SISPAD)*, Sep. 2020, pp. 253–256, doi: 10.23919/SISPAD49475.2020.9241612.

[72] B. Venitucci, J. Li, L. Bourdet, and Y.-M. Niquet, "Modeling silicon CMOS devices for quantum computing," in *Proc. Int. Conf. Simulation Semiconductor Processes Devices (SISPAD)*, Sep. 2019, pp. 1–4, doi: 10.1109/SISPAD.2019.8870477.

[73] L.-X. Zhang, D. V. Melnikov, and J.-P. Leburton, "Non-monotonic variation of the exchange energy in double elliptic quantum dots," *J. Phys., Condens. Matter*, vol. 21, no. 9, Jan. 2009, Art. no. 095502, doi: 10.1088/0953-8984/21/9/095502.

[74] W. I. L. Lawrie, H. G. J. Eenink, N. W. Hendrickx, J. M. Boter, L. Petit, S. V. Amitonov, M. Lodari, B. Paquelet Wuetz, C. Volk, S. G. J. Philips, G. Droulers, N. Kalhor, F. van Riggelen, D. Brousse, A. Sammak, L. M. K. Vandersypen, G. Scappucci, and M. Veldhorst, "Quantum dot arrays in silicon and germanium," *Appl. Phys. Lett.*, vol. 116, no. 8, Feb. 2020, Art. no. 080501, doi: 10.1063/5.0002013.

[75] F. Stern and W. E. Howard, "Properties of semiconductor surface inversion layers in the electric quantum limit," *Phys. Rev.*, vol. 163, no. 3, pp. 816–835, Nov. 1967, doi: 10.1103/PhysRev.163.816.

[76] F. F. Fang and W. E. Howard, "Negative field-effect mobility on (100) Si surfaces," *Phys. Rev. Lett.*, vol. 16, no. 18, pp. 797–799, May 1966, doi: 10.1103/PhysRevLett.16.797.

[77] S. Goswami, K. A. Slinker, M. Friesen, L. M. McGuire, J. L. Truitt, C. Tahan, L. J. Klein, J. O. Chu, P. M. Mooney, D. W. van der Weide, R. Joynt, S. N. Coppersmith, and M. A. Eriksson, "Controllable valley splitting in silicon quantum devices," *Nature Phys.*, vol. 3, no. 1, pp. 41–45, Jan. 2007, doi: 10.1038/nphys475.

[78] T. Ando, A. B. Fowler, and F. Stern, "Electronic properties of two-dimensional systems," *Rev. Mod. Phys.*, vol. 54, no. 2, pp. 437–672, Apr. 1982, doi: 10.1103/RevModPhys.54.437.

[79] T. B. Boykin, G. Klimeck, M. A. Eriksson, M. Friesen, S. N. Coppersmith, P. von Allmen, F. Oyafuso, and S. Lee, "Valley splitting in strained silicon quantum wells," *Appl. Phys. Lett.*, vol. 84, no. 1, pp. 115–117, Jan. 2004, doi: 10.1063/1.1637718.

[80] H. B. Michaelson, "The work function of the elements and its periodicity," *J. Appl. Phys.*, vol. 48, no. 11, pp. 4729–4733, Nov. 1977, doi: 10.1063/1.323539.

[81] P. W. Deelman, L. F. Edge, and C. A. Jackson, "Metamorphic materials for quantum computing," *MRS Bull.*, vol. 41, no. 3, pp. 224–230, Mar. 2016, doi: 10.1557/mrs.2016.28.

[82] T. Wu and J. Guo, "A multiscale simulation approach for germanium-hole-based quantum processor," *IEEE Trans. Comput.-Aided Design Integr. Circuits Syst.*, vol. 42, no. 1, pp. 257–265, Jan. 2023, doi: 10.1109/TCAD.2022.3166107.

[83] A. Fuhrer, "Phase coherence, orbital and spin states in quantum rings," Doctoral thesis, Natural Sci., ETH Zürich, Zürich, Switzerland, 2003, doi: 10.3929/ethz-a-004593507.

[84] Nanoacademic Technologies. *QTCAD Manual*. Accessed: May 5, 2023. [Online]. Available: https://docs.nanoacademic.com/qtcad/introduction/

[85] Nanoacademic Technologies. *QTCAD API*. Accessed: May 5, 2023. [Online]. Available: https://docs.nanoacademic.com/qtcad/API_reference/qtcad/

[86] S. Kullback and R. A. Leibler, "On information and sufficiency," *Ann. Math. Statist.*, vol. 22, no. 1, pp. 79–86, Mar. 1951, doi: 10.1214/aoms/1177729694.

[87] S. Nishio, Y. Pan, T. Satoh, H. Amano, and R. V. Meter, "Extracting success from IBM's 20-qubit machines using error-aware compilation," *ACM J. Emerg. Technol. Comput. Syst.*, vol. 16, no. 3, pp. 1–25, Jul. 2020, doi: 10.1145/3386162.

[88] H. G. J. Eenink, "Hot qubits in silicon for quantum computation," Doctoral thesis, QuTech, Delft Univ. Technol., Delft, The Netherlands, 2021, doi: 10.4233/uuid:a4e87a46-cdd9-459b-a073-c5b31ca4a73d.

[89] L. Petit, M. Russ, G. H. G. J. Eenink, W. I. L. Lawrie, J. S. Clarke, L. M. K. Vandersypen, and M. Veldhorst, "Design and integration of single-qubit rotations and two-qubit gates in silicon above one Kelvin," *Commun. Mater.*, vol. 3, no. 1, pp. 1–7, Nov. 2022, doi: 10.1038/s43246-022-00304-9.

[90] A. Elsayed, M. Shehata, C. Godfrin, S. Kubicek, S. Massar, Y. Canvel, J. Jussot, G. Simion, M. Mongillo, D. Wan, B. Govoreanu, I. P. Radu, R. Li, P. Van Dorpe, and K. De Greve, "Low charge noise quantum dots with industrial CMOS manufacturing," Dec. 2022, *arXiv:2212.06464*.

[91] M. T. Mądzik, A. Laucht, F. E. Hudson, A. M. Jakob, B. C. Johnson, D. N. Jamieson, K. M. Itoh, A. S. Dzurak, and A. Morello, "Conditional quantum operation of two exchange-coupled single-donor spin qubits in a MOS-compatible silicon device," *Nature Commun.*, vol. 12, no. 1, p. 181, Jan. 2021, doi: 10.1038/s41467-020-20424-5.

[92] G. Scappucci, C. Kloeffel, F. A. Zwanenburg, D. Loss, M. Myronov, J.-J. Zhang, S. De Franceschi, G. Katsaros, and M. Veldhorst, "The germanium quantum information route," *Nature Rev. Mater.*, vol. 6, no. 10, pp. 926–943, Dec. 2020, doi: 10.1038/s41578-020-00262-z.

[93] F. Schwabl, *Quantum Mechanics*, 4th ed. Berlin, Germany: Springer, 2007.

[94] R. Balian, *From Microphysics to Macrophysics: Methods and Applications of Statistical Physics*, 1st ed. New York, NY, USA: Springer, 2007.

[95] M. Nakahara and T. Ohmi, *Quantum Computing: From Linear Algebra to Physical Realizations*, 1st ed. Boca Raton, FL, USA: CRC Press, 2008.

[96] M. Levitt, *Spin Dynamics: Basics of Nuclear Magnetic Resonance*. Chichester, U.K.: Wiley, 2008.

[97] X. Wang, S. Yang, and S. D. Sarma, "Quantum theory of the charge-stability diagram of semiconductor double-quantum-dot systems," *Phys. Rev. B, Condens. Matter*, vol. 84, no. 11, Sep. 2011, Art. no. 115301, doi: 10.1103/PhysRevB.84.115301.

[98] S. Yang, X. Wang, and S. D. Sarma, "Generic Hubbard model description of semiconductor quantum-dot spin qubits," *Phys. Rev. B, Condens. Matter*, vol. 83, no. 16, Apr. 2011, Art. no. 161301, doi: 10.1103/PhysRevB.83.161301.

[99] S. Das Sarma, X. Wang, and S. Yang, "Hubbard model description of silicon spin qubits: Charge stability diagram and tunnel coupling in Si double quantum dots," *Phys. Rev. B, Condens. Matter*, vol. 83, no. 23, Jun. 2011, Art. no. 235314, doi: 10.1103/PhysRevB.83.235314.

[100] S. A. Jafari, "Introduction to Hubbard model and exact diagonalization," 2008, *arXiv:0807.4878*.

[101] J. R. Schrieffer and P. A. Wolff, "Relation between the Anderson and Kondo Hamiltonians," *Phys. Rev.*, vol. 149, pp. 491–492, Sep. 1966, doi: 10.1103/PhysRev.149.491.

[102] T. H. Kyaw, "Towards a scalable quantum computing platform in the ultrastrong coupling regime," Ph.D. thesis, Centre Quantum Technol., Nat. Univ. Singapore, Singapore, 2019.

DAVIDE COSTA received the M.Sc. degree in electronic engineering from Politecnico di Torino, in 2022. He is currently pursuing the Ph.D. degree in physics with TU Delft. His research activities include quantum materials characterization and modeling and simulation of quantum devices.

MARIO SIMONI (Member, IEEE) received the M.Sc. degree in micro and nanoelectronic engineering from Politecnico di Torino, in 2020, where he is currently pursuing the Ph.D. degree in electrical, electronics, and telecommunication engineering. He was a Visiting Researcher with the MESA+ Institute for Nanotechnology, University of Twente, in 2023. His research activities include modeling, simulation, design, and characterization of solid-state quantum computers.

GIANLUCA PICCININI received the M.Sc. and Ph.D. degrees in electronics engineering from Politecnico di Torino, Turin, Italy, in 1986 and 1990, respectively. Since 2006, he has been a Full Professor with the Department of Electronics, Politecnico di Torino. His current interests include modeling molecular field-coupled nanocomputing systems and single-molecule sensors, fabrication techniques of electrodes for molecular devices, functionalization of nanogap for sensing, and modeling and application of molecular transistors. He focuses on electrical transport modeling, especially in molecular and nanostructures; in the cross-implications between the physical characteristics of materials and system-level characteristics.

MARIAGRAZIA GRAZIANO received the M.Sc. and Ph.D. degrees in electronics engineering from Politecnico di Torino, Turin, Italy, in 1997 and 2001, respectively. Since 2008, she has been an Adjunct Faculty Member with the University of Illinois at Chicago (UFL), Chicago, IL, USA. From 2014 to 2017, she was a Marie-Sklodowska-Curie IntraEuropean Fellow with the London Centre for Nanotechnology, University College London, London, U.K. Since 2015, she has been a Lecturer at École Polytechnique Fédérale de Lausanne, Switzerland. She is an Associate Professor with the Department of Applied Science and Technology, Politecnico di Torino. Her research interests include nanotechnology, emerging technology devices, the simulation and design of nanocomputing devices, architectures, and circuits with physical-aware computer-aided design (CAD) tools, field coupling nanocomputing, and quantum computing.

• • •